Numerical Investigation of Erosion of a Pipe Protruded in a Sudden Contraction

BY

MUHAMMAD EHSANUL KABIR

A Thesis Presented to the

DEANSHIP OF GRADUATE STUDIES

KING FAHD UNIVERSITY OF PETROLEUM & MINERALS

DHAHRAN, SAUDI ARABIA

In Partial Fulfillment of the
Requirements for the Degree of

MASTER OF SCIENCE

In

MECHANICAL ENGINEERING

JUNE 2005

KING FAHD UNIVERSITY OF PETROLEUM & MINERALS

DHAHRAN 31261, SAUDI ARABIA

DEANSHIP OF GRADUATE STUDIES

This thesis, written by **MUHAMMAD EHSANUL KABIR** under the supervision of his thesis Advisor and approved by his Thesis Committee, has been presented to and accepted by the Dean of Graduate Studies, in partial fulfillment of the requirements for the degree of **MASTER OF SCIENCE IN MECHANICAL ENGINEERING.**

Thesis Committee

Dr. M. A. Habib
(Thesis Advisor)

Dr. Rached Ben-Mansour
(Thesis Co- Advisor)

Dr. Faleh A. Al- Sulaiman
(Department Chairman)

Dr. Hassan M. Badr
(Member)

Dr. Mohammad Abdulaziz Al-Ohali
(Dean of Graduate Studies)

Dr. Esmail Mokheimer
(Member)

Date: ١٤٢٦/١٢/٣
3-1-2006

Dr. Syed A.M. Said
(Member)

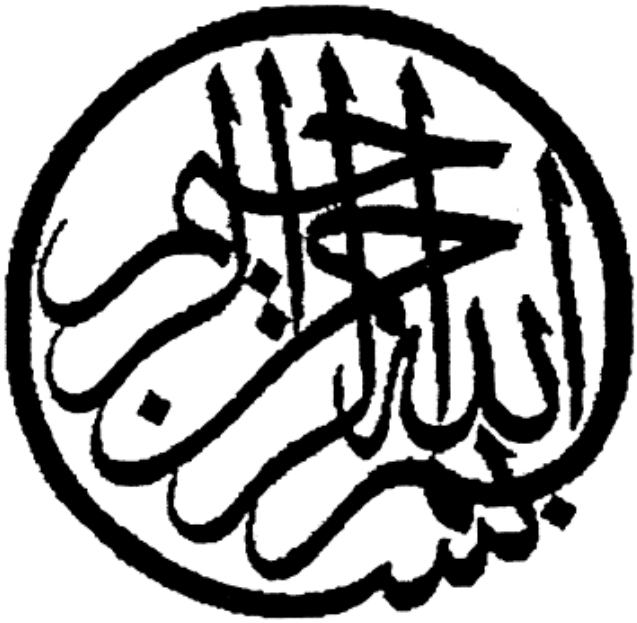

In the Name of Allah, Most Gracious, Most Merciful.

To

The Martyrs of the Liberation War of Bangladesh

&

To

My Parents, Sisters, Brothers-in-law, Nephews and Nieces

ACKNOWLEDGEMENT

All praises and thanks are first due to Almighty Allah for providing me this opportunity to complete this work. Acknowledgement is due to King Fahd University of Petroleum and Minerals (KFUPM) for its support in carrying out this research and for granting me the Research Assistantship to pursue my graduate studies.

I express my profound gratitude to department chairman Dr. Faleh A. Al-Sulaiman for providing me favorable environment for working.

I would like to express my profound gratitude to my thesis supervisor Dr. M. A. Habib for his inspiration, suggestion, constant help and guidance throughout the period of my research. I am indebted to my thesis committee co-advisor Dr. Rached Ben-Mansour for his constructive help specially the time he spent to teach me the FLUENT software. Sincere thanks to Dr. H. M. Badr for spending his valuable time in correcting the manuscript. I am also grateful to my thesis committee members Dr. S. A. M. Said and Dr. Esmail Mokheimer for their constant support and encouragement. Thanks are also due to Dr. M. A. Antar for providing me enough computing facilities.

I would also like to thank all the members of Bangladeshi community for their wonderful company throughout my stay at K.F.U.P.M. Special gratitude goes to reaz, shibly and raza bhai, for providing their invaluable mental support during my toughest times. Acknowledgement is also due to jewel for helping me a lot in preparing this manuscript. Special thanks to sumon for his witty opinions in explaining many things related to academia and human life, which pacified many of my stressful moments during the long working hours.

Finally, I am grateful to my parents and all family members for their constant prayers, huge mental support, enormous inspiration and endless sacrifices that helped me to engage all my strength to complete this research work.

Table of Contents

List of Tables

List of Figures

ABSTRACT

Name **Muhammad Ehsanul Kabir**

Title **NUMERICAL INVESTIGATION OF EROSION OF A PIPE PROTRUDED IN A SUDDEN CONTRACTION**

Major Field **MECHANICAL ENGINEERING**

Date of Degree: **1st June 2005**

The aim of this research is to numerically investigate the erosion phenomenon of a pipe protruded in sudden contraction geometry. The importance of this problem is mainly due to erosion of various gas and liquid flow passage devices such as heat exchangers, pipes, pumps, turbines and compressors, where erosion imposes serious problems like frequent failures and loss of expensive production time. In the present work, the geometry is an axi-symmetric abrupt pipe contraction with a pipe protrusion embedded in it. The flow is steady, 2-D axi-symmetric and is considered turbulent. The continuous flow field is obtained by solving Steady-state time averaged conservation equations of mass and momentum along with RNG- model for turbulence. Particles are tracked by using Lagrangian particle tracking. Finally, an erosion model is employed to investigate the erosion phenomena. In this study, different parameters are varied to observe their influence on erosion rate. A range of values is selected for every parameter. Inlet flow velocity is varied from 0.5 m/s to 10 m/s. Particle diameter is varied from 10μm to 400μm. Both the protruded pipe depth and thickness are varied for the ranges of 1mm to 5mm. Contraction ratios from 0.25 to 0.50 are considered. Carbon steel and aluminum are selected as pipe material.

Obtained results show strong influence of each parameter on the erosion rates of the protruded pipe. The results show erosion rate increment with the increasing inlet flow velocity and particle diameter. A declining trend in erosion rate is observed for the increasing protruded pipe depth and thickness values. A similar declining trend is also observed with the increasing contraction ratio. Particle trajectories are observed for all the cases to get an insight into these findings. Threshold values for the inlet flow velocity and the protruded pipe depth are obtained. In order to determine the most eroded and the most penetrated geometric configuration of the protruded pipe, additional analysis is performed with different combinations of depth and thickness.

MASTER OF SCIENCE DEGREE
KING FAHD UNIVERSITY OF PETROLEUM AND MINERALS
Dhahran, Saudi Arabia.

ABSTRACT (ARABIC)

ملخص الرسالة

الاسم: محمد إحسان الكبير
عنوان الرسالة:دراسة عددية للتآكل في أنبوب وضع بارزا عند مضيق مفاجيء لسريان داخل أنبوب
التخصص: الهندسة الميكانيكية
تاريخ التخرج: 23 ربيع الثاني 1426

يعتبر التآكل بالحت إحدى أهم المشاكل لكثير من شركات البترول و الغاز حيث يتسبب في توقف المعدات عن العمل بالإضافة إلى ارتفاع تكلفة الأجزاء المتآكلة. لحل هذة المشكلة فإنة يتم استخدام أغطية مصنوعة من مواد مختلفة لحماية أنابيب المبادلات الحرارية ويتم تغييرها عندما تتآكل. يتعلق هذا البحث بدراسة ظاهرة التآكل بالحت في أنبوب تم إدراجه بارزاً عند مضيق سريان مفاجيء. تمت الدراسة الحالية فى إنسياب داخل أنبوب متماثل حول محوره و ذى مضيق مفاجيء. و قد تم إدراج الأنبوب البارز عند مدخل المضيق. يتم فى هذا البحث دراسة عددية للسريان المضطرب المتاثل، ثنائي البعد ذى الكثافة المنخفضة لذرات الرمال فى الحالة الخاصة للانسياب ثنائى الطور(سائل و صلب). تم حل مجال السريان المستمر باستخدام معادلتي الكتلة وكمية الحركة باعتبار المتوسط الزمنى للسرعات فى السريان المضطرب. وتم حل المعادلات التى تحكم حركة الحبيبات تحت ظروف الجاذبية و اللذوجة و ذلك باستخدام طريقة لاجرانج. أخيراً تم استخدام نموذج رياضي لحساب معدلات التآكل و من ثم دراسة ظاهرة التآكل بالحت. تم التحقق من دقة الحسابات عن طريق مقارنة نتائج الحسابات مع النتائج المعملية المتوفرة.

غطت الدراسة تأثير عدة متغيرات على معدل التآكل بالحت، حيث تمت دراسة تأثير سرعة السريان عند المدخل فى المدى من 0.5 م/ث إلى 10 م/ث، تغير قطر الحبيبات من 10 ميكرومتر إلى 400 ميكرومتر، عمق وسمك الأنبوب البارز من 1 مم إلى 5 مم، ونسبة التضييق (نسبة قطرالأنبوب عند المخرج إلى قطره عند المدخل) من 0.25 إلى 0.5. كما تمت دراسة تاثير نوع المادة المصنعة منها الأنابيب حيث استخدمت مادتي الألمنيوم والفولاذ الكربونى. أوضحت نتائج الدراسة تأثيراً قوياً لكل المتغيرات على معدل التآكل في الأنبوب الذي تم إدراجه، حيث أوضحت النتائج زيادة معدل التآكل بزيادة السرعة عند المدخل وقطر الحبيبات , ونقصانه مع زيادة عمق وارتفاع الأنبوب المدرج، وهو ما تم الحصول عليه أيضاً عند زيادة نسبة التضييق. تم تحليل مسارالحبيبات لكل الحالات لتفسير و تأكيد النتائج التى تم الحصول عليها. أيضا تم تحديد سرعة السريان عند المدخل وعمق الأنبوب المدرج التى يمكن عندها تلافى التآكل بالحت.

NOMENCLATURE

a	constants defined in equation 3.19
a”	constant defined in equation 3.27
A	impingement area, defined in equation 3.25
b”	constant defined in equation 3.27
a_c	constant defined in equation 3.29
b_c	constant defined in equation 3.29
BHN	Brinell Hardness Number
A_w	empirical constant defined in equation 3.27
$C_{1\varepsilon}$,, $C_{2\varepsilon}$, $C_{3\varepsilon}$	empirical constant used in the Standard k-ε model in equation 3.6
$C_{\varepsilon 1}$, $C_{\varepsilon 2}$, $C\varepsilon_3$	empirical constants in the k-ε (RNG) model in equation. 3.13
C_μ	constant defined in equation 3.15
C_D	drag co-efficient
C_k	constant defined in equation 3.30
Cr	contraction ratio
d_p	particle diameter
E	erosion rate
E’	roughness parameter of wall defined in equation 3.32
F	force
F_s	shape factor defined in 3.29
g	gravitational acceleration
G_b	production of turbulent kinetic energy due to buoyancy

G_k	production of turbulent kinetic energy due to mean velocity grad.
H	protruded pipe depth.
k	kinetic energy of turbulence
l	Length scale
LER	Local erosion rate, mg/g
L/H	normalized distance along protruded pipe depth
m_p	mass of the particles
N	number of control volumes in a certain mesh size
N_p	number of particles
p	pressure
P	parameter defined by Finnie et al. (1992) at equation 3.24
Pn	penetration rate
Pr_t	turbulent Prandtl number
Re_p	particle Reynolds number
r_1	Large bore pipe radius
r_2	Small bore pipe radius
R_f	parameter defined by Wood et al. in equation 3.30
S	modulus of the mean rate of stress tensor
S_m	a geometric constant by defined by Salama (1998) in equation 3.26
$\dot{s}$	sand rate (kg/s)
T	protruded pipe thickness
T_L	characteristic lifetime of the eddy
TER	total erosion rate, mg/g

u_p	particle impact velocity
u_{cr}	critical particle velocity defined in equation 3.23
$\bar{u}, \bar{v}$	time averaged velocity components
u' v'	fluctuating components of velocity
$\overline{U}_j$	average velocity component
V_{mix}	fluid mixture velocity, kg/day, defined in equation 3.26
W	sand production rate, kg/day
x_j	space coordinate
y_p	is the actual distance from point P to the wall
y_p^+	dimensionless distance from point P to the wall
Y_M	contribution of the fluctuating dilatation to the dissipation rate
x, y, z	constants defined in equation 3.29
X, Y, Z	constants defined in equation 3.27

Greek Symbols

ϕ	general field variable represented in the transport equation
ε	rate of dissipation of the kinetic energy
κ	Von Karman constant defined in equation (3.32)
δ	kroneker delta
μ	viscosity
ρ	density
σ_k	effective Prandtl number for k
σ_ε	effective Prandtl number for ε
β	coefficient of thermal expansion

τ	shear stress
α	impingement angle
γ	cutting wear defined in equation 3.22
σ	deformation wear defined in equation 3.22
$\hat{\alpha}$	angle defined in equation 3.24
ρ_{mix}	fluid mixture density defined in equation 3.26
λ	step length factor.

Subscripts

D	drag
eff	effective
i,j	spatial coordinate indices
lc	local
m	target material
mix	mixture
p	particle or wall node
pg	pressure gradient
sl	saffman lift
t	turbulent
vm	virtual mass
w	wall

Superscript

$\dot{}$	time rate
$\overline{}$	time average

Chapter 1

Introduction

1.1 Flow through Pipes and Pipe Contractions

Fluid flow in ducts and pipes is a commonly encountered phenomenon in engineering practice and as such requires special attention. For a flow to take place, a pressure difference must exist between the inlet and the outlet. This is the pressure difference, which determines the flow rate. The designer of flow system, therefore, needs to estimate this pressure difference for a given flow rate and hence be in a position to select a suitable pump for his system. Thus, it is apparent that a poor estimate of the pressure difference will lead to the flow system operating away from its optimum condition and this could be detrimental to both system performance and operating cost. In practice, flow systems or pipelines do not consist entirely of straight length of pipe where the flow is fully developed. Rather they consist of entry length, bends, valves, fittings, changes in cross section such as a contraction from large pipe bore to a small bore and enlargements. Contractions exist in a variety of process and chemical plants. Examples are heat exchangers, fired heaters and boilers, where they occur in conjunction with enlargements and at the entrance to the tube bundles that are

attached to the manifolds or headers. Contraction also occurs in conjunction with enlargements because of the use of ferrules for close control of the flow distribution within tube bundles. Differential ferruling is often used to ensure that each tube receives a flow, which is consistent with its heat input and pressure loss characteristics. Thus, it is important to be able to calculate not only the absolute pressure drop through specific ferrule sizes but also the variation between closely spaced sizes.

A schematic diagram of fluid flow through pipe contraction is shown in the following Figure 1.1. As the fluid flows through the large bore pipe, there is a dissipation of energy due to fluid friction. At some location '1' (Figure 1.1) upstream of the contraction, the fluid separates from the pipe wall and is directed towards the entrance of the small-bore pipe. The streamlines continue inwards towards the pipe center past the contraction '1C/2C' to form a minimum flow area called the vena contracta. It is shown as location '2' in the Figure 1.1. Downstream the vena contracta, the fluid expands to re-attach at location '3' to the walls of the small bore pipe. The pressure loss due to the contraction thus occurs from the point of separation in the large bore pipe to the point of re-attachment in the small-bore pipe.

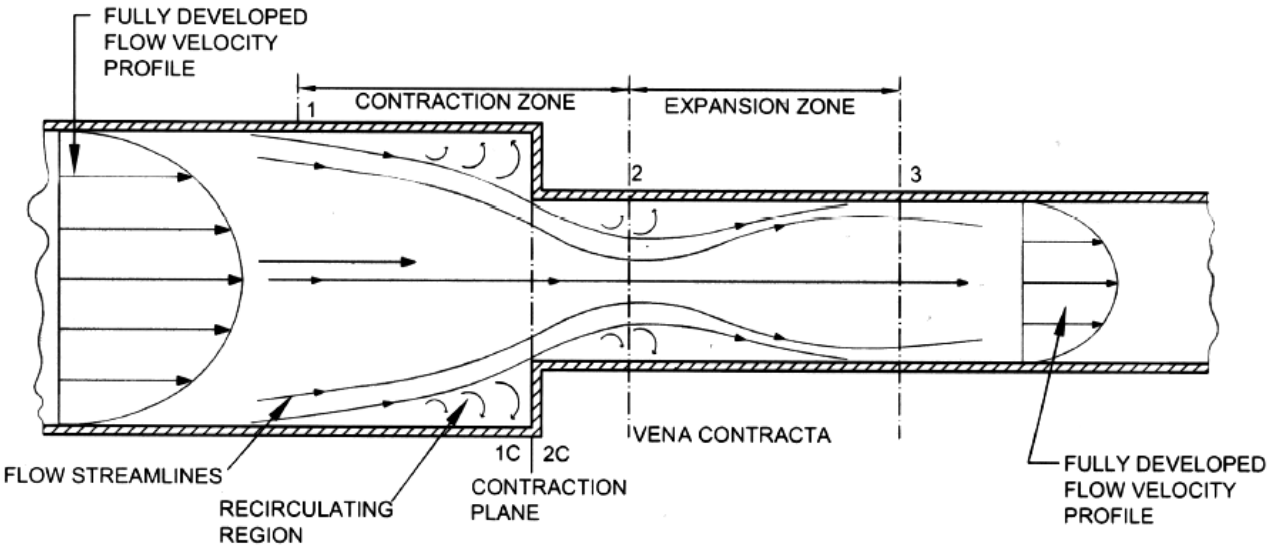

Figure 1.1 : Flow through a sudden pipe contraction

The contraction process thus consists of a contraction in flow area from the large pipe bore to the vena contracta, followed by an expansion process from the vena contracta to the small-bore pipe. The mechanism responsible for the additional pressure loss caused by the change in area is essentially the generation of large-scale turbulence that extracts energy from the mean flow. The accurate prediction of contraction pressure loss is important when it is a significant component of the overall system pressure loss, or when it can have significant effect on the flow conditions. These situations are most commonly encountered in heat exchangers, particularly fired heaters, boilers, cooling water condensers etc.

Another factor, which has significant importance to the industrial applications, is the erosion of the contraction. Geometric modification of the inlet geometry and significant reduction in pressure loss can occur due to this erosion phenomenon. Erosion is the process of metal removal by solid particle impact. This is a problem in many multiphase flow industrial devices, particularly in petroleum industries. In the oil industry, entrained abrasive sand particles are carried with the oil up to the well string, causing wear of the oil pipeline. Erosion is greatly enhanced where any discontinuity of the oil pipe occurs.

In the present work, the erosion phenomenon of a pipe protruded in a sudden contraction is studied. In typical industrial applications such as heat exchanger, erosion of the tubes is a common thing to occur. In a real life heat exchanger, tubes are situated in bundles. The current work focuses the erosion of a single pipe to analyze the whole phenomena more minutely. Numerical approach is adopted in the Lagrangian reference

frame to solve the current problem. This approach represents a one-way flow-to-particle coupling method that can be used when low volume of particles is simulated. Two computational models were developed. The first was the continuous phase model (dealing with the prediction of the flow velocity field) and the second was the particle-tracking model (dealing with the prediction of particle motion). Through a combination of computational fluid dynamics (CFD) and Lagrangian particle tracking, predictions of particle movement through complex geometries were achieved. Using the particle-tracking model, solid particles were tracked through the domain in a Lagrangian manner using Lagrangian equation of motion of a particle. The impingement data (impact speed and angle) were first compiled for all particles on the specified solid boundaries of the flow domain. For computing the erosion rates, the compiled data was used in an erosion model. In the present work, the erosion model proposed by Wallace and Peters (2000) was utilized. The erosion rate calculations were performed using the equations of the above-mentioned model, via a programmed code linked to a CFD package (Fluent in this case). Commercially available software tools have found the way in many design processes now a days.

1.2 Motivation and Importance of the Present Work

The present work demonstrates the flow of fluid (water in this case) through pipe contraction geometry with a protruded pipe embedded in it. This work originates from a very

important real life problem for any industry dealing with fluid-solid transport, especially in the areas of oil and gas production. Solids such as sand are entrained in the fluid and impinge the walls of piping and equipment. As a result, removal of the wall material occurs. This phenomenon is termed as “solid particle erosion” and can significantly reduce service life. Figure 1.2 shows the schematic diagram of the present case. The protruded pipe is inserted inside the sudden contraction pipe geometry so that the solid particle erosion phenomenon can be better investigated from different points of view. Firstly, the pattern of the entrained particle trajectories, their impinging locations and the subsequent erosion pattern are obtained by observing the eroded surface of the protruded pipe. Secondly, optimum protrusion pipe dimensions (depth and thickness) can be calculated by analyzing their effect on total erosion and penetration rates for a specific pipe material. This can act as a guide to industrial applications. A threshold depth of the protruded pipe can be obtained for an industrial use similar to that of the flow condition of the present work. Thirdly, variation in erosion rates due to variation in target material can be obtained by using different material for the protruded pipe.

The above-mentioned observations lead to a comprehensive guess about the longevity of the protruded pipe that can provide guideline for similar type of industrial applications. After the protruded pipe is eroded, there is a possibility of future leakage through the tube sheet that may lead to serious safety hazard. As a result, a crucial decision on future preventive measures can be obtained from this analysis.

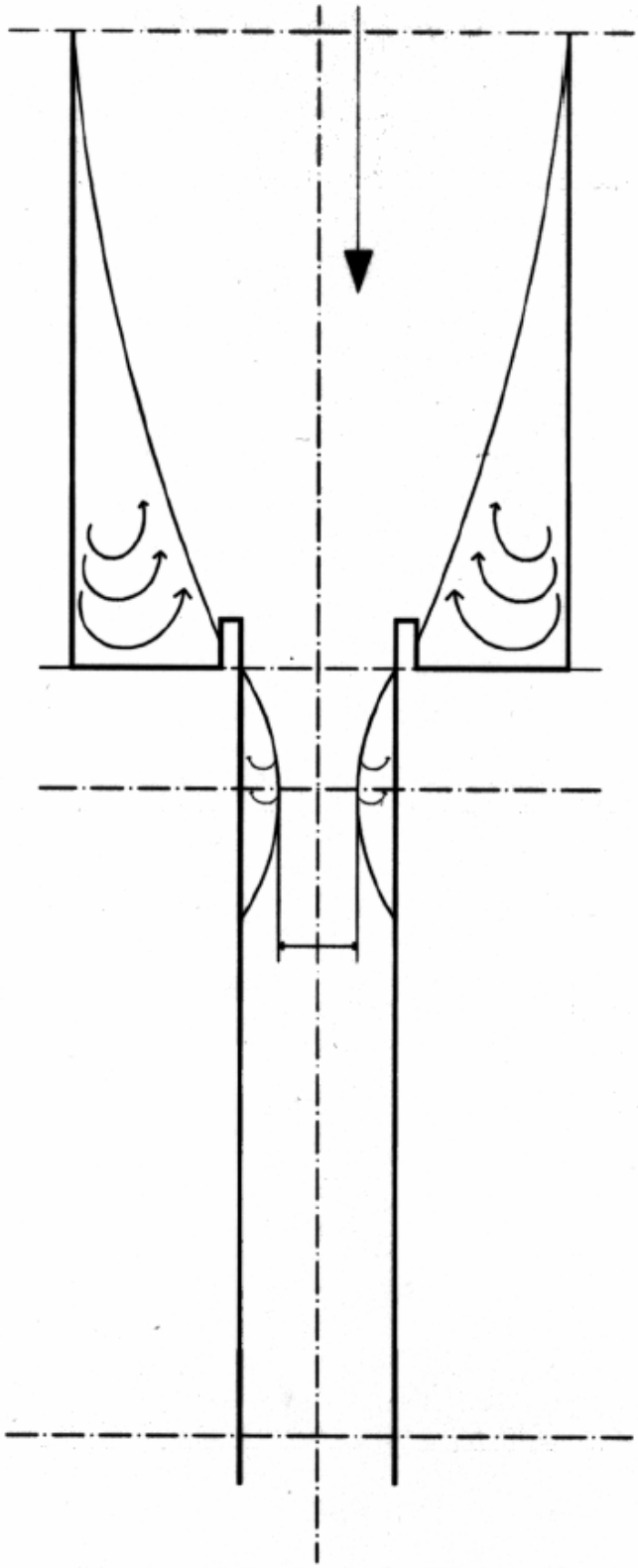

Figure 1.2 : Flow through sudden contraction with an embeded protuded pipe

1.3 Motivation for Numerical Modeling in the Present Work

Reasons for numerically modeling the erosion phenomena of the protruded pipe in a sudden contraction are:

- Experimental setup of a real kind like that of the present study is very difficult to build as it involves lot of complexities due to turbulent flow.
- A significant amount of numerical research work has been performed in similar type of areas using different numerical models.
- Carrying out simulations will be economical and less time consuming than the corresponding experiments when a proper model has been setup and validated.
- Results obtained from numerical modeling can be very helpful for understanding the underlying physics of the present problem. Moreover, changing different variables (related to flow condition and geometry of the problem) and observing their influence on erosion rates can be conveniently performed. Performing such structural readjustments and test condition alterations would be much difficult for an experimental setup.

1.4 Approach for Solving the Present Problem

The present research work aims at investigating the erosion of a pipe protruded in a sudden contraction. While doing that, investigations are to be carried out to demonstrate the influence of relevant parameters on the erosion process. These relevant parameters are inlet

flow velocity, diameter of the sand particles, protruded pipe's geometric parameters: depth and thickness, material of the protruded pipe. The Lagrangian Particle Tracking Method is used to predict particle trajectories. Modeling of the erosion process is carried out in the following steps:

a) Prediction of the flow velocity field of continuous fluid in the domain of interest.

b) Calculation of the solid particles trajectories using Lagrangian particle tracking calculations and then extraction of the particle impact data (impact angle and velocity).

c) Prediction of erosive wear using a semi-empirical equations.

1.5 Structure of the Thesis

This thesis is organized in seven chapters.

- Chapter 2 gives a brief detail of the review of the literatures related to the present work. The objective of the current research is also stated there.
- In chapter 3, governing equations of the existing flow situations are stated. Problem statement, boundary conditions have been discussed.
- Chapter 4 deals with the numerical procedure and detailed solution procedure of the current problem.
- Chapter 5 contains the validation part. A geometric configuration similar to that of the current problem has been numerically simulated. Erosion rates are obtained by employing a suitable erosion model. The erosion results are validated with the experimental results reported in the literature.

- Chapter 6 presents the detailed presentation of the obtained results. These results contain influence of various flow and geometry related parameters on erosion rates. Calculations of the threshold values for inlet flow velocity and protruded depth are also performed.

- Chapter 7 includes concluding remarks and different recommendations for the future research.

Chapter 2

Literature Survey

The current research work deals with the erosion estimation of a pipe protruded in a sudden pipe contraction. Numerous experimental and numerical research works on erosion estimation of similar types of geometries were performed before and many are going on. The most accepted approach of erosion estimation of various types of geometries adopted by most of the researchers in this area is a three-step approach. This three-step approach is: prediction of the flow field in the domain of interest, calculation of particle trajectories and prediction of erosion from the data obtained in the previous steps. Based on the pattern of this problem and the possible ways to solve it, the literatures can be divided into the following three categories:

A) Literature linked to the prediction of flow field in the domain of interest.

B) Literature dealing with the Particle tracking.

C) Literature related to the erosion modeling.

2.1 Literatures Related to Flow Field of Pipe Contraction

2.1.1 Experimental Investigations

For laminar flow regions, Durst *et al.* (1985) carried out a comprehensive study for the Reynolds number range (based on the upstream pipe diameter) of 23 to 1213 for an area ratio of 0.285 using Dual Beam LDA system operating in the forward scatter mode with signal processing by a frequency tracker or transient recorder. Some important features identified by the investigation were the location of the velocity maxima close to the pipe wall (velocity overshoot) and the flat distribution of velocity in the central part of the section downstream of the contraction for Reynolds number 196 or greater. They estimated the recirculation bubble to start at a Reynolds number of approximately 300. The dimensions of this recalculation bubble (its length and depth) were found to increase with higher Reynolds number. Bullen *et al.* (1986) proposed a detailed experimental setup to investigate turbulent flow field through a sudden pipe contraction. The experimental results were presented for fourteen points of measurements. The detailed flow field through contraction for an area ratio of 0.332 and Reynolds number of 1.54×10^5 was measured using a Three Beam Laser Doppler Anemometer. These measurements were presented in the form of mean velocity, turbulence intensity, and Reynolds stress. They showed several observations such as the accelerations of the flow through contraction, formation of the vena contracta, its axial position, size and re-establishment of uniform flow. They found out that at the downstream of the contraction, the maximum velocity did not occur at the pipe axis but it was displaced towards the pipe

wall. This velocity 'overshoot' had a maximum value of 1.58 times the bulk velocity. The prediction of the flow field was performed using Fluent code with standard κ-ε turbulence model. These showed good agreement in terms of redevelopment of the downstream flow. However, their findings of detailed flow field near to the wall and close to the contraction were not well represented. Pipe contraction flow field measurements for the turbulent flow regime have been reported by Khezzar *et al.* (1988), who measured mean axial and radial velocities as well as their rms for a Reynolds number (based on upstream pipe diameter) of 4.0×10^4 and for an area ratio of 0.4. The reported measurements did not cover the region in the immediate vicinity of the contraction and as such no conclusion about the vena contracta was drawn.

An experimental study of turbulent water flow through abrupt contractions which resembles the present very much geometry, was performed by Bullen *et al.* (1996)**.** They carried out detailed experiment to determine the flow field. Wall static pressure measurements enabled the calculations of pressure loss coefficient for a range of contraction area from 0.13 to 0.69 over a Reynolds number variation from $4x10^4$-$2x10^5$. The effect of variation in contraction sharpness was also established. To establish the detailed flow features, measurement of mean velocities and turbulence intensities were made using a Two Component Laser Doppler Anemometry for one area ratio of 0.332. They developed a pressure loss coefficient prediction method which allowed for velocity profile variation through contraction. There was a good agreement between the experimental values of pressure loss coefficients and the predictions based on the above method. The results of pressure loss coefficient presented in the paper showed that at

high Reynolds number, accuracy was about 5% to 10% for smallest and largest area ratios respectively. The authors showed that the inlet sharpness had a significant effect on the pressure loss coefficient. Fossa and Gugliemini (1998) experimentally investigated the void fraction in horizontal pipe with sudden contraction area. The experiments were aimed at analyzing the effect of the singularity characteristics on void fraction profiles and phase distribution. The instrumentation set up consisted of ring electrode pairs placed on the internal wall of the cylindrical test duct, flush to the pipe surface. Plug and slug flow regimes were investigated in order to obtain the mean void fraction in five different locations upstream and downstream. The analysis of the results showed that the characteristics of the flow restriction deeply modify the flow structure upstream and downstream the discontinuity. Contractions existed at the entrance to the tube bundles, which were attached to manifolds or headers.

The experimental determination of contraction pressure loss coefficients in the turbulent flow regime were reported by Bendict *et al.* (1966) and Gerami-Tajabadi H. (1985). However, Bendict *et al*. (1966) did not specify the Reynolds number range of their tests. Some measurements in the transition region up to Reynolds number of $7x10^3$ for one area ratio of 0.28 was reported by Kays (1950). Measurement of loss coefficients were given by Astarita and Grego (1968) for a range of Reynolds number between 20 and $2x10^3$ for one area ratio of 0.16. In all cases except Gerami-Tejabadi, the contraction was defined as sharp but had not been quantified in geometrical terms. Greami-Tejabadi, H. (1985) reported results for five different area ratios for a Reynolds number range of $5.0x10^4$ to $2.3x10^4$. Unlike Benedict, he found the loss coefficient to be dependent on

Reynolds number. However, the results for the two smallest tested area ratios were found to be non-reproducible. He also emphasized the significance of the inlet geometry but did not provide any detailed results.

2.1.2 Numerical Investigations

Shih *et al.* (1995) proposed a new k-ε eddy viscosity model that can be used for the accurate predictions of flows of high curvature such as the flow in pipe contraction. The model consisted of a new model dissipation rate equation and a new realizable eddy viscosity formulation. The new model dissipation rate equation was based on the dynamic equation of the mean-square vortices fluctuation at large turbulent Reynolds number. The new eddy viscosity formulation was based on the realizable constraints. It was found that the present model with a set of unified model coefficient could perform well for a variety of flows. These flows are channel flow, rotating homogeneous shear flow and backward facing step separated flows. The model predictions were compared with available experimental data. The results from the standard k- ε eddy viscosity model were also included for comparison that showed a significant improvement.

It is notable that none of the investigations has considered pipe protrusion as their required geometry. Rather all the literatures discussed so far provided data for a qualitative development of the flow through sudden pipe contraction only. However the data is not detailed enough to enable a comprehensive correlation of the flow field to be made. Invariably there are problems with such correlations since all the relevant data

such as inlet flow conditions, inlet sharpness are not well known for all the studies and this makes it very difficult to get any direct comparison among the various studies.

2.2 Literatures Dealing with the Particle Tracking

Two approaches are normally used to predict two-phase flow. These are Eulerian and Lagrangian approach. The Lagrangian approach treats the fluid phase as a continuum and predicts the trajectory of a single particle in the fluid flow as a result of various forces acting on the particle. By assuming different starting positions of the particles and following their trajectories, a solid-fluid flow can be simulated. Eulerian approach treats the solid as some kind of continuum, and appropriate continuum equations for the fluid and particle phases are solved. In Lagrangian approach, the particle impact velocities and angles can be determined at solid surfaces. On the contrary, greater difficulty is associated with obtaining actual particle impact velocities and angles at solid surfaces in the Eulerian modeling procedure. As this information is vital for erosion modeling, the Lagrangian method for trajectory computations is adopted in the present study. Therefore, most of the covered literatures are related to the Lagrangian approach.

2.2.1 Literatures Related to Eulerian and Lagrangian Approaches of Solid Particle Tracking

Picart *et al.* (1986) developed a method that accounted for the anisotropic effects in the turbulence field through second-order algebraic extensions to the k-ε model. A transport equation was written for the particle number density of spherical monosized particles, and particulate dispersion was accounted for. Tu *et al.* (1996) attempted to

develop an Eulerian formulation that could better account for behavior near an obstructing wall surface. The concept was to define a particle-wall rebounding layer in which the collision process had a significant effect on incoming particles. Durst *et al.* (1985) made a comparison between two approaches while predicting the particulate two-phase flows. Both Eulerian and Lagranigan approaches were discussed and their basic equations for particle and fluid phases as well as their numerical treatment were also discussed. Cases like vertical pipe flow with various particle concentrations, sudden expansions in a vertical pipe were discussed. They concluded that the Lagrangian approach has some distinct advantages for predicting the particulate flows with large acceleration. It could also handle particulate two phase flows consisting of poly dispersed particle size distribution. Lu *et al.* (1993) established a three-dimensional Lagrangian Model for the motion of the particles in three-dimensional flows. They adopted the idea of time series analysis to the temporal and spatial fluid velocity correlations. This model was used to simulate the experiments of other works. The computed results were compared with the experimental data for the particle dispersion, velocity dispersions and the velocity decay. In the case where the mean turbulent flow had one main direction, this model was extended to include the Eulerian temporal velocity correlation. As a result, a so-called mixed model was devised. This model was applied to compute the particle dispersion in stationery, homogeneous, isotropic and incompressible turbulence. Comparison was made with the theoretical particle diffusion coefficients and a good agreement was reached.

2.2.2 Literatures Concerned with the Basic Equations of Particle Tracking

A particle that is moving in a fluid experiences a variety of forces acting upon it. These forces determine the particular path taken by the particle as the fluid carries it along. Michaelides (1997) gave the earliest form of the equation for the transient hydrodynamic force acting on a sphere that was initially at rest and is accelerated, in an infinite fluid at rest. This is known as the Basset-Boussinesq-Oseen equation (B-B-O). This equation is only valid for conditions of low velocity and large acceleration, and does not truly apply at finite particle Reynolds numbers. A popular method of overcoming this limitation is to introduce empirical coefficients, particularly for the steady-state drag, which extends the range of application of this equation. Odar and Hamilton (1964) applied those required coefficients. This equation can be applied to the case of a sphere moving in a quiescent fluid. If the fluid is also moving, the relative velocity between the sphere and the fluid will be required. Other forces also act on a particle moving through a fluid. The pressure-gradient force is the force required to accelerate the fluid that occupies the particle volume if the particle is absent. Clift *et al.* (1978) gave this force, in its full form**.** Two lift forces may operate on a particle. The Magnus force originates from the nonlinear terms of the Navier-Stokes equations, and is a lift force resulting from particle rotation at low Reynolds numbers. Jayanti and Hewitt (1991) gave the Magnus force expression. Saffman (1965) showed that a small sphere in a slow shear flow experiences a lift force perpendicular to the flow direction. This is often referred to as the Saffman lift force.

Other forces that may act on a particle are the body force due to gravity and the buoyancy force. It is often the case that some of these forces can be justifiably neglected. Meng and Van Der Geld (1991) performed a comparative study among Saffman lift, added-mass, pressure-gradient, and Basset history forces. These are applicable for particles of various sizes moving in an inviscid liquid flow over a cylinder. They employed an estimation-iteration approach to solve the complex Basset history term. The results concluded with some observations. Firstly, the Saffman lift force was always very small and can be ignored. Secondly, added-mass force was only important for large particles (particle sizes in their study were 250, 1250 or 2500μm). Thirdly, pressure-gradient force was generally important. Fourthly, changes in the Basset history force were related to the steady drag force, and it could have considerable influence in particle trajectory calculations. Based on the findings of Meng and Van Der Geld (1991), it would be possible to neglect the Saffman lift force for erosion modeling calculations, as the particle sizes were generally small. Inclusion of the Basset history force greatly complicates particle trajectory calculations, and is generally neglected in erosion modeling studies. It is obvious that there are several forces acting on particles in a fluid flow. Not all forces need to be included in all simulations, but it will generally be the case (for industrial simulations at least) that the forces included in a calculation would be those that are made available to the user of a commercial CFD code. As per the findings of Meng and Van Der Geld (1991), Saffman's lift force is neglected in the present calculations.

2.2.3 Literatures Related to the Modeling of Turbulent Particle Dispersion

The velocities required in the particle equation of motion are the instantaneous fluid and particle velocities at that instant in time. A comprehensive review and introduction to the subject has been provided by Shirolkar *et al.* (1996). Lagrangian particle tracking methods can also be described as separated flow models because the discrete phase calculation is performed in a separate step from the fluid phase calculation. The separated flow models can be split into two divisions: Deterministic Separated Flow (DSF) models, and Stochastic Separated Flow (SSF) models. Deterministic models simply ignore the fluctuating component of the instantaneous velocity and obtain particle trajectories from the mean velocity field directly. This approach was adopted by Crowe *et al.* (1977) in their development of the Particle-Source-In Cell (PSI-CELL) method for gas-droplet flows. However this method did not address the fundamental problem of random fluctuations. There are three variants of stochastic separated flow model. Models based on the eddy lifetime (or eddy interaction) concept; time correlated models that generate fluid particle and discrete particle trajectories simultaneously and Probability Density Function (PDF) propagation models. The most popular approach to date has been the eddy interaction model.

In the eddy interaction model, the fluctuating fluid velocity of the eddy is randomly sampled from a Probability Density Function (PDF) based on local turbulence properties at the start of the particle-eddy interaction. The fluid turbulence closure model for the simulation gives the turbulence properties. A particle will interact with an eddy

for the minimum of either the eddy lifetime or the transit time taken for the particle to cross the eddy and pass from it. Gosman and Ioannides (1981) assumed the fluid turbulence to be isotropic and to possess a Gaussian probability distribution in the fluctuating velocity. Govan *et al.* (1989), Adeniji-Fashola and Chen (1990), Sommerfeld and Zivkovic (1992), and Chang and Wu (1994) used similar eddy interaction models that assume isotropic turbulence. Graham (1995, 1996) attempted to improve the eddy interaction model for isotropic turbulence by extending it to account for three main effects observed in particle dispersion experiments. These effects are, firstly, the crossing trajectories effect, or CTE, which results in reduced particle dispersion in the presence of a drift velocity. This can be accounted for by using the correct eddy length and fluid particle interaction time. The influence of gravity should also be included. Secondly, the inertia effect due to the density of the particles which is greater than that of the fluid. This is modeled by allowing the maximum particle-eddy interaction time to become greater than the actual eddy lifetime. Thirdly, the continuity effect where greater dispersion occurs in the drift velocity direction than at right angles to it. Calculating interaction times for each of the coordinate directions can model this effect.

2.2.4 Literature Related to the Particle-Wall Interaction Concept

Grant and Tabakoff (1975) developed particle rebound correlations for 200 μm diameter quartz sand particles 2024 annealed aluminum alloy at velocities between 76.2 and 118.9 m/s in air. A purpose-built erosion wind tunnel was used for the experimental testing. High speed photography provided the particle impact and rebound measurements.

Restitution ratios for normal and tangential velocity components were obtained in terms of impact angle. A later study by Tabakoff *et al.* (1987) applied Laser Doppler Velocimetry to measure impact and rebound velocities and angles for fly ash particles (around 5 μm) aluminum and a titanium alloy in air.

Other researchers used relations obtained by Grant and Tabakoff (1975) in their numerical predictions of solid particle trajectories. However, it is questionable as to whether those should be used for liquid particle flows, where liquid viscosity and inertia effects govern particle-wall interaction. Clark and Burmeister (1992) made an analysis of particle-wall interaction in liquid flows based on squeeze film theory. The film of liquid trapped between an particle and the wall has a cushioning effect on the particle—the squeeze film effect. In order for a particle-wall collision to occur, the particle must have sufficient velocity to overcome the effect of the squeeze film. If the particle is to rebound after impact, it must again have sufficient residual kinetic energy to escape from the squeeze film region and escape into the main flow. Should the particle have insufficient rebound energy, it will remain trapped by the squeeze film effects. Equations have been developed which allow estimation of the squeeze film effect. This theory has been successfully applied in erosion modeling studies by McLaury (1996).

2.2.5 Literatures Related to Numerical Investigations of Lagrangian Particle Tracking in Different Geometries

Edwards *et al.* (2000) focused on the evaluation of fittings commonly used to create a 90-degree flow turn, namely standard and long radius pipe elbows as well as a

plugged tee geometry. In this paper, the CFD code contained a Lagrangian particle-tracking algorithm that numerically predicts individual trajectories of a dispersed phase (solid particles, droplets) through the flow field. The code had also the capability to perform both mass and momentum coupling between particle equation of motion and the simulated flow field. In this Paper the authors showed that two new features were added to the CFD codes particle tracking capabilities. These features included squeeze film effect which is very important in situations where the carrier fluid is either a liquid or dense gas and particle rebound model that accounted for varying impingement angle. Wallace and Peters (2000) identified the limits of the standard CFD model when applied to the type of complex geometries found in multi orifice choke valve. Particle trajectories were obtained by Lagrangian particle tracking which involved solution of the particle equation of motion across many small intervals through the flow. Standard k- ε model was used along with SIMPLE or SIMPLEC pressure-velocity coupling method, to solve the equation set. Water at 20 degrees was used as the fluid. One of the obvious limitations of the CFD code was identified. That was the quality of prediction depends on computational meshes which maght be difficult for geometry like the choke valve.

A simplified particle tracking model for geometries like elbows and tees was proposed by Shirazi *et al.* (1995) proposed. This model was used to estimate the impact velocity of sand particle moving in a stagnation region near the pipe wall. A new concept of equivalent stagnation length was introduced which allowed the simplified procedure to be applicable to actual pipe geometries. The “equivalent stagnation regions” of an elbow and tee geometry of different sizes were obtained from the experimental data for small

pipe diameter, and a computational model was used to extend the procedure to large pipe diameter. Currently the prediction applied to the mild steel and accounted for the effects of sand size shape and density, fluid density viscosity and flow speed as well as pipe size and shape. The proposed method was verified for gas and liquid flows through several comparisons with the experimental data available in different literatures.

Wang and Shirazi (2003) reported a new CFD based correlation in their paper. The agreement between the predicted and the experiment data. They also focused on the effect of elbow radius on erosion in long-radius elbows. Chen *et al.* (2004) presented a CFD-based work applicable to oilfield geometries specifically elbows and plugged tees. Stochastic rebound model was applied in the simulations which gave reasonable estimate of the erosion rate. Wood *et al.* (2004) also proposed a modified form of Hashish (1987)'s volumetric erosion estimation correlation. They introduced their numerical correlation by taking into account of the target material property as well as the erodent properties. They successfully validated their model for the calculations of AISI 304 stainless steel bend.

2.3 Literatures Related to Erosion Modeling

A vast body of literature exists on the subject of erosion due to solid particle impact. The reason is the broad range of application from aerodynamic flows past turbine blades to flows inside pumps, pipes, bends and other fittings. Of particular interest are studies in which an effort was made to deriving equations (semi-empirical or otherwise) that relate erosive material loss to particle impact velocity and angle. Such equations have

been playing a vital role in the success of a CFD-based erosion modeling tool. Experimental test facilities have also been analyzed using the CFD-based technique. In the present work, literatures related to erosion modeling are presented in terms of different geometries. These geometries have good similarities to that of the present geometry.

2.3.1 Literatures Related to Erosion Prediction in Pipe Bends and Related Geometries

A fair amount of work has been carried out into the erosion modeling of pipe bends, elbows, tees and related geometries. Blanchard *et al.* (1984) developed a two-dimensional theoretical model to predict particle trajectories around a 90 degree bend. However, the predictions of maximum wear location did not agree sufficiently well with experiment. This was attributed to the inability of the model to account for secondary flows. Rubini *et al.* (1985) were able to account for secondary flows in their computation of gas particle flow round pipe bends with their fully-elliptic, three-dimensional, finite difference method for laminar and turbulent flows. No stochastic turbulent dispersion model was included in their Lagrangian particle tracking routine. Their predictions of wear location were compared against the experimental data of Mason and Smith (1972). Primary wear location was predicted to be occurred about 100 further downstream than the experimental data suggested, although the actual pipe geometry eroded considerably before measurements were taken in the experiments. A secondary wear location was also predicted. No quantitative comparisons of erosion magnitude were made.

Extensive comparisons of predicted penetration rates were made with the data of Bourgoyne (1989). Of these comparisons, 18 were for air-particle flow, and 3 were for mud-particle flow. With the air-particle flow, the average difference between measured and predicted penetration rate was 37.5 %, with the maximum difference being 56.1 %, and the minimum being 1.97 %. Differences were both above and below the measured values, which suggests some element of inherent scatter in the method. For the liquid-particle flows, differences were 54.2 %, 171.1 %, and 42.7 %, which did indicate poorer performance for liquid flows. The authors acknowledged this and cited the fact that secondary flows were not accounted for, as being the possible reason for poorer predictions. Locations of maximum penetration rates were predicted fairly well, using the erosion model of Ahlert (1994). Another comparison was made between prediction and experiment for a gas-particle flow round a bend. Particle concentration was far higher for this model than for the previous models. The experimental data of Eyler (1987) was compared against predictions. Penetration rates normalized on the maximum value, were compared in this instance. This method could not well predict actual erosion due to the high concentration. The agreement was very good.

More recent studies have also focused on erosion of pipe bends. Edwards *et al.* (1998) supplemented a commercial CFD code CFX with appropriate procedures to predict erosion on particle impact. The erosion model of Ahlert (1994) and its extension by McLaury (1996) (for aluminum) were used to predict erosive wear. Laser Doppler measurements of the flow structure round a bend (Enayet , 1982) were used to validate

the CFD predictions of flow field. Reasonable agreement was obtained. Agreement for the predicted wear distribution was good, although actual erosion magnitude was not compared. Keating and Nesic (2000) considered full 180 degree bend using the commercial CFD code PHOENICS in conjunction with a separate Lagrangian particle tracking code. Although the fluid velocity field was validated by comparison with experimental data, no comparisons were offered for the predictions of erosive wear made with a modified form of Finnie's (1958) model. This makes it difficult to assess the effectiveness of the model. Hanson and Patel (2000) also used PHOENICS in predicting the life of pneumatic conveyor bends undergoing erosive wear. Their work was somewhat different in that they attempted to account for the shape of the wear scar as erosion continued. However, the shape of the scar was not used to alter the computational mesh for fluid phase calculations by Hanson and Patel (2000). Hengshuan and Zhong (1990) considered the erosion of rectangular section bends using a two-dimensional inviscid approach both with and without secondary flow. Finnie's model (Finnie, 1960, 1972) was used to predict the erosion rate.

Comparison between predicted and actual distributions of erosion is favorable, with an improvement in prediction when secondary flow is accounted for. It can be seen that the erosion of pipe bends can be fairly well predicted both in terms of wear distribution and in magnitude. This is expected with the only solid surface being the outer boundary wall. The choice of erosion model has been that of Finnie (1958, 1960) in several cases, which suggests that even an early model such as this can give reasonable predictions of relative erosive wear. Wang and Shirazi (2003) performed their erosion

research on 90 degree elbows and bends. Their numerically simulated data of penetration rate was compared with available experimental data by Eyler (1987). The agreement between the predicted penetration rates and the experiment data was good. They found out that magnitude of the numerical erosion results did not agree well with most of the data because most of the data available were for erosion experiments with high particle rates. However, trend of the model predictions agreed well with the data in the literature. The authors found that erosion in long radius bends was reduced erosion when gas was the carrier fluid. They further reported that the effect of the squeeze film, secondary flows and turbulent flow fluctuations might play important roles in erosion predictions when the carrier fluid was liquid. These phenomena needed to be investigated further. The authors reported a new CFD based correlation. They recommended a first-order approximation for engineering calculations to account for the effects of elbow radius on erosion in long-radius elbows. This equation was recommended by the authors for computing the ratio of the wall thickness loss (or penetration rate) in long-radius elbow to the penetration rate of a standard (short-radius) elbow. The authors found the results using the correlation agreed well with the trend of available data in the literature. Chen *et al.* (2004) presented a CFD-based erosion prediction model. The salient feature of their work was the applicability of their work to oilfield geometries specifically elbows and plugged tees. Stochastic rebound model was applied in the simulations which gave reasonable estimate of the erosion rate. Numerical simulations showed that particle rebound behavior played an important role in determining the motion of the particles. Thus the authors recommended that particle rebound behavior might have a significant role in particle trajectories and there by on erosion profile. For cases where strong

particle recirculation potentially occurred, the application of stochastic rebound model was required to acquire realistic simulated results of erosion. The authors reported that the CFD-based erosion procedure was able to predict reasonably the erosion profile and satisfactorily showed the trend of erosion with respect to the carrier velocity. But the quantity of erosion was over predicted by about one order magnitude, which suggested that the erosion correlation needs to be re-evaluated.

2.3.2 Literatures Related to Straight pipes and Constrictions

A few studies are available where erosion resulted from random perpendicular impacts of particles passing through a straight walled pipe or constricted section. McLaury (1996) modeled the erosion taking place within straight choke geometry. Their method was based around a two-dimensional axi-symmetric CFD code. It accounted for turbulent dispersion of particles (with a stochastic model) as well as the 'squeeze film' effect Clark and Burmeister (1992) on particles solid surfaces. An empirical equation by Ahlert (1994) was used to complete the prediction method. Direct comparison was made between experimentally obtained results and the erosion profiles predicted by the CFD technique. It was found that excellent quantitative agreement could be obtained only after the rapid erosion of the sharp edge at the entrance to the straight choke had been accounted for in the computational mesh. This edge had a significant effect on the turbulent kinetic energy levels at the entrance to the straight choke and hence on the resulting erosion due to normal particle impacts against the walls. This study underlined the need to properly account for the effect of eroded geometry on subsequent fluid mechanics behavior (and hence particle transport). The same set of experimental data was

used to validate the work of Edwards *et al.* (1998). No reason was mentioned about the change in geometric profile. The agreement between the predictions and experiments were not quite so good.

A comprehensive experimental work was reported by Postlethwaite and Nesic (1993). They measured the erosion rates along the length of a tubular flow cell of type 304 (UNS S 30400) stainless steel carrying the dilute slurries of silica sand (0.43 mm diameter) and smooth glass beads of a similar size. The segmented test cell contained a sudden constriction, an expansion and a groove to create flow disturbances. Erosion rates were changed due to the altercation of pipe wall geometry. It was resulted from erosions at positions of high metal loss and localized erosion at downstream because of turbulence and particle dispersion. Smoothing the sand particles in the system halved the erosion rate. In this way, reduction in erosion rates obtained with the sand was of two orders of higher magnitude than that produced with the glass beads. These differences were attributed to surface micro roughness of the particles. Salama and Venkatesh (1983) proposed an alternative equation to that of the API. The authors included the effects of the fluid mixture density and particle diameter effects in their correlation. The accuracy of this proposed erosion equation in the pipe bends for slurry flows was demonstrated by a comparison with several multi loop tests that cover a broad range of liquid-gas ratios, sand size, and pipe size and by different investigators. They validated their model constants using tests conducted by four independent laboratories for geometries such as elbows and bends. Both CFD analysis and short experimental work suggested that the numerical erosion rate was lower for the elbows. But this effect decreased as the liquid to

gas ratio was increased. Wood *et al.* (2004) performed studies of erosion in an experimental setup consisted of an upstream straight section followed by a bend. The radius of curvature of the bend was of 1.2 bore diameters within a 78 mm diameter pipe test loop handling water-sand mixture at 10% by volume. The mean velocity was 3m/s. The authors proposed an erosion model by recognizing the two erosion mechanism of cutting and deformation erosion proposed by Forder *et al.* (1998). This proposed model included variables such as particle shape and material properties of both particle and the target material. The erosion predictions derived from this model, showed a good agreement with actual damage rates and patterns found in full-scale test looping. Moreover, the bend wear patterns were found to consist of various scales of ripples, indicating varying levels of sand intensity and scales of turbulence near to the walls.

Erosion estimation in a vertical pipe with sudden contraction was exyensively discussed by Badr *et al.* (2002) in their paper. The special case of two-phase turbulent flow with low particle concentration was investigated. Two mathematical models were used for the determination of fluid flow velocity field and calculation of solid particle trajectory respectively. Erosion model proposed by Wallace and Peters (2000) was used for predicting erosion rates. The effects of flow velocity and particle size were investigated in considering water flow in a carbon-steel pipe with contraction ration 2:1. The results showed strong dependence of erosion on both flow velocity and particle size. Moreover, presence of a flow threshold velocity below which erosion rate was negligibly small was determined. They found that a velocity of value 1m/s was too low to be accounted for any erosion to occur. The authors also showed that flow direction had very

little effect on the erosion phenomenon except for large particle diameter of 400 μm and moderate flow velocity of 5 m/s. Habib *et al.* (2004) reported erosion predictions with abrupt contraction of different contraction ratios for the case of two-phase (liquid and solid) turbulent flow with low particle concentration. A mathematical model based on the time-averaged governing equations of 2-D axi-symmetry turbulent flow was used for the calculations of the fluid velocity field. Lagrangian particle tracking approach was adopted for particle tracking. Three geometries of different contraction ratios were used to investigate the effects of Reynolds number and flow direction on erosion rate. The authors reported the influence of contraction ratio on local erosion rate. The authors pointed out a region close to the outside corner, where erosion did not take place due to very low velocity. They reported that the location of the maximum erosion was at the inner tip of the contraction. Their results proved that inlet velocity variations have a very significant effect on erosion. Erosion rate increased exponentially with the inlet velocity. They also indicated a benchmark for threshold velocity below which erosion became negligible (1m/s). The contribution of buoyancy was mentionable only for the case of low velocity of the continuous flow. Badr *et al.* (2005) reported a numerical investigation of erosion threshold velocity in a pipe with sudden contraction. They considered the axis of the pipe being vertical either in the direction of the gravity (down flow) or against it (up flow). Mathematical models for the calculations of fluid velocity vector field and the motion of the solids had been established. An erosion model was used to predict the erosion rate. The effects of the fluid flow velocity and particle size were investigated for one contraction geometry considering water flow in steel pipe. Strong dependence of erosion on both particle size and flow velocity was observed in their study. Direction of

the flow (up flow or down flow) had insignificant effect on erosion rates. The erosion critical area was found to be the inner surface of the tube sheet (connecting the two pipes) in the region close to the small pipe. Their results indicated the presence of a threshold velocity to be approximately 2m/s. Below this value, erosion effect was insignificant. The authors found out that for low velocities, effect of gravity on particle motion became significant. The effect of flow direction was found significant only for larger particle size (400 μm) and moderate flow velocity of 5 m/s. The authors reported strong dependence of erosion on the particle size ranging from 10 μm to 400 μm.

2.3.3 Literature Related to the Erosion of Choke Valves

A handful of studies have been published on the CFD-based erosion modeling of choke valves. In the paper, Nokleberg and Sontvedt (1998) presented erosion predictions for two types of choke valve: Needle and Seat, and External sleeve. Their method was based on the structured mesh version of the Fluent commercial CFD package, and so had difficulty in accurately reproducing the valve internal geometries. Nevertheless, the predictions did follow experimentally observed trends fairly well, both in terms of mass loss and wear distribution. Actual erosion tests for the two types of valve gave peak erosion rates around 2-3 times larger than calculated. Predictions were better for the Needle and Seat choke (where the internal geometry is fairly smooth and simple) than for the External sleeve choke valve. This would be due to geometry changes during the erosion process, which the CFD method did not account for. Forder *et al.* (1998) also considered Needle and Seat choke valves in their application of CFD-based erosion modeling techniques. Although detailed description was made of their technique; no

actual quantitative comparisons were made between experimental and predicted erosion of choke valves. A structured approach to mesh generation was followed (using the commercial code CFX) which limits the ability of the method to represent complicated geometries accurately. The only comparison presented by Forder *et al.* (1998) had been for a flat plate undergoing erosion by a fully submerged jet. Good agreement was obtained. A hybrid empirical erosion model was used to represent both ductile and brittle erosion mechanisms. Haugen *et al.* (1995) reported exhaustive test results of erosion characteristics of total twenty eight different materials including standard steel grades, solid tungsten carbide, coatings, and ceramics. They have determined an empirical model of erosion and reported erosion resistance for the materials. Their results showed that a longevity gain factor of up to 10^2 could be achieved by proper material selection. Increased longevity will lead to significant savings of the components concerned. Wallace and Peters (2000) reported a comprehensive CFD-modeling of multi-orifice choke valve. The authors proposed a semi-empirical equation by incorporating particle impact velocity and angle of impact. Their proposed erosion correlation had greater flexibility to be used in situation commonly encountered in the real life flow situations such as flow through abrupt constrictions. The authors compared experimental material loss with the predicted ones that showed significant closeness between the two. Moreover, comparisons of predicted pressure drop with experimental data indicated accuracy within 3% for a fully open valve. Particle trajectory study in their work revealed the predictions of erosive wear in multi orifice choke valves. The authors reported that further work would have to be performed to predict pressure drop across partially open orifice choke valve.

Wallace *et al*. (2004) reported solid particle erosion rates for valves in aqueous slurry flow. They proposed an Eulerian-Lagrangian model of the flow, in combination with the empirically developed equations for the mass removal of the industrially relevant component, valves. They examined two types of geometries: a relative simple geometry with basic geometrical features similar to real valve. Another one is a geometrically complex valve similar to that of a choke valve. They reported that due to variation in thegeometric features, the average erosion rates were under predicted by almost 60% for the simple geometries and by a factor 10 to 15 for the complex geometries. They concluded that the wear equations based on jet type erosion tests and neglecting the geometric changes partly accounted for this poor prediction of wear rates.

2.4 Objectives of the Present Work

Based on the literature review, it can be concluded that no work was published on the topic of the erosion of a pipe protruded in sudden contraction geometry. The overall objective of this study is to estimate the erosion rate of a pipe protruded in sudden contraction geometry. To achieve that, the following objectives are set:

1. Choosing and setting up of a proper turbulence model for solving the continuous flow in the geometry of interest. Subsequently, performing particle tracking calculations in the Lagrangian approach. Utilizing this information erosion rate of the protruded pipe will be calculated by choosing a suitable empirical model.

2. Validating the above mentioned erosion model with the experimental data available in the literature.

3. Conducting parametric studies of different variables related to flow condition (inlet flow velocity, particle diameter) and geometry of the present study (protruded pipe depth, thickness and contraction ratio of the pipe geometry).

4. Analyzing the above mentioned results to observe the influence of these parameters on the erosion rates of the protruded pipe. As such, different recommendations for future work would be made.

Chapter 3

Mathematical Formulation

The advent of the general-purpose commercial CFD (Computational Fluid Dynamics) codes has made it possible to predict fluid flow and particle motion through complex geometries. An extension of this capability is to extract the velocities and angles with which particles impact solid surfaces, and to somehow relate that information to erosive wear. The concept, known as the Lagrangian approach, is considered to have three stages:-

1. Predictions are made of the fluid flow field through the geometry of interest. The component geometry is used to create the computational mesh on which the governing equations of fluid flow will be solved. Appropriate boundary conditions are required before the flow solution can be obtained. The present work deals with the flow that is steady state, 2-D axi-symmetric and is considered to be turbulent. For fluid phase modeling of the present work, Renormalization-group (RNG) κ-ε model is applied. RNG κ-ε model is derived using a rigorous statistical technique called renormalization group theory. The RNG κ-ε model proves to provide accurate result (Wilcox, 2000) especially flows having strong streamline curvature, vortices, and rotation. In the present study, the flow is supposed to have higher

streamline curvature to occur near the protruded pipe. Keeping this view into consideration, RNG-k-ε model is chosen for solving the continuous flow instead of the standard k-ε model.

2. It is possible to track the movement of particles entrained within the fluid phase once the fluid phase behavior has been adequately predicted. By including the stochastic effect into particle tracking, a good number of particle trajectories are usually required in this step in order to obtain a good statistical representation of impact sites. When a sufficient number of tries is requested , the computed trajectories will include a statistical representation of the spread of the particle stream due to turbulence. In the present case, effect of turbulence is incorporated in order to get a good statistical representation of the particle tracks. In this study, around 4000-4500 particles are tracked at a time using the Lagrangian particle-tracking frame. Particle trajectories are calculated by solving the particle equation of motion for small time steps throughout the flow. When a particle strikes a solid surface, it looses some of its kinetic energy due to the collision.Therefore, it rebounds with a lower velocity (and possibly different angle) than at impact. Restitution coefficients are used to determine rebound velocity and angle.

3. The impact data generated by the particle trajectory calculations can be used to estimate the level of erosive wear. Equations are developed which relate particle impact properties (e.g. impact velocity and impingement angle) to the amount of material lost. These equations are generally semi-empirical, and will be specific to a certain material type. Successive impacts at each cell point on the surface are summed to give final

erosion predictions when all particle trajectories have been calculated.This three-stage procedure has the potential to assist flow component manufacturers in developing valves that are more resistant to solid particle erosion. Surfaces could be angled in ways that ensure particle impact angles cause the minimum amount of erosion damage. Surfaces receiving the greatest proportion of particle impacts could be reinforced at specific points.

The physical situations involving fluid flow are governed by the conservation principles of mass and momentum. These principles can be expressed in terms of partial differential equations. A close examination of these equations reveals that they posses a common form as proposed by Lapidus and Pinder (1982):

$$\oint \rho\phi v.dA = \oint \Gamma_{\phi} \nabla \phi.dA + \int_{V} S_{\phi} dV \qquad (3.1)$$

In equation (3.1), ϕ is any field variable and v is the velocity vector. This quantity describes the transport of scalar or vector quantity that takes place due to of convection and diffusion process. The first term in the general transport equation (3.1) is called the convection term. This represents the transport of property ϕ due to mass flow through the control surfaces. The second term represents diffusion of property ϕ due to its gradient in the flow field. The third term is the source term representing the rate of generation of the transport variable ϕ within the control volume.

3.1 General Governing Equations in Physical Space

3.1.1 Mean Flow Equations

Most flows occurring in the practical industrial applications are turbulent. In Von Karman's (1937) view: "*Turbulence is an irregular motion which in general makes it appearances in fluids, gaseous or liquid, when they flow past solid surfaces or even when neighboring streams of the same liquid flow past or over one another*." To provide a more representative definition of turbulence, Hinze (1975) offers the following revised definition: " *Turbulent fluid motion is an irregular condition of flow in which the various quantities show a random variation with time and space coordinates, so that statistically distinct average values can be discerned.* "

The crucial difference between visualization of laminar and turbulent flows is the appearance of eddying motion of a wide range of length scales in turbulent flows. A typical flow domain of 0.1m by 0.1 m with high Reynolds number turbulent flow might contain eddies down to 10 to 100 μm size. The fastest events take place with a frequency of the order of 10 KHz, so it is required to descretise time into steps of 100 μs.

The present day computing powers are far behind those required to simulate turbulent flows using direct numerical simulation (i.e. using full Navier Stokes Equations without any modeling assumptions about the structure of turbulence). Engineers need

computational procedures, which supply adequate information about the turbulent processes, avoiding the need of predicting the effects of each and every eddy in the flows. As turbulence consists of random fluctuation of the various flow properties, statistical approach is used. Reynolds (1985) introduced a procedure in which all quantities are expressed as the sum of mean and fluctuating parts. The time-averaged property of the flow provides equations governing mean- flow quantities, ϕ, largely. To predict the flow pattern of the continuous flow phase, the conservation equations for mass and momentum are solved together with the transport equation for the turbulence model.

3.1.2 Conservation of Mass (Continuity):

$$\frac{\partial}{\partial x_j}(\rho \overline{U}_j) = 0 \tag{3.2}$$

3.1.3 Momentum Conservation:

$$\frac{\partial}{\partial x_j}(\rho \overline{U}_i \overline{U}_{\bar{j}}) = -\frac{\partial p}{\partial x_i} + \frac{\partial}{\partial x_j}(\mu \frac{\partial U_i}{\partial x_j}) - \frac{\partial}{\partial x_j}(\rho \overline{u_i u_j}) \tag{3.3}$$

where p is the static pressure and the stress tensor $\rho \overline{u_i u_j}$ is given

$$-\rho \overline{u_i u_j} = \mu(\frac{\partial \overline{U}_i}{\partial x_j} + \frac{\partial \overline{U}_j}{\partial x_j}) - \frac{2}{3}\rho k \delta_{i_j} \tag{3.4}$$

where δ_{ij} is the Kroneker delta and $\mu_{eff} = \mu_t + \mu$ is the effective viscosity. The Kronecker, δ_{ij} is equal to 1 for i=j and equals to 0 for $i \neq j$ and $\mu_{eff} = \mu_t + \mu$ is the effective viscosity.

The above governing equations are time averaged; however, they no longer form a closed set due to the additional terms representing the transport of momentum of the fluctuation motion. Equations governing these fluctuating motions introduce additional unknown quantities and can only be solved when the turbulence correlations are used.

3.1.4 Modeling of Turbulence

The Navier-Stokes equations describe flow under laminar and turbulent regimes. Because of the existence of an extremely wide range of length and time scales in turbulent flows, the computational resources required for the exact numerical solution of turbulent flow is remarkably high. For most engineering applications, it is necessary to use turbulence models along with time averaged Navier-Stokes equations. The cautious application and interpretation of turbulence models have proved to be a valuable tool in engineering research and design, despite their physical deficiencies. No single turbulence model is universally accepted as being superior for all class of problems. The choice of a turbulence model depends on considerations such as the physics encompassing in the flow, the level of accuracy required and availability of computational resources. To make the most appropriate choice of a model for an application, one needs to understand the capabilities and limitations of the various options. The turbulence models most commonly used can be summarized in the following sections. The computational effort and cost in terms of CPU time and memory for each turbulence model is discussed herewith.

3.1.4.1 The Zero Equation Models

These include constant eddy viscosity and constant Prandtl mixing length models. These are early models and they are not available anymore in CFD packages.

3.1.4.2 The One-Equation Models

There is a one-equation model known as Spalart- Allmaras model. This model was designed specifically for aerospace applications involving wall-bounded flows and has been shown to give good results for boundary layers subjected to adverse pressure gradients. Due to these shortcomings, Spalart- Allmaras model is not applicable for the present case.

3.1.4.3 The Two-Equation Turbulence Models

The two-equation turbulence models are the widely used models for different flow conditions. These two equation turbulence models and their proposers names are shown in table 3.1:

Table 3.1: Different turbulence models and their proposers

Turbulence Model	**Proposed by**
Standard k-ε	Jones and Launder (1973)
Renormalization Group (RNG) κ-ε model	Yakhot and Orszag (1986)
Realizable κ-ε model	Shih et al. (1995)
κ-ω	Wilcox (1988)
RSM	Launder et al. (1975)

Although the Reynolds-averaged Navier-Stokes (RANS) equations represent transport equations for the mean flow quantities only with all the scales of the turbulence being modeled. The approach of permitting a solution for the mean flow variables greatly reduces the computational efforts. If the mean flow is steady, the governing equations will not contain time derivatives and a steady-state solution can be obtained economically. The Reynolds-averaged approach is generally adopted for practical engineering calculations.

3.1.4.4 The Standard κ-ε Turbulence Model

The standard k-ε model is a semi-empirical model based on model transport of equations for the turbulent kinetic energy (k) and its dissipation rate (ε). The model transport equation for k is derived from the exact equation, while the model transport equation for ε is obtained using physical reasoning and bears little resemblance to its mathematically exact counterpart. In the derivation of the k-ε model, it is assumed that the flow is fully turbulent, and the effects of molecular viscosity are negligible. The standard k-ε model is therefore valid only for fully turbulent flows. The turbulent kinetic energy, k and its rate of dissipation, ε is obtained from the following transport equations:

$$\rho \frac{Dk}{Dt} = \frac{\partial}{\partial x_j}[(\mu + \frac{\mu_t}{\sigma k})\frac{\partial k}{\partial x_i}] + G_k + G_b - \rho\varepsilon - Y_M \tag{3.5}$$

$$\rho \frac{D\varepsilon}{Dt} = \frac{\partial}{\partial x_j}[(\mu + \frac{\mu_t}{\sigma_k})\frac{\partial \varepsilon}{\partial x_i}] + C_{1\varepsilon}\frac{\varepsilon}{k}(G_k + C_{3\varepsilon}G_b) - C_{2\varepsilon}\rho\frac{\varepsilon^2}{k} \tag{3.6}$$

In these equations, G_k represents the generation of turbulence kinetic energy due to mean velocity gradients, G_b is the generation of turbulent kinetic energy due to buoyancy, Y_M represents the contribution of the fluctuating dilatation in compressible turbulence to the overall dissipation rate.

The term G_k representing the production of turbulent kinetic energy, is defined as

$$G_k = -\rho \overline{u_i' u_j'} \frac{\partial u_j}{\partial x_i} \tag{3.7}$$

To evaluate G_κ in a manner with the Boussinesq hypothesis,

$G_\kappa = \mu_t S^2$, where S is the modulus of the mean rate-of -strain tensor, defined as:

$S \equiv \sqrt{2 S_{ij} S_{ij}}$ with mean S_{ij} given by

$$S_{ij} = \frac{1}{2}\left(\frac{\partial u_i}{\partial x_j} + \frac{\partial u_j}{\partial x_i}\right) \tag{3.8}$$

Now, G_b is the generation of turbulent kinetic energy due to buoyancy.

$$G_b = \beta g_i \frac{\mu_t}{\mathrm{Pr}_t} \frac{\partial T}{\partial x_i} \tag{3.9}$$

where Pr_t is the turbulent Prandtl number for energy. For standard κ-ε models, the default value of Pr_t is 0.85.

β is the coefficient of thermal expansion and is defined by:

$$\beta = -\frac{1}{\rho}\left(\frac{\partial \rho}{\partial T}\right)_p \tag{3.10}$$

For high Mach number flow, the effect of compressibility on turbulence is included by "dilatation dissipation", which is normally neglected for incompressible flow. The "eddy" or turbulent viscosity, μ_t, is computed by combining k and ε as follows:

$$\mu_t = \rho C_\mu \frac{\kappa^2}{\varepsilon}$$, where Cμ is a constant (3.11)

Model Constants

The model constants $C_{1\varepsilon}$,$C_{2\varepsilon}$,σ_k and σ_ε have the following default values

$C_{1\varepsilon}$ =1.44, $C_{2\varepsilon}$=1.92, σ_k=1.0, σ_ε=1.3, C_μ=0.09.

$C_{3\varepsilon}$ will become 1 for buoyant shear layer for which the main flow is aligned with the direction of gravity. For buoyant shear layer that is perpendicular to the gravitational vector,$C_{3\varepsilon}$,will become zero. The default values have been determined from experiments with air and water for fundamentals turbulent shear flows including homogeneous shear flows and decaying isotropic grid turbulences. They have been found to work fairly well for a wide range of wall-bounded and free shear flows.

3.1.5 The RNG κ-ε Model

The RNG-based k-ε turbulence model is derived from the instantaneous Navier-Stokes equations, using a mathematical technique called "renormalization" group (RNG) methods. The analytical derivations result in a model with constants from those in the standard κ-ε model, and additional terms and functions in the transport equations for κ-ε.

Transport Equations for the RNG k-ε Model

The RNG k-ε model has a similar form to the standard k-ε model:

The kinetic energy of turbulence:

$$\frac{\partial}{\partial x_j}(\rho \overline{U}_j K) = \frac{\partial}{\partial x_j}(\frac{\mu_{eff}}{\sigma_k} - \frac{\partial k}{\partial x_j}) + G_k - \rho\varepsilon \quad (3.12)$$

The dissipation rate of kinetic energy in turbulence:

$$\frac{\partial}{\partial x_j}(\rho \overline{U}_j \varepsilon) = \frac{\partial}{\partial x_i}(\frac{\mu_{eff}}{\sigma_\varepsilon}\frac{\partial \varepsilon}{\partial x_i}) + C_{\varepsilon 1} G_k \frac{\varepsilon}{k} - (C_{\varepsilon 2} + C_{\varepsilon 3})\rho \frac{\varepsilon^2}{k} \tag{3.13}$$

In these equations, G_k represents the generation of turbulence kinetic energy due to the mean velocity gradients; and given by:

$$\rho \overline{u_i' u_j'} \frac{\partial u_j}{\partial x_i} \tag{3.14}$$

The quantities σ_k, σ_ε the effective Prandtl numbers for k & ε respectively, and where $C_{\varepsilon 3}$ is a function of the term k/ε and, this model is thus responsive to the effects of rapid strain and streamline curvature. The model values for $C_{\varepsilon 1}$ and $C\varepsilon_2$ are 1.42 and 1.68 respectively.

The turbulent viscosity μ_t is given by:

$$\mu_t = \rho C_\mu \frac{k^2}{\varepsilon} \tag{3.15}$$

With Cμ= 0.0845, derived using RNG theory. It is interesting to note that this value is very close to the empirically-determined value of 0.09 used in standard k-ε model.

3.2 Near-Wall Treatments for Wall-Bounded Turbulent Flows

Turbulent flows are significantly affected by the presence of the walls. Mean velocity fields are affected by through the no-slip condition that has to be maintained at the wall. However, turbulence is also changed by the presence of wall in non-trivial ways. Very close to the wall, viscous damping reduces the tangential velocity fluctuations, while kinematic blocking reduces the normal fluctuations. Towards the outer part of the near

wall region, the turbulence is rapidly augmented by the production of turbulent kinetic energy due to large gradients in mean velocity. The near-wall modeling significantly impacts the fidelity of numerical solutions, inasmuch as walls are the main source of mean vorticity and turbulence. In the near-wall region, solution variably changes with large gradients and the momentum and other scalar transports occur most vigorously. Numerous experiments have shown that the near-wall region can be largely subdivided into three layers. In the innermost layer, the flow is almost laminar-like and the (molecular) viscosity plays a dominant role in momentum transfer. This layer is called "viscous sublayer". There is an interim region between viscous sublayer and the fully turbulent layer where the effects of molecular viscosity and turbulence are equally important. In the outer layer, known as "fully turbulent layer", turbulence plays a major role. Figure 3.1 shows a schematic diagram about the subdivisions of the near wall region.

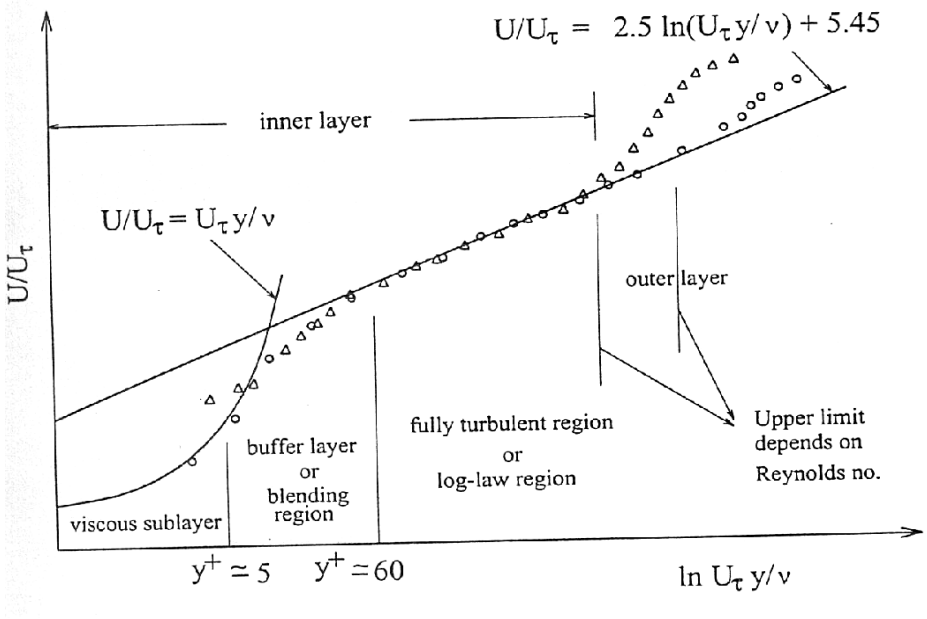

Figure 3.1: Subdivisions of the near wall region (Ref. Fluent 6.1 Documentation).

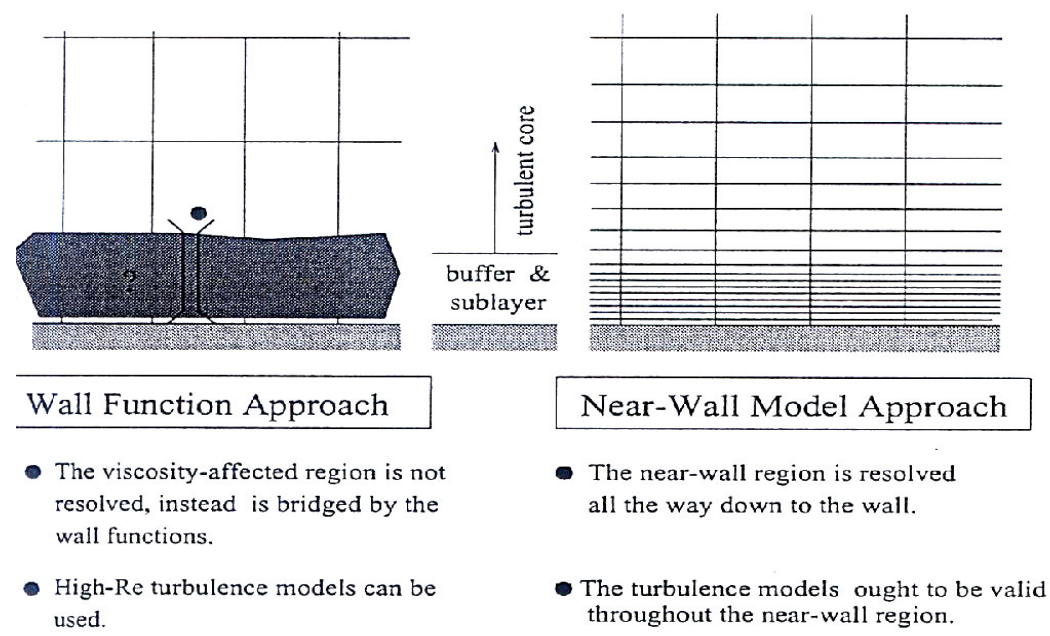

Figure 3.2: Near Wall treatment approach (Ref. Fluent 6.1 Documentation).

There are two approaches to modeling the near-wall region. In one approach, the viscosity-affected, inner region, (viscous sub layer and buffer layer) is not resolved. Instead semi empirical formulas called “wall functions” are used to bridge the viscosity affected region between the wall and the fully turbulent region. The use of wall functions obviates the need to modify the turbulence models to account for the presence of the wall. In another approach, the turbulence models are modified to enable the viscosity-affected region to be resolved with a mesh all the way to the wall, including the viscous sub layer. In most high Reynolds number flows, the wall function approach substantially saves computational resources. Due to viscosity-affected near wall region where the solution variables rapidly change. The wall function approach is popular because it is economical, robust, and reasonably accurate. It is a practical option for the near wall treatments for industrial flow simulations. In this work, standard wall function approach is used. The wall function approach is inadequate in situations where the low Reynolds number effects are pervasive in the flow domain. Such situations require near-wall models that are valid in the viscosity-affected region and accordingly integrable all the way to the wall.

3.3 The Particle Tracking

The particle tracking calculations aim to determine the particle trajectories as well as its velocity (magnitude and direction) before every impact either on the pipe walls or anywhere in the sheet. Such impact is not only important for calculation of solid surface erosion but also for determination of the particle trajectories during its subsequent course of motion following motion. Particle trajectories are obtained by Lagrangian

particle tracking which involves solution of particle equation of motion across many intervals through the flow. This method can be used to account for the influence of the particles on the fluid flow field, but it is thought that the low concentration of the particle present in the flows considered in this work (less that 1% by volume fraction) does not warrant a coupled solution of discrete and continuum. The particle equation of motion used to predict trajectories is written as follows in Cartesian co-ordinate as proposed by Wallace and Peters (2000):

$$\frac{du_p}{dt} = F_D(u - u_p) + g_x(\rho_p - \rho)/\rho_p + F_{vm} + F_{pg} + F_{sl} \tag{3.16}$$

where the first term at the right hand side is the drag force per unit particle mass and

$$F_D = \frac{18\mu}{\rho_p d_p^{\,2}} \frac{C_D \operatorname{Re}_p}{24} \tag{3.17}$$

Re_p is the relative particle Reynolds number given by:

$$\operatorname{Re}_p = \frac{\rho d_p \left| u_p - u \right|}{\mu} \tag{3.18}$$

The drag coefficient is provided by:

$$C_D = a_1 + \frac{a_2}{\operatorname{Re}_p} + \frac{a_3}{\operatorname{Re}_p^{\,2}} \tag{3.19}$$

where a's are the coefficients given by Morsi and Alexander (1972) for smooth spherical particles over several range of Re_p. The virtual mass force F_{vm} is the force required to accelerate fluid surrounding the particle, is given by

$$F_{vm} = (1/2)\frac{\rho}{\rho_p}\frac{d}{dt}(u - u_p) \tag{3.20}$$

Effects of the pressure gradient on particle motion are accounted for by $F_{\rho g}$, given as

$$F_{\rho g} = \frac{\rho}{\rho_s} u_p \frac{\partial u}{\partial x} \tag{3.21}$$

Forces which are not included in this work are Basset History force, which accounts for influence of changes in the flow field surrounding the particle from steady-state conditions (important when the particle acceleration is high). Another one was Magnus lift force, which results from the particle rotation at low Reynolds number .Moreover the Saffman lift force is not expected to contribute much to the particle motion (Meng and Van Der Geld, 1991).

3.4 Erosion Models

In the present work, model proposed by Wallace and Peters (2000) is chosen for erosion calculations. For erosion prediction, several models are available in the literature. Some are stated below:

Wallace and Peters (2000) provided the following formulae by using the empirical erosion equation suggested by Neilson and Gilchrist (1968).

$$\left.\begin{aligned} E &= \frac{1}{N_P}\left[\frac{(1/2)u^2{}_p \cos^2\alpha \sin 2\alpha}{\gamma} + \frac{(1/2)u^2{}_p \sin^2\alpha}{\sigma}\right]; for\,\alpha \le 45^o \\ E &= \frac{1}{N_P}\left[\frac{(1/2)u^2{}_p \cos^2\alpha}{\gamma} + \frac{(1/2)u^2{}_p \sin^2\alpha}{\sigma}\right]; for\,\alpha > 45^o \end{aligned}\right\} \tag{3.22}$$

Here E is termed as erosion rate, mg/g, γ & σ are the cutting wear and deformation wear coefficients having the values 33316.9 and 77419.7 (for carbon steel) respectively.

Keating and Nesic (2000) proposed a modified version of Finnie's erosion model. Their model equation is as follows:-

$$\left.\begin{array}{l} \text{For } \alpha \le 18.5^{o} \\ E = \dfrac{(u_p \sin\alpha - u_{cr})}{2p}\left[\dfrac{\rho_m}{1000}\right]\left[u_p \cos\alpha - \dfrac{3}{2}(u_p \sin\alpha - u_{cr})\right] \\ \text{For } \alpha > 18.5^{o} \\ E = \dfrac{(u_p \sin\alpha - u_{cr})^2}{12p}\dfrac{\rho_m}{1000}\dfrac{\cos^2\alpha}{\sin^2\alpha} \end{array}\right\} \quad (3.23)$$

In this model, E is denoted as erosion rate mg/g, u_p is particle velocity, m/s, u_{cr} is critical velocity for plastic deformation (as for steel 0.668), α is the impact angle, ρ_m is the target material density, p is the flow stress.

Finnie et al. (1992) proposed an erosion model as follows:

$$\left.\begin{array}{l} E\alpha\dfrac{2}{P}(\sin(2\alpha) - \dfrac{2}{P}\sin^2\alpha), \text{ for } \alpha \le \hat{\alpha} \\ \text{E } \alpha \ \dfrac{\cos^2\alpha}{1000}, \text{ for } \alpha \ge \hat{\alpha}, \text{ for } \alpha \ge \hat{\alpha} \end{array}\right\} \quad (3.24)$$

Where E=Erosion rate, mg/g

P = parameter defined by Finnie et al. (1992)

$\hat{\alpha}$ = almost equal to 14 degrees for most metals

Shirazi et al. (1995) proposed the following formulae:

$$Pn = \frac{\dot{s}}{\rho_m A N_p} E_{lc} x 31536000 \tag{3.25}$$

$\dot{s}$ denotes sand rate, kg/s

E_{lc}: stands for local erosion rate, mg/g

ρ_m: stands for density of target material

N_p: means number of particles throughput

A: denotes impingement area

Salama (1998) proposed his equation for erosion prediction in multiphase flow as follows:

$$Pn = \frac{1}{S_m} \frac{W V_{mix}{}^2 d_p}{D^2 \rho_{mix}} \tag{3.26}$$

Pn =Penetration rate, mm/year

W= sand production rate, kg/day

d_p= sand size, μm

ρ_{mix} = fluid mixture density, kg/m3

S_m= a geometric dependent constant defined by Salama (1998).

V_{mix}= fluid mixture velocity, m/s

Wang and Shirazi (2003) in their proposed model for long-radius elbows and bends eroded by sand in a liquid cited the following equations:

$$E = [A_W u_p^{1.73} f\ (\alpha) BHN^{-0.59}] \frac{1}{1000}$$

(3.27)

$$f(\alpha) = \{a''\alpha^2 + b''\alpha), 0 \le \alpha \le 15^0\}$$

$$= \{\ X\cos^2(\alpha)\sin(\alpha) + Y\sin^2(\alpha) + Z, 15^0 \le \alpha \le 90^0\ \}$$

where Aw is an empirical constant for wet surfaces, BHN is the Brinell hardness number of the target material, f_W (α) angle function. They also provided the formula for calculating local penetration rate:

$$Pn = [\frac{W}{\rho_m N_P A_i} E] x365 \tag{3.28}$$

where ρ_m= density of target material, N_p=number of particles, A_i=impingement area, Pn= mm/y.

Chen et al. (2004) proposed an erosion model that is based on the experimental data for two materials; Carbon steel and aluminum. As many literatures are not found to deal with erosion models other than different steel group; this model is of special important from that point of view. Moreover, this model is also interesting to make a comparison with the erosion results reported by Wallace and Peters (2000) for carbon steel.

$$\left.\begin{array}{l} E = AF_s u_p^{\ 2} f(\alpha) \\ f(\alpha) = \begin{cases} a_C\alpha^2 + b_C\alpha, for\alpha \le \varphi \\ x\cos^2\alpha\sin(w\alpha) + y\sin^2\alpha + z, for\alpha > \varphi \end{cases} \end{array}\right\} \tag{3.29}$$

φ, a_c, b_C, w, x, y, z are empirical constants depend on the material being eroded.

Wood et al. (2004) reported a model that is originally proposed by Hashish (1988) for low impingement angle. This model takes into account material properties for both the particle and target as well as particle shape. This approach of inclusion of the material property is not considered by many earlier models. Their model is as follows:

$$E=\begin{cases} \frac{100}{2\sqrt{29}}[(d_P/2)^3 * (\frac{u_P}{C_K})^n \ \sin 2\alpha\sqrt{\sin\alpha}]x0.031536 \\ C_K = \sqrt{\frac{3\sigma R_f^{\ 0.6}}{\rho_P}} \end{cases} \tag{3.30}$$

Here,

d_p= diameter of the particles

u_p= particle velocity

σ= plastic flow stress, Pa

ρ_p = particle density, kg/m^3

α=impingement angle, radians.

3.5 Problem Statement and Boundary Conditions

The problem considered is that of solid particle erosion of a pipe protruded in a sudden contraction. Figure 3.3 shows the schematic diagram of the turbulent flow through a sudden contraction. The Cartesian coordinate system is chosen. The large pipe of diameter r_1 is connected to a small pipe of diameter r_2, through a sudden contraction joint. The small diameter pipe is protruded into the contraction section and the axes of both pipes are vertical resulting in an axisyymetric flow field. The fluid medium is water at 20^{0}C (ρ=998 kg/m^3, μ=1.003 mPa.s) and the flow is considered steady, incompressible,

and turbulent. The solid particles acting as eroding materials are sand particles of spherical shape with density 2668 kg/ m^3.The sand concentration is considered less than 10^{-3} (by volume) resulting in a dilute particle concentration. In such case, it is widely accepted to assume that the effect of particle motion on the fluid flow field is negligibly small. The same assumption is made by Lu et al. (1993), Shirazi et al. (1995), Edwards et al. (2000), Keating and Nesic (2000), Wallace and Peters (2000). In the present study, the fluid properties are considered constant throughout. The contraction ratio in this work is defined as the ratio of the small bore pipe diameter to the large bore pipe diameter. The material used for the pipe configuration was carbon steel. Particular form of the transport equation, which governs the flow process, is presented in equations (3.2-3.15). The Lagrangian particle tracking of sand particles was carried out using equations are (3.16) including stochastic effect and particle rebound behavior. Finally, erosion was modeled by using the pertinent particle impact data (velocity and impingement angle) in any of the

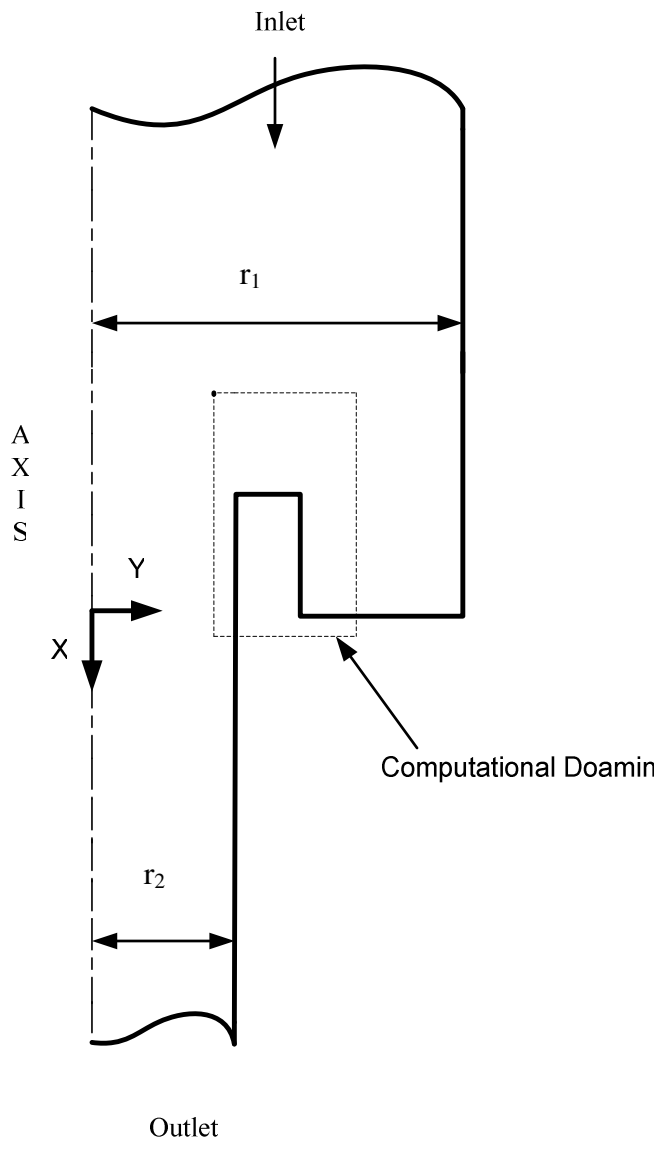

Figure 3.3: Schematic diagram of the present work and computational domain.

suitable erosion model, reported in different literature. The erosion models are given in the equations (3.22-3.30). In the present work, equations (3.22) and equation (3.25) are used for total erosion rates and penetration rate calculations respectively.

3.5.1 Boundary Conditions

On each of the computational points, boundaries conditions are required to solve the differential equations. Four different types of boundaries exist in the problem. They are the inlet section, the outlet section, the solid walls, and the axis of symmetry respectively.

Solid Walls

u=0, v=0 (3.31)

k And ε : If the law of wall is applied, then it is supposed that the first computational point close to the wall is designated as P. At this point, the law of wall for velocity U_p yields

$$|U_p| = \frac{u^*}{\kappa}\ln(E' y_p^+) \qquad (3.32)$$

Here u^* is called the friction velocity and y_p^+, represents a dimensionless distance from point P to the wall defined as

$$u^* = \left(\frac{\tau_\omega}{\rho}\right)^{\frac{1}{2}} \quad , \qquad (3.33)$$

$$y_p^+ = \frac{\rho y_p u^*}{\mu} \tag{3.34}$$

where τ_ω is the shear stress at the wall.

κ is the Von Karman constant.

E' is a roughness parameter

y_p is the actual distance from point P to the wall for all mesh points located in the region, $y_p^+ < 11.225$ where laminar stress-strain relationship is applicable. While for $y_p^+ > 11.225$, the logarithmic law is to be employed. Assuming the case of $y_p^+ >$ 11.225, the turbulent sub-layer is in local equilibrium. So the rate of κ is exactly equal to its destruction rate. This leads to

$$\frac{\mu_t}{\rho}\left(\frac{\partial u}{\partial y}\right)^2 = \varepsilon \tag{3.35}$$

By further supposing that the shear stress is constant in the sub-layer ($\tau_p=\tau_\omega$).One can use the logarithmic law to write

$$k = \frac{u^{*2}}{\sqrt{C_\mu}} \tag{3.36}$$

$$\varepsilon_P = \frac{u^{*3}}{\kappa y_p^+} \tag{3.37}$$

Using the above relations yield to the non-linear equation:

$$\left|U_P\right| = \frac{u^*}{\kappa}\ln\left(\frac{E'\rho y_p^+ u^*}{\mu}\right) \tag{3.38}$$

The velocity U_p is known from the solution of the momentum equation. The values of k_p and ε_p are used to calculate the turbulent viscosity and serve as boundary conditions (Dirchlet) for the rest of the bulk domain.

Inlet conditions

u= fully developed, i.e., the velocity profile is assumed the same as that of a fully developed turbulent pipe flow.

Outlet

The flow extends over a sufficiently long domain so that it is fully developed at the exit section.

$$\frac{\partial \phi}{\partial x} = 0 \tag{3.39}$$

Symmetric axis:

Here the radial derivative is set equal to zero.

$$\frac{\partial \phi}{\partial r}\Big|_{r=0} = 0 \tag{3.40}$$

Chapter 4

Numerical Procedure

4.1 Introduction

Numerical methods are powerful tools for solving problems related to fluid dynamics, heat transfer and other engineering problems when these cannot be handled by exact analysis due to nonlinearities, complex geometries and complicated boundary conditions. A numerical solution of a differential equation consists of a set of numbers from which the distribution of the dependent variable, ϕ, can be constructed. Derivation of the finite difference equations is obtained by discretizing the partial differential equations. Thus, a preliminary idea about the task of a numerical method can be obtained by considering a flow situation. The values of the dependent variables are considered at a finite number of locations called the grid points in the computational domain. The entire flow domain is divided into the control-volumes with grids at their geometric centers and all the variables defined at those grid points. From the differential equations governing the chosen variables, algebraic equations are derived for the grid-point values of the variables. Therefore, the method includes the tasks of formulating algebraic equation for these unknowns and prescribing an algorithm for solving these equations.

Therefore, some basic steps required to solve the flow problems are:

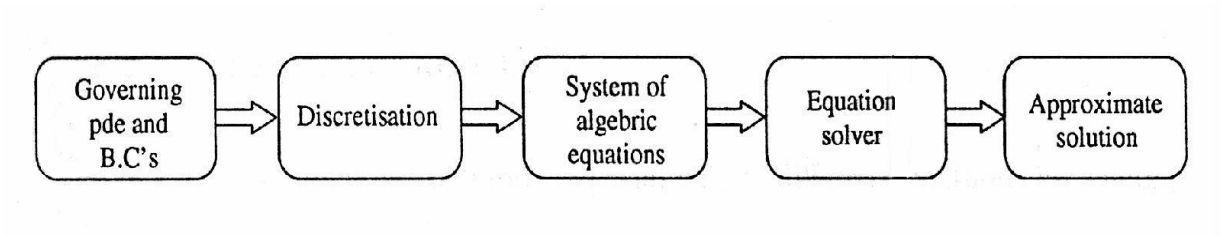

Figure 4.1: Overview of the computational procedure.

Thus, some prior knowledge of the background of the problem are required to formulate a numerical solution. Among other things, the order of magnitude of certain numerical data of the problem should also be accounted for.

These numerical methods can be categorized into*:*

1. Finite-Difference method.
2. Finite-Element method.
3. Finite-Volume method.
4. Boundary-Element method.

In this study finite- volume approach is adopted for solving the continuous phase. There are some basic properties of numerical solutions that determine their level of accuracy. These properties are convergence, consistency, stability.

Convergence is the property of a numerical method to produce a solution that approaches the exact solution as the grid spacing, control volume size or element size is reduced to zero. **Consistency** is the property of a numerical method to produce systems of algebraic equations which can be demonstrated to be equivalent to the original governing partial differential equations as the grid spacing tends to zero. **Stability** is associated with the growth or damping of errors as the numerical method proceeds and hence it describes whether the dependent variable is bounded.

In CFD, there is a need of codes that produce physically realistic results with good accuracy in simulations with finite (sometimes quite coarse) grids. Patankar (1980) has formulated rules, which yield robust finite-volume calculation schemes. The three crucial properties of robust methods include:

- Conservativeness.
- Boundedness.
- Transportiveness.

Conservativeness is the property of a numerical scheme, which is associated with the consistent expressions for fluxes of the fluid property through the cell faces of adjacent control volumes. **Boundedness** is akin to stability and requires that the solution of a linear problem without source to be bounded by the maximum and minimum boundary values. Boundedness can be achieved by placing restrictions on the magnitude and signs of the coefficients of the algebraic equations. Although flow problems are non-linear, it is

important to study the boundedness of a finite volume scheme for closely related but linear, problems. **Transportiveness** must account for the directionality of influencing in terms of the relative strength of diffusion to convection. The proposed work also deals with a steady case involving convective phenomena. Therefore, concentration will be focused on conservativeness, boundedness and transportiveness of the solution, calculated by the CFD techniques.

4.2 Discretization

The discretization process is essentially an exercise of engineering judgment. The number, shape, size and configuration of the discrete volumes (control volumes) must be in such a way that the original body is simulated as close as possible. The general objective of such a discretization is to divide the flow domain into finite control volumes sufficiently small so that the simple models can adequately approximate the true solution. At the same time, one must remember that too fine a subdivision may cause extra computational effort.

For a given differential equation, the discretization equations can be obtained in various ways:

1. Taylor Series Formulation.
2. Variational Formulation.
3. Method of Weighted Residuals.
4. The Finite Volume Method.

In the present work, the finite volume approach is adopted.

4.2.1 The Finite-Volume Method

In this method, the calculation domain is divided into a number of non-overlapping control volumes such that there is one control volume surrounding each grid point. The differential equation is integrated over each control volume. Profiles (such a step-wise and piecewise-linear profiles), expressing the variation of field variable (temperature, pressure, velocity, species mass fraction, etc.) between the grid points, are used to evaluate the required integrals. The result is the discretization equation containing the values of field variable for a group of grid points. The discretization equation thus obtained in this manner expresses the conservation principle of the field variable for the finite control volume, just as the differential equation expresses it for an infinitesimal control volume. Several techniques of numerical analysis exist. Among them most famous are Finite difference, finite volume, and finite element, spectral and pseudo-spectral methods. The finite volume technique is used in the present simulation for its simplicity and accuracy.

4.3 Discretization of the Transport Equations

Discretization process of the equations can be illustrated by considering the steady-state conservation equation for transport of a scalar quantity,ϕ. This is demonstrated by

the following equation written in integral form for an arbitrary control volume V as follows:

$$\oint \rho\phi v.dA = \oint \Gamma_\phi \nabla\phi..dA + \int_V S_\phi dV \tag{4.1}$$

where ρ is the density, v is the velocity vector, A is the surface area vector, Γ_ϕ is the diffusion coefficient for ϕ, S_ϕ is the source term of ϕ per unit volume and $\nabla\phi$ is given by

$$\nabla\phi = \left(\frac{\partial\phi}{\partial x}\right)\hat{i} + \left(\frac{\partial\phi}{\partial y}\right)\hat{j} \tag{4.2}$$

The above equation is applied to each control volume or cell in the computational domain. Now discretization of the above mentioned steady state diffusion equation for general transport property ϕ is given by

$$\nabla.(\rho u\phi) = \nabla.(\Gamma grad\phi) + S_\phi \tag{4.3}$$

The integration over a control volume gives

$$\int_{CA} n.(\rho\phi u)dA = \int_{CA} n.(\Gamma grad\phi)dA + \int_{CV} S_\phi dV \tag{4.4}$$

Applying divergence theorem, to the above equation, the following form is obtained

$$\frac{\partial}{\partial x}(\rho u\phi) + \frac{\partial}{\partial y}(\rho v\phi) = \frac{\partial}{\partial x}(\Gamma\frac{\partial\phi}{\partial x}) + \frac{\partial}{\partial y}(\Gamma\frac{\partial\phi}{\partial y}) + S \tag{4.5}$$

For the purpose of solving the flow domain is overlaid with a number of grids whose center points or nodes denote the location at which all variables except velocities are calculated. The latter are computed at locations midway between the two pressure points. Thus, the normal velocity components are directly available at the control volume faces, where they are needed for the scalar transport convection diffusion computations. The nodes of a typical grid cluster for two dimensions are labeled as P, N, S, E, and W. The

integration of each term in the above mentioned general equation (4.5) can be obtained with reference to the control volume for a typical node P with four nearest neighbors N, S, E, and W, in the spatial domain.

4.4 Domain Discretization

The first step in the finite-volume method is to divide the domain into discrete control volumes. The boundary of control volume is positioned mid way between adjacent nodes. Thus, each node is surrounded by a control volume or cell. It is common practice to set up control volumes near the edge of the domain in such a way that the physical boundaries coincide with the control volume boundaries. The nodal system is described in the Figure 4.2. The key step of finite-volume method is the integration of the governing equation over a control volume. For the above mentioned control volumes this integration gives,

$$\int_{\Delta V} \frac{\partial}{\partial x}(\rho u \phi) dx.dy + \int_{\Delta V} \frac{\partial}{\partial y}(\rho v \phi) dx.dy = \int_{\Delta V} \frac{\partial}{\partial x}(\Gamma \frac{\partial \phi}{\partial x}) dx.dy + \int_{\Delta V} \frac{\partial}{\partial y}(\Gamma \frac{\partial \phi}{\partial y}) dx.dy + \int_{\Delta V} S_{\varphi} dV \qquad (4.6)$$

So, noting that $A_{e=}A_W=\Delta y$ and $A_n=A_s=\Delta x$, the following relation is obtained:

$$[(\rho u A \phi)_e - (\rho u A \phi)_w] + [(\rho v A \phi)_n - (\rho v A \phi)_s] = [(\Gamma A \frac{\partial \phi}{\partial x})_e - (\Gamma A \frac{\partial \phi}{\partial x})_w] + [(\Gamma A \frac{\partial \phi}{\partial x})_n - (\Gamma A \frac{\partial \phi}{\partial x})_s] + \bar{S} \Delta V$$

(4.7)

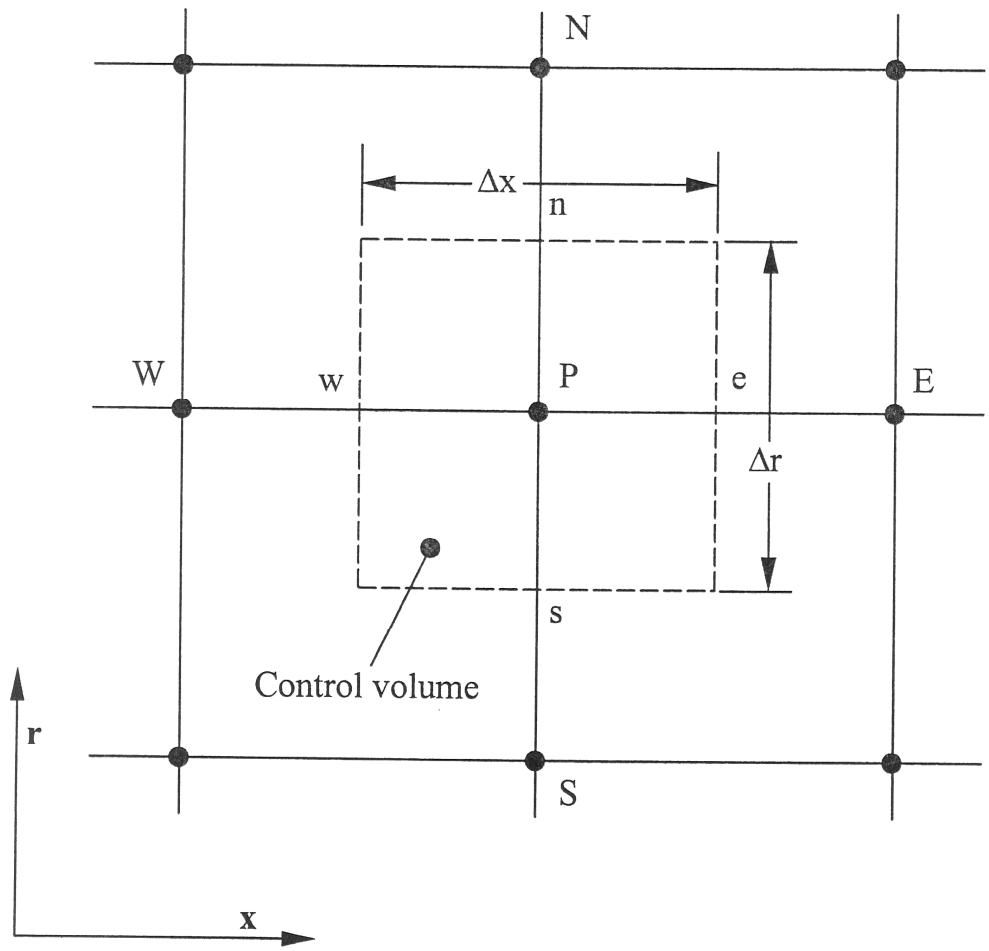

Figure 4.2: Control Volume for 2-D situation.

The flow must satisfy continuity and accordingly,

$$\frac{\partial(\rho u)}{\partial x}+\frac{\partial(\rho v)}{\partial y}=0 \tag{4.8}$$

In addition, its integration over the control volume gives

$$[(\rho uA)_e-(\rho uA)_w]+[(\rho vA)_n-(\rho vA)_s]=0 \tag{4.9}$$

The nonlinearity of the source term can be removed by representing it in a linear form

$$\bar{S}\Delta V=S_u+S_p\phi_p \tag{4.10}$$

Using linear central differencing approximation, it can be written as:

Flux across west face= $\Gamma_w A_w \frac{\partial\phi}{\partial x}\Big|_w=\Gamma_w A_w \frac{(\phi_p-\phi_w)}{\delta x_{wp}}$ (4.11)

Similar expressions can be written for flux through other faces.

To obtain discretized equations for the convection or diffusion problem, it must approximately the terms in the above equation. It is convenient to define two variables F and D to represent the convective mass flux per unit area and diffusion conductance at cell faces: F=ρ u and D= $\frac{\Gamma}{\delta x}$.

The cell face values of the variables F, D, Pe can be written as

$F_w=(\rho u)_w$, $D_w=\frac{\Gamma_w}{\delta x_{wp}}$, $P_w=\frac{F_w}{D_w}$.

For the convective terms for a uniform grid, it can be written the cell face values of property ϕ as $\phi_e = \frac{(\phi_{p-}\phi_E)}{2}$ and similarity for other face values.

The general discretized equation form for interior nodes reduces to:

$$a_p\phi_p=a_w\phi_w+a_E\phi_E+a_N\phi_N+a_s\phi_s+S_u \tag{4.12}$$

and from conservation equation, it can be written as $(F_E-F_W)+(F_N-F_s)=0$ where

$$a_W = D_W A(|P_W|)\|F_W, 0\| \tag{4.13}$$

$$a_E = D_E A(|P_E|)+\|-F_E, 0\| \tag{4.14}$$

$$a_s = D_s A(|P_S|)+\|F_s, 0\| \tag{4.15}$$

$$a_N = D_N A(|P_N|)+\|-F_N, 0\| \tag{4.16}$$

$$a_P = a_{W+}a_E + a_S + a_N - S_P A \tag{4.17}$$

The value A ($|P|$) for the upwind scheme is 1.0 (Patanker,1980).

In the present work, the first and second order upwind schemes have been used.

4.4.1 First –Order Upwind Scheme

In the first-order upwind scheme, quantities at cell faces are determined by assuming that the cell-centre values of any field variable represent a cell-average value and hold throughout the entire cell; the face quantities are identical to the cell quantities. Thus, in the first-Order up winding, the face value ϕ_f is set equal to the cell-centre value of ϕ in the upstream cell.

4.4.2 Second Order Upwind Scheme

In the Second Order Upwind Scheme, quantities at the cell faces are computed using a multidimensional linear reconstruction approach introduced by Barth and Jesperson (1989). In this approach, higher-order accuracy is achieved at all cell faces through a Taylor series expansion of the cell-centered solution about the cell centroid. Thus, when second-order up winding is selected, the face value ϕ_f is computed using the following expression:

$$\phi_f = \phi + \nabla\phi.\Delta s \tag{4.18}$$

where $\phi$and $\Delta\phi$ are the cell-centered value and its gradient in the upstream cell, and Δs is the displacement vector from the upstream cell centroid to the face centroid. This formulation requires the determination of the gradient $\nabla\phi$ in each cell. This is computed using the divergence theorem, which in discrete form can be written as

$$\nabla\phi = \frac{1}{V}\sum_{f}^{N_{faces}} \tilde{\phi}_f A \tag{4.19}$$

Here the face values $\tilde{\phi}_f$ are computed by averaging ϕ from two cells adjacent to the face. Finally the gradient $\nabla\phi$ is limited so that no new maxima or minima are introduced.

4.5 Solution Procedure

4.5.1 Grid Generation

To save the computational time a variable size grid is constructed to cover the computational domain. A fine grid is used in the regions (near walls) where large variation of flow variables viz. velocity, are expected. Figure 4.3 shows the grid system for the current study.

4.5.2 Computation of the Flow Field

The solution of the general transport equation presents two new problems:

- The convective term contains non-linear inertia terms.
- The continuity, momentum, energy, species and turbulence equations, represented, are intimately coupled because every velocity component appearing in each equation.

Both the problems associated with the non-linearities in general equation and the pressure velocity linkage can be resolved by adopting an iterative solution strategy such as SIMPLE (Semi-Implicit Method for Pressure-Linkage Equations) algorithm of Patankar (1980). Before outlining the algorithm, it is very important to explain the grid staggering, which is the first step to the SIMPLE algorithm. The finite volume method starts with the

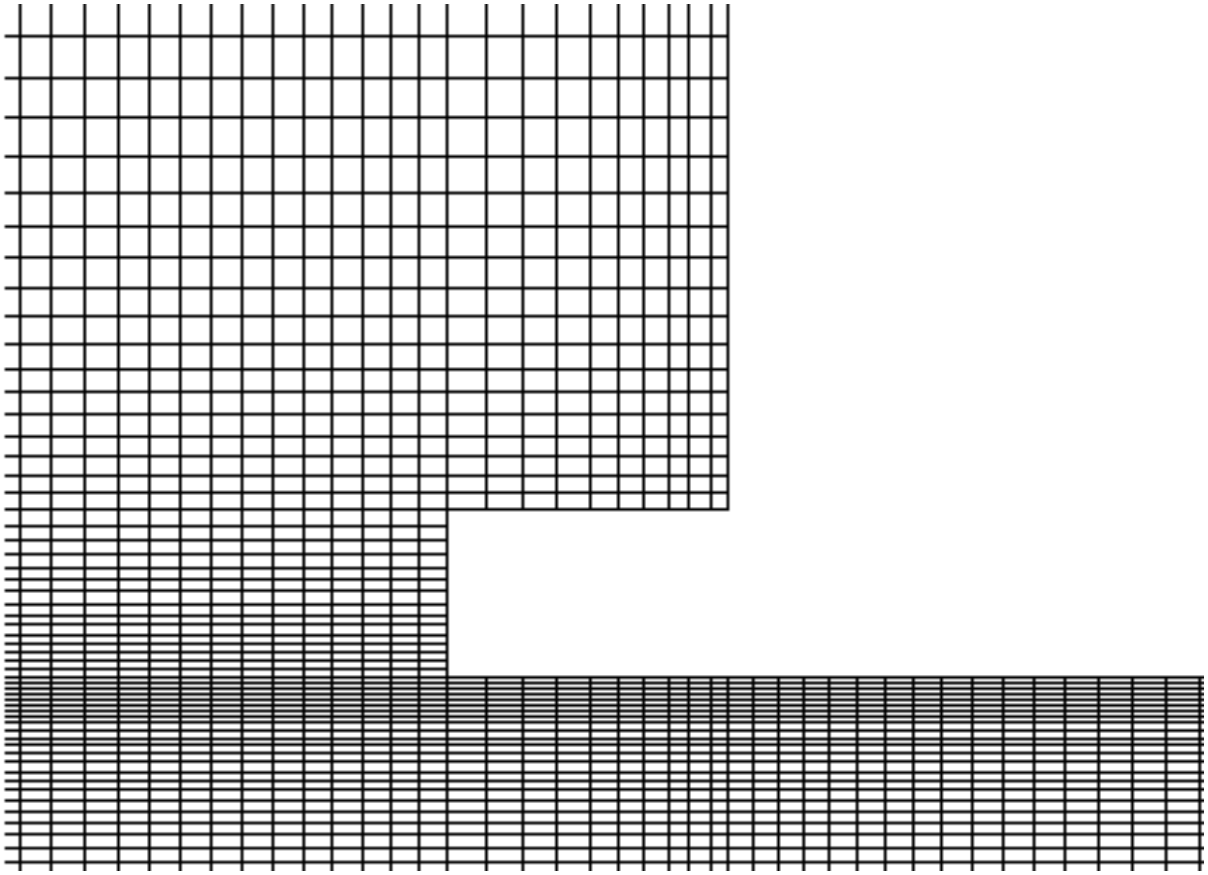

Figure 4.3: Magnified view of grid around the protruded pipe.

discretization of the flow domain and of the general transport equation. First, there is a need to decide where to store the velocities. If the velocities are defined at the scalar nodes (at which scalars, such as pressure and temperature, are defined), the influence of pressure is not properly represented in the discretized momentum equations. A remedy for this problem is to use a staggered grid for the velocity components. The idea is to evaluate scalar variables such as, pressure, density, temperature, species concentration, turbulence kinetic energy and turbulence dissipation, at ordinary nodal points but to calculate velocity components on staggered grids centered on the cell faces. In Figure 4.4, unbroken lines (grid lines) are numbered by means of capital letters I-1, I, I+1 and., J- I, J, J +1 in the axial and radial directions respectively whereas the dashed lines that construct the scalar cell faces 3 denoted by lower case letters i— l, i, i+l, and j—1, j,j+1 in the axial and radial directions respectively. A subscript system based on this numbering allows defining the locations of grid nodes and cell faces with precision. Scalar nodes, located at the intersection of two grid lines, are identified by two capital letters: point P in Figure 4.4 is denoted by (I, J). The staggering of the velocity avoids the unrealistic behavior of the discretized momentum equation for spatially oscillating pressures. A further advantage of the staggered grid arrangement is that it generates velocities at exactly the locations that they are required for the scalar transport-convection-diffusion-computations. No interpolation is required then.

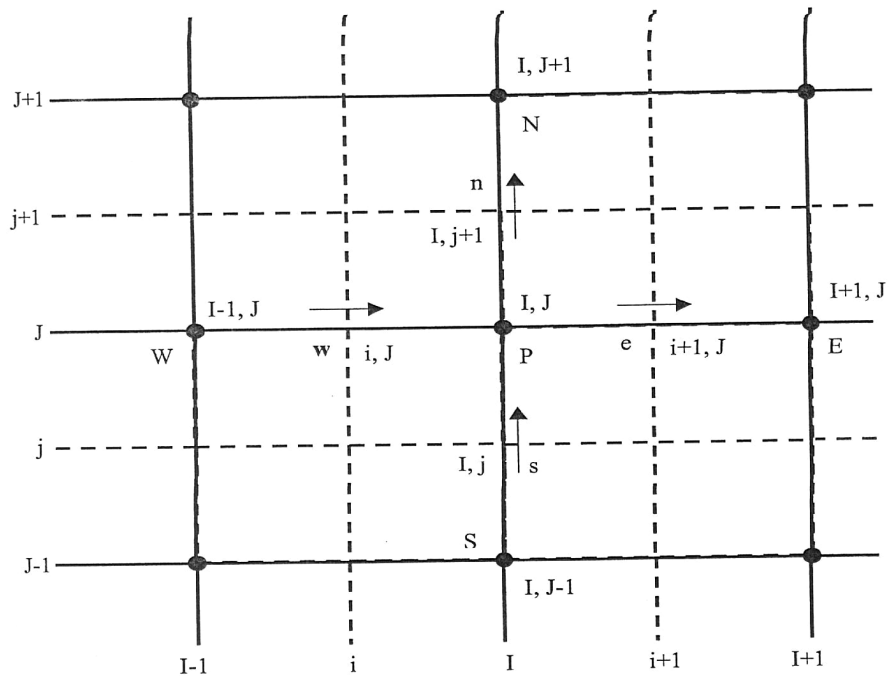

Figure 4.4: Staggered grid arrangement for velocity components.

4.5.3 Solution Algorithm for Pressure-Velocity Coupling

If the pressure field, which appears as a major part of the source term, is unknown then the following equation applied at all nodal points yield a set of algebraic equations but the resulting velocity field may not satisfy continuity equation:

$$a_p\phi_p = a_w\phi_w + a_E\phi_E + a_N\phi_N + a_s\phi_s + S_u \tag{4.20}$$

The problems of determining the pressure and satisfying the continuity are overcome by adjusting the pressure field using pressure-velocity coupling. SIMPLE algorithm by Patankar and Spalding (1972) is used for the pressure-velocity coupling. The acronym SIMPLE stands for Semi-implicit Method for Pressure-Linked Equations. In this algorithm, the pressure field p^* is first assumed. the discretized momentum equations are then solved using the assumed pressure field to yield velocity components u^* and v^*. Now the corrections, p', defined as the difference between the correct pressure field p and the assumed pressure field p^*, is calculated and a better approximation of the pressure field can be obtained using $p = p^* + p'$. Similarly the velocity components are corrected by adding the increments u' and v' to the assumed velocity components u^* and v^*, the whole process of the SIMPLE algorithm is explained in the flow diagram at Figure 4.5.

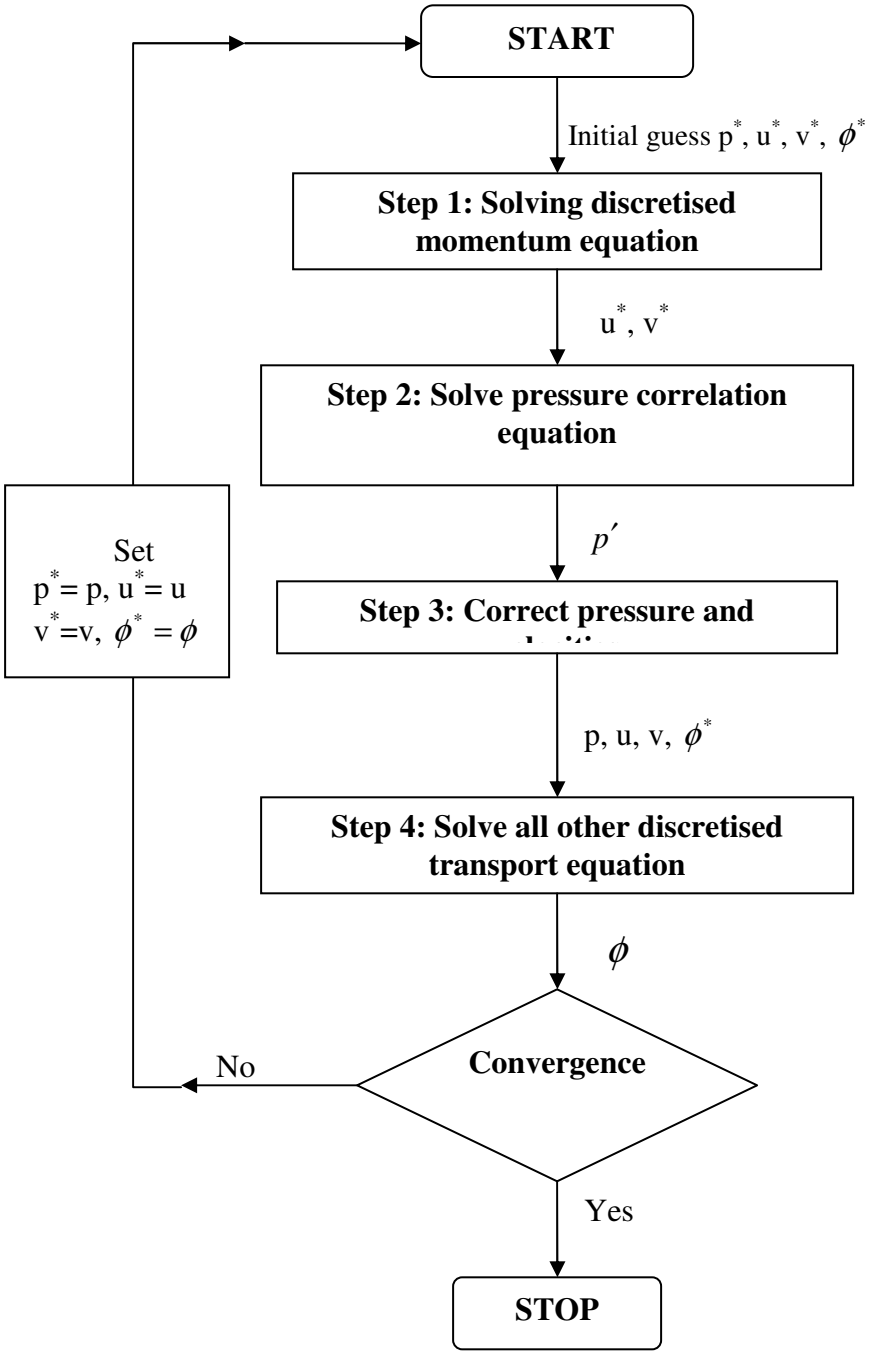

Figure 4.5: Diagram of SIMPLE algorithm.

4.5.4 The Calculation Procedure for the Flow Field

In this process, the governing equations are solved sequentially (i.e. segregated from one another). Since the equations are non-linear, several iterations of the solution loop must be performed before a converged solution is obtained. Therefore, the steps involved are:

1. Fluid properties are invariant in this problem.
2. The u and v momentum equations are solved in turn using the current values for pressure and face mass flow fluxes in order to update the velocity field.
3. Since velocities obtained in Step 2 may not satisfy the continuity equation, a pressure correction is applied. This satisfies the continuity equation (SIMPLE algorithm) and the linearized momentum equations. The pressure correction equation is solved and resulting pressure and velocity fields are obtained.
4. Equations for scalars such as turbulence kinetic energy, dissipation rate are solved using the previously updated values of these variables.
5. A check for convergence of equation set is made.

These steps are continued until the convergence criterion is satisfied. Figure 4.6 represents the steps involved in the calculation procedure.

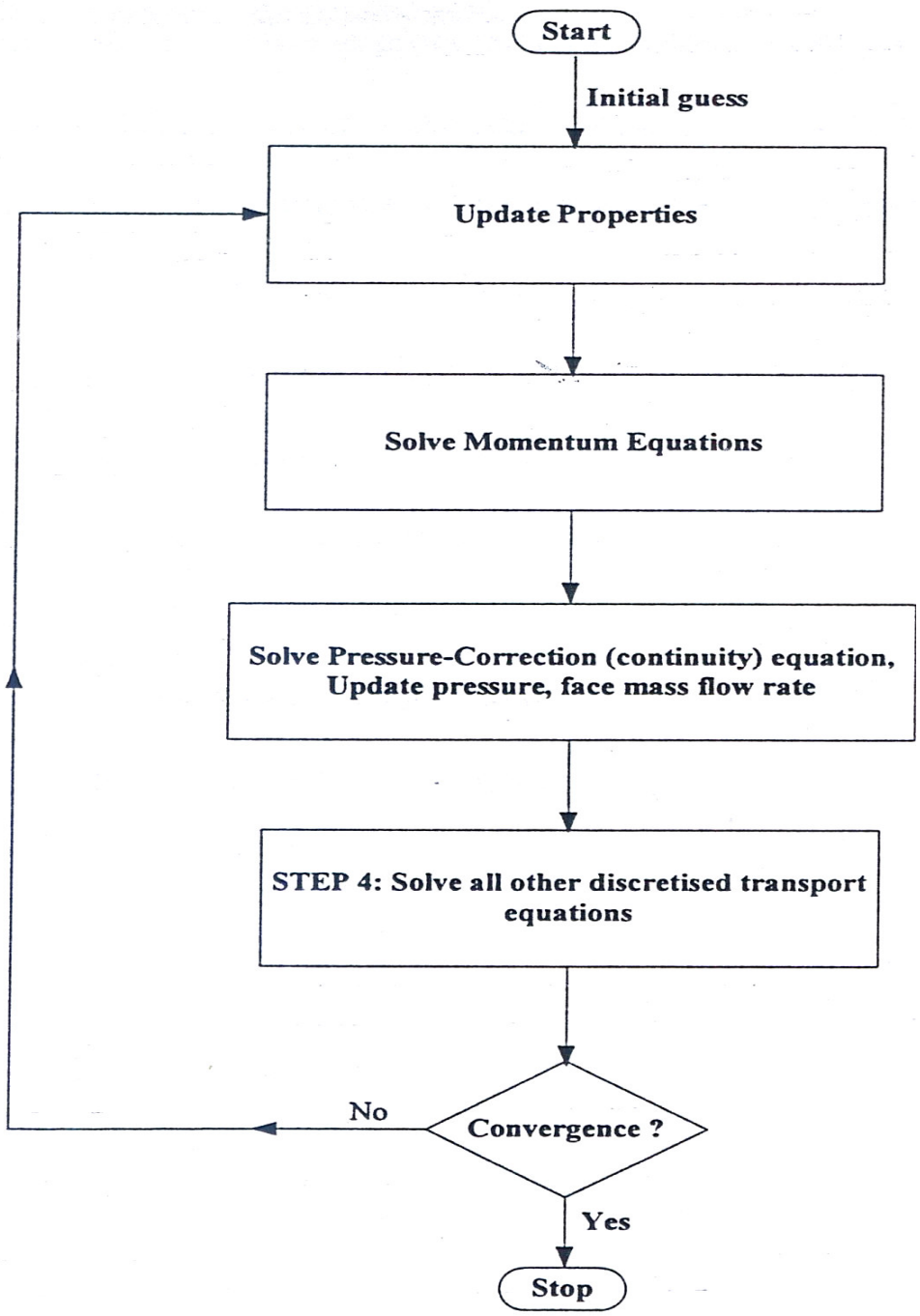

Figure 4.6: Flow Chart of solution algorithm.

4.5.5 Convergence Criteria

The use of an iterative solution method necessitates the definition of a convergence and stopping criteria to terminate the iteration process. The measure of convergence is a norm on the change in the solution vector between successive iterations. The iterative algorithm is terminated after a fixed number of iterations if the convergence has not been achieved. This criterion is used to prevent slowly convergent or divergent problems from wasting computation time. Convergence in this present study is defined to have been obtained after all the following criteria achieved.

Changes in the x-and y-velocity component are less than	$1x10^{-6}$
Changes in the turbulence kinetic energy is less than	$1x10^{-6}$
Changes in the turbulence dissipation rate is less than	$1x10^{-6}$

4.6 The Calculation Procedure of Particle Tracking

Wallace and Peters (2000) proposed the particle equation of motion used to predict trajectories to be written as follows in the Cartesian co-ordinates:

$$\frac{du_p}{dt} = F_D(u - u_p) + g_x(\rho_p - \rho)/\rho_p + F_{vm} + F_{\rho g} + F_{sl} \tag{4.21}$$

In the equation 4.21, the drag force per unit particle mass term is represented by $F_D(u - u_p)$, where $F_D=3C_D\mu Re_p/(4\rho_p D_p^2)$. In the present study, due to low particle concentration, the particle motions are considered non-interacting and the dominant force acting on the particle is the drag force.

The virtual mass force, $F_{vm,}$ takes care of the force required to accelerate the fluid surrounding the particle. This force is specifically important when the density of the fluid is more than that of the particle. In the present case, this is not true. So, the virtual mass force is neglected. The pressure gradient is denoted by, $F_{\rho g}$, arises from the influence of pressure gradient in the flow that acts on every volume element of the flowing medium. In the present study the pressure does not vary significantly over a distance of one particle diameter, a condition that is normal for reasonably small particles. As a result, the pressure gradient force is neglected. There are two other forces that can be mentioned are Magnus lift force and Besset history function force. Magnus lift force is significant when there are particle rotations. Also the Besset history force is counted when there is flow unsteadiness. These two forces are neglected due to low particle acceleration. Wallace and Peters (2000) showed that Saffman's lift force, F_{sl}, does not contribute greatly to the particle motion. Another force known as "thermophoretic force" is neglected in the particle motion as in the present case there is no temperature gradient. Similarly, Brownian force is neglected as this is applicable for sub-micron particle. It is important to have some understanding of the way in which particles behave upon impact with a solid wall in order to continue trajectory calculations after an impact event. Ideally, a simulation should be able to predict the correct rebound angle and velocity from the impact properties. The relationship between impact and rebound can be described in terms of restitution coefficients for a particular material. Restitution coefficients based on particle velocity ratio (V_2/V_1) give a measure of the momentum exchange on impact, and are therefore related to the energy available to damage the material surface by erosion.

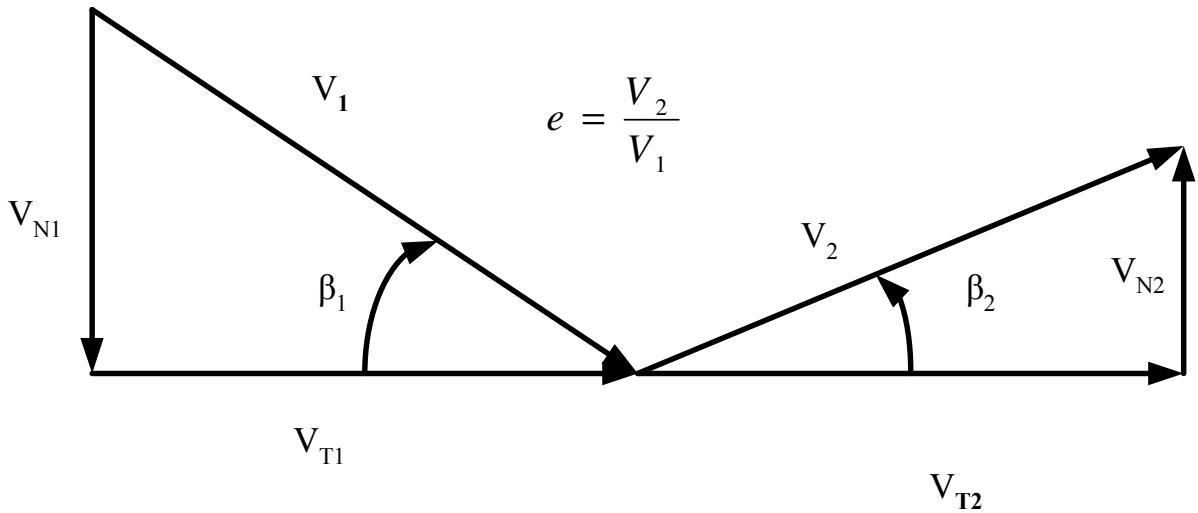

Figure 4.7: Impact and rebound notation for restitution coefficients.

Figure 4.7 presents the above-mentioned symbols. Clark and Burmeister (1992) made an analysis of particle-wall interaction in liquid flows based on squeeze film theory. The film of liquid trapped between a particle and the wall has a cushioning effect on the particle—the squeeze film effect. In order for a particle-wall collision to occur, the particle must have sufficient velocity to overcome the effect of the squeeze film. If the particle is to rebound after impact, it must again have sufficient residual kinetic energy to escape from the squeeze film region and escape into the main flow. If the particle have insufficient rebound energy it will remain trapped by the squeeze film effects. Equations have been developed which allow estimation of the squeeze film effect. This theory has been successfully applied in erosion modeling studies by McLaury et al. (1996).

Particle impingement data (impact velocity and angle of impact) are the most important for calculating erosion rate. Two different approaches are applied for Lagrangian particle tracking:

- Mean Velocity approach or Non-Stochastic Particle tracking.
- Stochastic approach.

In mean velocity approach, the particles are tracked on mean value of the velocity. The CFD code Fluent predicts the trajectory of a discrete-phase particle by integrating the force balance equation written in a Lagrangian reference frame [refer to equation 3-16]. In stochastic approach, the effect of turbulence is included using the instantaneous fluid velocity, u' . In the stochastic tracking approach, FLUENT predicts the turbulent dispersion of particles by integrating the trajectory equations for individual particles, using the instantaneous fluid velocity, $u + u'(t)$, along the particle path during the

integration. By computing the trajectory in this manner for a sufficient number of representative particles (termed as “number of tries"), the random effects of turbulence on the particle dispersion may be accounted for. In FLUENT, the Discrete Random Walk (DRW) model is used. In this model, the fluctuating velocity components are discrete piecewise constant functions of time. Their random value is kept constant over an interval of time given by the characteristic lifetime of the eddies.

When a sufficient number of tries is applied, the trajectories computed will include a statistical representation of the spread of the particle stream due to turbulence. When multiple stochastic tracking is applied, the momentum and mass defined for a certain injection, are divided evenly among the multiple particle/droplets and are thus spread out in terms of the inter phase momentum, mass, heat calculations. When doing calculations with stochastic option, it is found out that the stochastic option is providing the demonstrative results. But the problem is the huge difference between the stochastic and non-stochastic approach. This can be explained by observing the “particle tracking” option available in the FLUENT software. For various cases, it will be seen that the particle path lines are the determining factors in the erosion process for a desired surface. By employing stochastic approach, the particles are influenced by the fluctuating component of the fluid velocity.

This fluctuation is dragging the particles more towards the outer surface of the protruded pipe. As a result, number of impacts by particles is increased. Moreover, in some cases multiple impacts by particles are occurred to cause higher erosion. Some

cases will be discussed to demonstrate the difference between the stochastic and non-stochastic approaches.

In Figure 4.8, the total erosion rate variation with different particle diameters for certain geometry of depth 1mm, thickness 3mm at inlet velocity 10 m/s is shown. The stochastic values are almost 5-8 times higher than those of the non-stochastic values are. To investigate the reason behind this, particle pass lines are observed carefully for both stochastic and non-stochastic cases. Figures 4.9 to 4.10(A) & (B) demonstrate the reason behind this discrepancy in values. In Figure 4.9, the particle path lines for non-stochastic case are seen. The particle stream is shown to impact on the outer surface of the protruded pipe. In the present work, for non-stochastic cases, around 140 particles are tracked at a time. From the Figure 4.9 it is seen that the number of particles impacts at the outer surface of the protruded pipe is around 5-10. When stochastic option is chosen for the same case, the instantaneous velocity fluctuations are added to the mean velocity component in the particle motion equation. Sufficient number of particles is introduced to the flow to get a statistically representative pattern of the particle dispersion. In the Figures 4.10 (A) & (B), the stochastic particle tracks are seen. In the present work, for stochastic option, around 4200 particles are tracked at a time.

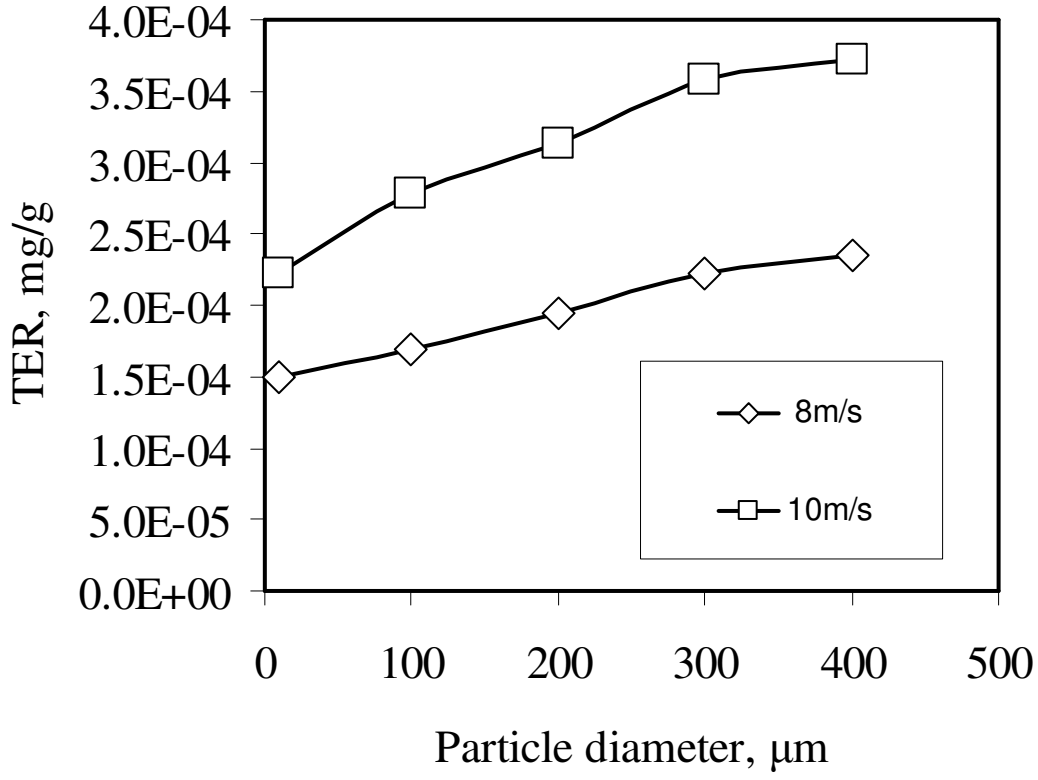

Figure 4.8: Total erosion rate variation with particle diameter, d_p, at different velocities, for the case H= 1mm, T=3mm.

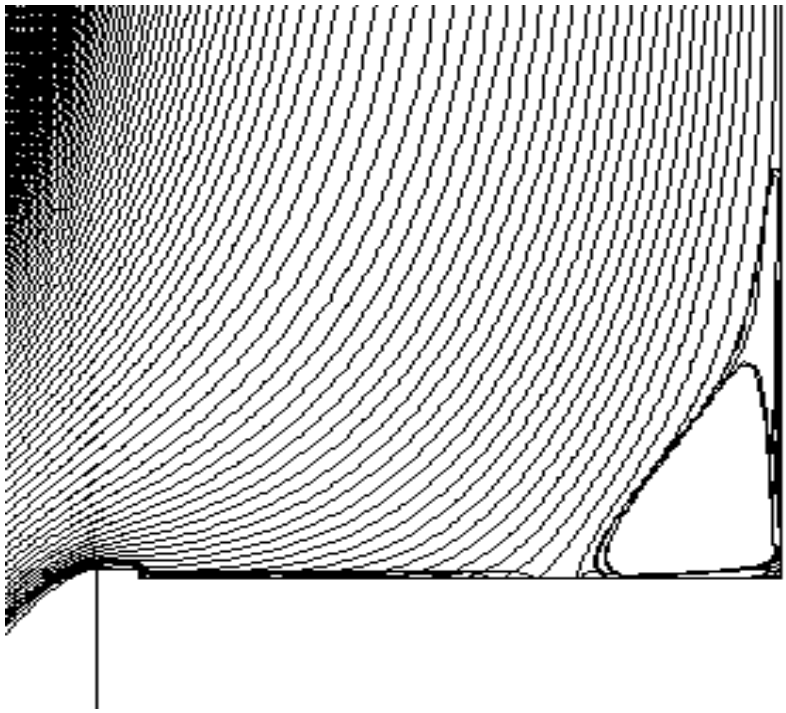

Figure 4.9: Particle path lines for the case, H= 1mm, T= 3mm, d_p= 400 μm, V= 10m/s (Non-Stochastic approach).

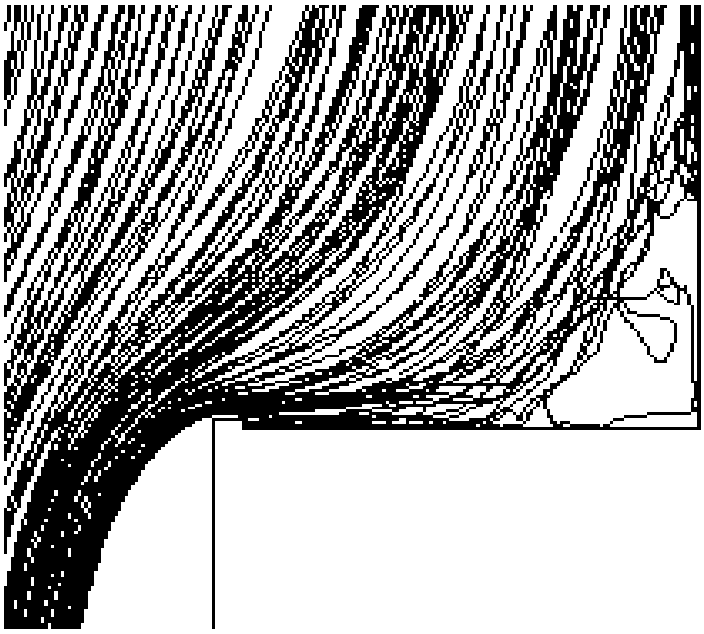

(A) Stochastic Approach

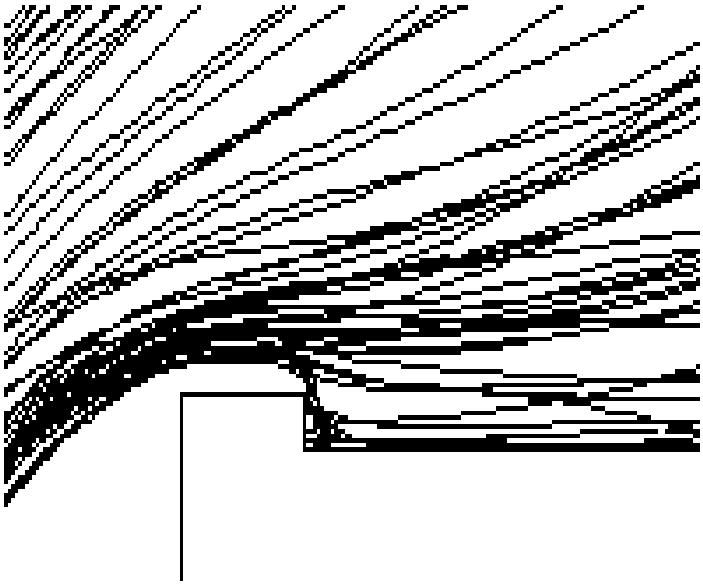

(B) Magnified view of the same

Figure 4.10: Particle path lines for the case H=1mm, T= 3mm, dp=400 μm, V=10m/s.

(A) Stochastic Approach (B) Magnified view of the same.

By close observation of the Figures 4.10 (A) & (B) reveals that the number of impacts in stochastic cases are many times higher than those in the non-stochastic cases. For stochastic cases, the turbulent velocity fluctuations are dragging the particles towards the outer surface of the protruded pipe and thereby making them impact there. Due to larger number of impacts for the same total mass of particles released at the inlet section; the total erosion rate values for stochastic cases are much higher than those for the non-stochastic. Taking another case with a different geometry, the same finding holds true. Figures 4.11(A) & (B) reveals a similar case for a different geometry of depth 4mm, thickness 3mm and for a flow condition of inlet velocity 10m/s, particle diameter 200µm. For stochastic options as shown in Figure 4.11 (B), higher numbers of particle impact at the outer surface of the protruded pipe, was causing higher erosion rates. In addition to that, multiple impacts on the outer surface also occurred by some particles. Close observation of Figure 4.11 (B) signifies this fact. This phenomenon contributed higher total erosion rate for all stochastic cases. While performing particle trajectories in the Lagrangian approach (for steady state case), the two important controlling parameters used in the FLUENT software have to be taken care of. They are :

- The length scale/step length factor.
- The maximum number of step determination.

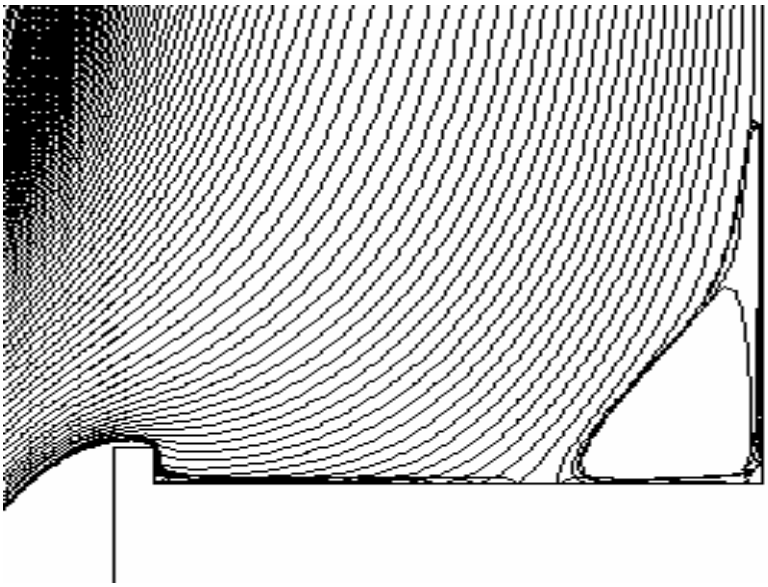

(A) Non-Stochastic Approach

(B) Stochastic Approach

Figure 4.11: Particle path lines for the case H= 4mm, T= 3mm, d_p= 200 μm, V=10m/s

(A) Non-Stochastic approach (B) Stochastic Approach.

The prediction of particle trajectory in FLUENT software is carried out through the computation of successive trajectories via integration of the particle motion equation (4.21). When the maximum number of steps is exceeded, FLUENT abandons the trajectory calculations for the certain particle injection and report the trajectory fate as "incomplete". The limit on the number of integration time steps eliminates the possibilities of a particle being caught in a recalculating region of the continuous flow and being tracked infinitely. The general rule of thumb of setting this parameter is to set that value which is equal to or greater than the multiplication value of maximum number of steps and Length Scale. It is approximately equal to the distance a particle has to travel. This parameter controls time step size used to integrate the equations of motion for the particle. The integration time step is calculated in FLUENT based on the specified length scale l, the velocity of the particle u_p and of the continuous phase u_c;

$$\Delta t = \frac{l}{u_p + u_c} \tag{4.22}$$

where l is the length scale and this is equivalent to the distance that the particle will travel before its equation of motion is solved again and updated. In the other approach, the step length factor controls the time step used to integrate the equation of motion. It differs from the Length scale in one point. It allows FLUENT to compute the time step in terms of the number of time steps required for a particle to traverse a computational cell. The integration time step is computed by FLUENT based on a characteristic time, which is related to an estimate of time required for the particle to traverse the current continuous phase control volume. This estimated transit time is defined as $\Delta t^* = \frac{\Delta t^*}{\lambda}$, where λ is the step length factor and is inversely proportional to the integration time step. It is roughly

equivalent to the number of time steps required to traverse the current continuous phase control volume. The default value for SLF is 5. In this work, not much difference is noted in results by using both the above mentioned two methods. To keep consistency in all the calculations, the Length Scale method is adopted for trajectory calculation.

The trajectories of the discrete phase injections are computed when graphics is applied for trajectory displayed (uncoupled approach) or when solution iterations are performed (coupled approach). In this present work, uncoupled approach is adopted. The following two steps show that approach:

1. Continuous phase solution.
2. Plotting and reporting of particle trajectories for discrete phase injections of interest.

4.7 Erosion Calculations

Particle impingement data is obtained by solving particle motion using the Lagrangian particle tracking method. Fluent 6.0 has the capability to produce this particle tracking type to demonstrate particle position, velocity, and particle identity. By setting "stochastic modeling" approach, the number of particles can be set in terms of "Ntries". Moreover, specific stochastic choice of approach can be adopted between the "random eddy life" and "cloud tracking method". In this work, random eddy life option is used. Thus particle impingement velocity is used to calculate impingement angle by using an external FORTRAN subroutine. Thereby the relevant particle impingement data (particle

velocity and impingement angle) is used in the relevant erosion model to get the local and total erosion rates along the desired surfaces.

4.8 The Overall Solution Procedure

The overall solution procedure applied in this work is outlined below:

1. Creating model geometry and meshing by using structured grid scheme. GAMBIT pre-processor is used in this purpose.
2. Starting appropriate solver (FLUENT 6.0)
3. Importing grid to the solver.
4. Checking entire grid and performing scaling to the appropriate unit.
5. Selecting solver formulation (Segregated in this work).
6. Choosing appropriate viscous models (k-ε RNG is used in this work).
7. Specifying appropriate materials(Water liquid in this work).
8. Specifying boundary conditions (at inlet, outlet, fluid, turbulence specification method. Intensity and length scale option is followed in this work).
9. Adjusting solution control parameters, i.e. under-relaxation parameters for pressure, density, body force, momentum (default values of 0.5 are used in this work) and upwind schemes (for better convergence first order scheme is applied up to a convergence criteria 10^{-3}. Thereafter second order scheme is applied for momentum and turbulence quantities up to a criterion 10^{-6}).
10. Initializing the flow field.

11. Performing calculations to get a solution (numerous iterations are performed to attain convergence).
12. Saving the results in case and data files.
13. Performing discrete phase calculation by adopting Lagrangian particle tracking techniques and choosing stochastic option to manifest the effect of turbulence.

    While incorporating the effect of fluctuating velocity components, an option known as "Ntries" is available in FLUENT. This option facilitates the introduction of adequate number of particles to be introduced in the flow field. Particle states (velocity, position, mass flow, temperature, diameter) are written in the "dpm" file format.
14. Editing the "dpm" files and converting the file into "text" format.
15. This edited "text" file, containing particle data is used in the FORTRAN code to evaluate particle impingement angle and thereby final calculations of erosion are performed at the desired surfaces.
16. Parametric studies are performed by varying different parameters like inlet velocity, particle diameter, protruded pipe depth and thickness, materials to observe their effect on erosion of the present study.

Chapter 5

Validation of Numerical Results

5.1 Introduction

The ideal way to validate the single-phase CFD predictions is to compare the predicted velocity fields with the actual velocity fields, measured by using Laser Doppler Velocimetry or similar techniques. It is a general approach to look for experimental data of a similar type of problem available in the literature. A CFD-based erosion-modeling tool is achieved by solving the fluid flow through the region of interest in the first step. Tracking of particles through the fluid and extracting impact data on all desired solid surfaces are the second step. Final step consists of relating the particle impact data (particle impact velocity and impingement angle) to erosive wear through a semi-empirical equation. A typical situation of the erosion process in a bend is presented in Figure 5.1, to get an understanding of the above mentioned erosion modeling steps:

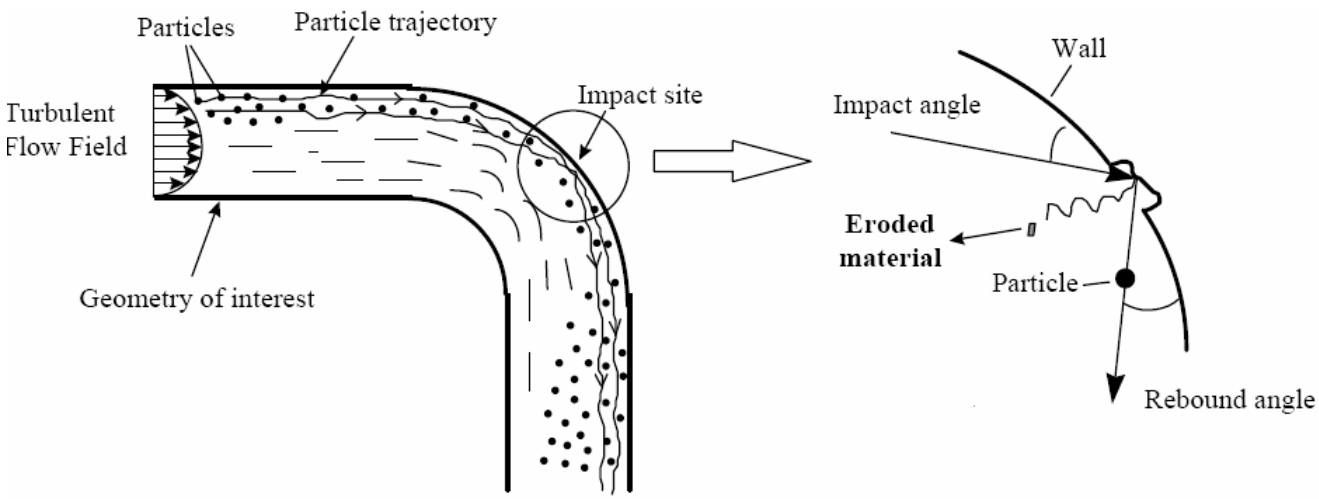

Figure 5.1: Schematic diagram of the erosion modeling concept.

For the validation purpose in the present work, the paper of Postlethwaite & Nesic (1993) is chosen. They reported erosion modeling with an experimental test section containing a sudden pipe contraction as its part. For validation purpose, this paper is mainly chosen due to the geometric similarity of their experimental test section with that of the present study. Moreover, the authors explained and reported their setup, experimental measurements, experimental procedure and data of their experiment in a detailed way.

For the present numerical work, the flow computations were performed by using the computational fluid dynamics package FLUENT 6.0, with Pentium processors having Microsoft Windows 2000. This specific package uses finite volume method for the discretization of the Navier Stokes equation. The k-ε turbulence model with RNG option was used to model the turbulence. In pre-processor GAMBIT, structured mesh scheme was used. Finer meshes were generated near the constricted region in order to demonstrate the effect of large velocity gradients at this region properly. Initially, the convergence of the continuous phase for all the flow variables were set at 10^{-3} by using the first order scheme for momentum and turbulence quantities. In order to get more precision in results, higher order convergence criteria of 10^{-6} is set for all the flow variables. Second order scheme for momentum and turbulence quantities was adopted at this higher order of convergence criteria in order to attain better results for a velocity-coupling scheme like SIMPLE. After the continuous phase was solved, Lagrangian particle tracking technique was applied to predict particle trajectories by taking into consideration the effect of stochastic turbulent dispersion. Uncoupled procedure for

particle tracking was applied, such that the particle phase does not interact with the continuous phase. After getting the impact data from Fluent software, a FORTRAN subroutine was employed to calculate the erosion rate. The following empirical model by Wallace and Peter (2000) was applied for that purpose.

$$\left.\begin{aligned} E &= \frac{(1/2)u_p^{\,2}\cos^2\alpha\sin 2\alpha}{\gamma} + \frac{(1/2)u_p^{\,2}\sin^2\alpha}{\sigma};\ \text{for } \alpha \le 45^0 \\ E &= \frac{(1/2)u^2{}_p\cos^2\alpha}{\gamma} + \frac{(1/2)u^2{}_p\sin^2\alpha}{\sigma};\ \ \text{for } \alpha > 45^0 \end{aligned}\right\}$$

where u_p and α are particle velocity and impact angle respectively. The cutting wear and deformation wear coefficients $\gamma \,\&\, \sigma$ have the values 33316.9 and 77419.7 for carbon steel, respectively. Shirazi et al. (1995)'s formula [ref. equation 3-25] was used to calculate and report the penetration rates in terms of millimeter of target material removed per year.

5.2 Brief Description of the Work Performed by Postlethwaite and Nesic (1993)

In their paper, Postlethwaite and Nesic (1993) reported experiments with a tubular flow cell of type 304 (UNS S30400) stainless steel. The tube cell carried dilute slurries of silica sand of diameter 0.43mm which acted as erodent. The geometric ratio of large bore pipe diameter to small bore pipe diameter was 2:1. In the present study, only the round

shaped silica sand particles were only considered. The details of the operating conditions of their experiment are presented in the Table 5.1. This table shows that there are several materials such as silica sand, large glass beads, and small glass beads that were used as eroding materials. The schematic diagram of the test section is presented in Figure 5.2. The segmented test cell contained a sudden constriction, a sudden expansion and a groove to produce distributed flow condition. For the present research purpose, the focus was to carefully review the erosion phenomena at the sudden constricted part only. Postlethwaite and Nesic (1993) showed that the most serious intensity of the erosion phenomena was a localized one & occurred under the distributed flow conditions.

Table 5.1 Operating conditions in the experiment by Postlethwaite and Nesic (1993)

Cell Material	Stainless steel	AISI TYPE 304
Pipe diameter	Large pipe Small pipe	42.1mm 21.2 mm
Slurry flow velocity	Large pipe Small pipe	3.3 m/s, Re=170000 13.3 m/s , Re=340000
Carrier fluid	Distilled water	Temperature=30^0
Particle average. diameter	Silica sand Large glass beads Small glass beads	0.43mm 0.4 mm 0.01mm
Particle concentration		2vol.%, 5vol.%, 10vol.%
Exposure Time		2h – 72 h

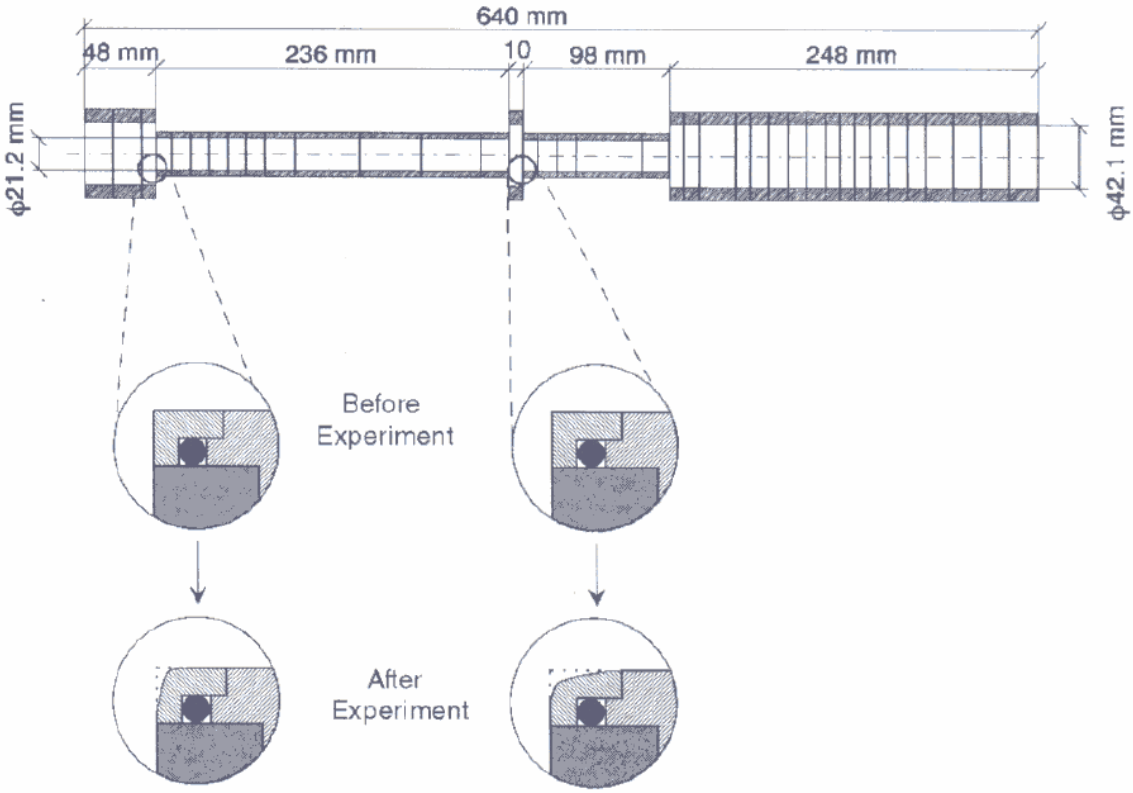

Figure 5.2: Schematic diagram of the experimental setup of Postlethwaite and Nesic (1993).

5.3 Validation of Present Work by that of Postlethwaite and Nesic (1993)

It was revealed experimentally that the slurry erosion (mm/y) initially increases with increasing particle concentration up to a certain particle concentration. After a certain limit of particle concentration increment, the rate of increase in penetration rate drops. This is due to the fact known as "particle-particle interaction" at higher particle concentrations. By increasing particle concentration from 2% volume to 5% volume, it was experimentally found that the erosion rate was increased by a factor of 2.5 times. By setting all the experimental parameters in the CFD code, the whole experiment was simulated numerically. Subsequently, penetration rate is calculated in terms of millimeter of target material removed in one year span of time. The predicted numerical result (for both stochastic and non-stochastic process), matched very closely with the experimental ones. In the numerical study, the increment in penetration rate was found to be around 2.3 times (stochastic case) by varying the sand concentration from 2%volume to 5% volume. By further increasing volume concentration from 5% to 10 %, the penetration rate increment was dropped. The authors reported around 20% increment in penetration rate for a change in sand concentration from 5 % volume to 10 % volume. For the same amount of increase in sand concentration, numerically it was found to be about 10% increment in penetration rate. In the Figure 5.3, it is noticed that the patterns of the curves are the same for both experimental and numerical studies. A logarithmic scale is applied to y-axis for penetration rate (mm/y). For stochastic particle tracking, the numerical data is more close to those of the experimental data. In their experimental work, Postlethwaite

and Nesic (1993) reported a change in test cell geometry with the passing of time. Experimentally it was found that the highest erosion rates occurred at the sudden constriction and at the downstream edge of the groove, 50 mm and 300 mm from the inlet section respectively. Actually large mean curvature occurred in these regions that led to higher erosion to occur. It was also found that in the constriction region where the diameter was 21.2 mm and fluid velocity 13.3 m/s, erosion rates were much higher. This was occurred due to the erosion phenomena. Severe erosion effect was observed at the bottom part of the contraction specifically. Due to the direct particle impingement, the lower part of the contraction plane was eroded and assumed the pattern of the erosion curve. The authors expressed the opinion that reshaping the geometry accordingly would result in lower erosion rates. They preferred rounding the edges that would lower the turbulence level and particle dispersion, and subsequently results in lower erosion rates. Figure 5.4 shows the photograph of the eroded constricted part used in the experiments of Postlethwaite and Nesic (1993). It is observed that the shape of the lower part of the constriction is altered. The sharp edge of the bottom tip of the contraction plane is turned into a rather rounded shape. This is due to the constant impact of the particle stream with higher magnitude of velocity and impingement angle. As a result, the sharp edge is eroded and the shape is turned to a round shape in place of the original sharp edge.

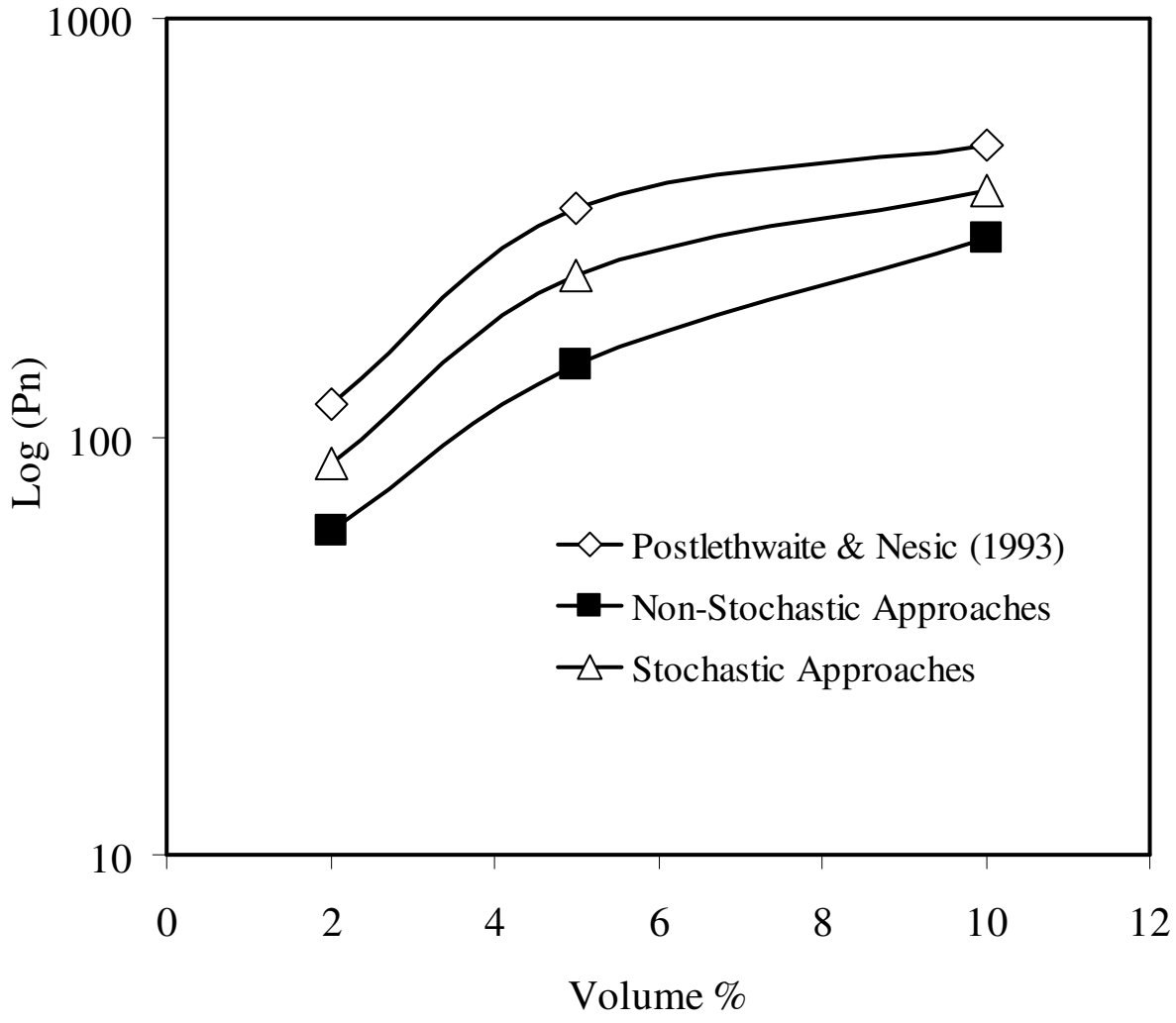

Figure 5.3: Validation of numerical results by the experimental data of Postlethwaite and Nesic (1993).

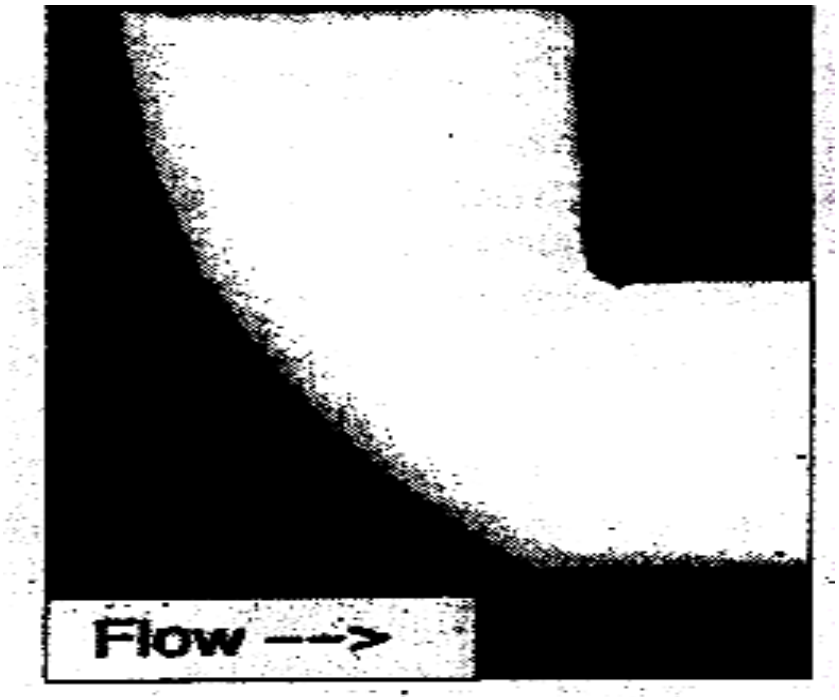

Figure 5.4: Photograph of the eroded contraction plane of an elbow (Ref. Postlethwaite and Nesic, 1993).

Chapter 6

Results & Discussions

6.1 Introduction

The present work deals with the prediction of erosion of a protruded pipe embedded in an axi-symmetric abrupt pipe contraction geometry. The flow is steady, 2-D axi-symmetric and is considered turbulent. The k-ε Turbulence model, with the Renormalized Group (RNG) option is used for turbulence modeling. Fully developed inlet flow profile is applied at inlet. Standard wall functions are applied as the wall boundary conditions. The fluid medium is water at 20^0C and the solid particles are of spherical shape with density 2668 kg/m^3. The volume percent of sand present in the mixture was 0.05%. The Reynolds number ranges from 9.95×10^4 to 1.99×10^6. Figure 6.1 shows a longitudinal section of the contraction region showing the protruded pipe. Different parameters are varied to investigate their influence on the erosion characteristics of the protruded pipe. The parameters include flow conditions such as inlet flow velocity, particle diameter as well as geometric variables such as protruded pipe depth, thickness and pipe material. Efforts were also made to determine threshold values for inlet flow velocity and optimum configuration for the depth of the protruded pipe. The range of each aforementioned parameter is presented in table 6.1. A typical configuration of all the relevant parameters is selected to conduct the parametric studies as shown in Table 6.2.

Table 6.1: Parameters investigated in the present work

Name of the Parameter	**Range of Values Considered**
Inlet Flow Velocity (m/s)	**0.5, 1.0, 3.0, 5.0, 8.0, 10.0**
Particle Diameter (μm)	**10, 100, 200, 300, 400**
Protruded Pipe Depth (mm)	**1, 2, 3, 4, 5**
Protruded Pipe Thickness (mm)	**1, 2, 3, 4, 5**
Pipe Material	**Carbon Steel, Aluminum**
Contraction Ratio, Cr = $\frac{r_2}{r_1}$	**0.25, 0.286, 0.33, 0.4, 0.5**

Table 6.2 Typical configurations of the geometric and flow variables

Particle Diameter, d_P	**200 μ m**
Inlet Velocity, V	**5m/s**
Protruded Pipe Depth, H	**5 mm**
Protruded Pipe Thickness, T	**3 mm**
Material	**Carbon steel**
Contraction ratio, Cr= $\frac{r_2}{r_1}$	**0.5**

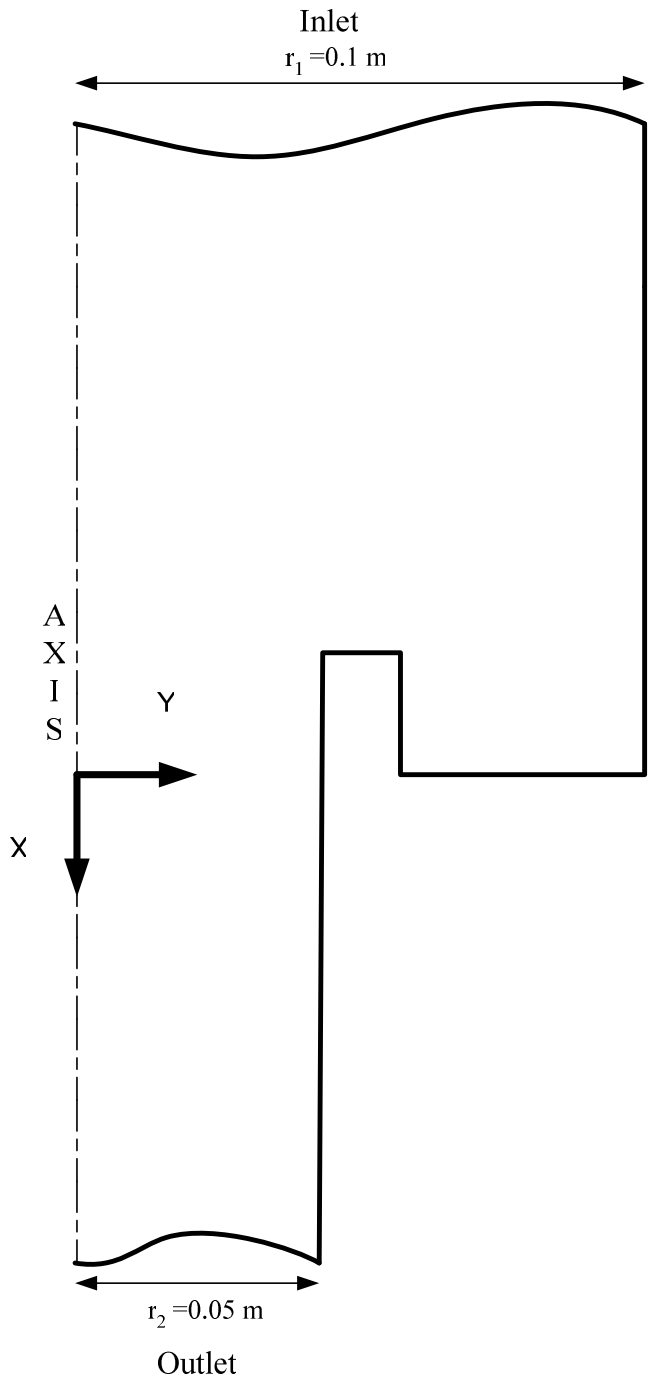

Figure 6.1: Schematic diagram of the overall geometry.

For the protruded pipe geometry shown in Figure 6.1, a certain nomenclature is adopted for the present study. These are protruded pipe depth, H, and thickness, T.

6.2 Features of the Flow Field near the Contraction Plane

The first part of erosion modeling for this problem is the solution of the continuous phase flow field. The flow is turbulent and k-ε model (RNG) is applied. The convergence criteria are fixed at the residual value of 10^{-6} for all flow variables. At inlet, fully developed profile of velocity is applied as shown in Figure 6.2. The works reported by Khezzar et al. (1988) indicated that the reattachment length is undesirably lengthened when a non-fully developed velocity profile is applied at the inlet. The inlet section of the pipe geometry is at a distance 3.5 meters upstream of the sudden contraction, which also justifies the fully developed velocity profile at inlet. The numerical calculations are based on 1st order upwind scheme for all variables in the momentum and turbulence kinetic energy equations. The discretization parameters are changed from 1st order to 2nd order upwind for a residual value greater than10^{-3}, in order to get more accurate results for the remaining flow field.

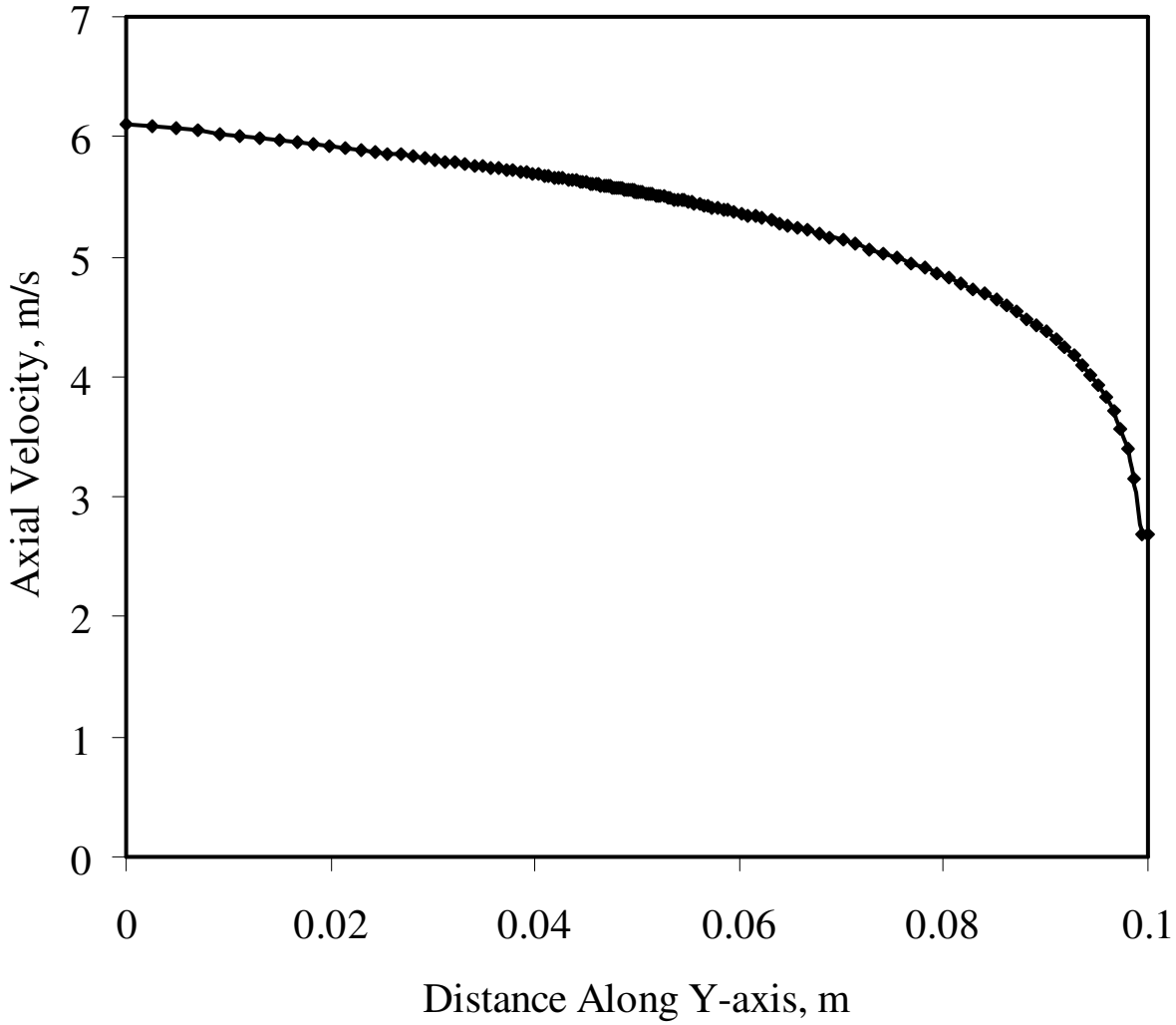

Figure 6.2: Schematic diagram of the inlet axial velocity profile.

6.2.1 Variation of the Developed Velocity Profile near Constriction

The variation of the velocity profile from its fully developed profile at inlet is investigated, as the flow approaches from inlet towards the contraction plane. The velocity profile is plotted at five selected locations as shown in (Figure 6.3). The axial velocity variation is shown in Figure 6.4. It is clear that the axial velocity remains almost the same as that of the inlet velocity, at sections X=-1m and X=-0.5m. The magnitude of the axial velocity remains very close to that at inlet (5m/s). Minute changes in shape and magnitude are observed when axial velocity profile is plotted at section X=-0.05m. The axial velocity is considerably increased to around 8m/s.The axial velocity profile shows significant change as it approaches further towards the protruded pipe in the contraction region (in this case at X=-0.01m). This is a manifestation of the presence of the protruded pipe as well as the contraction plane. The axial velocity magnitude jumps up to a value near 18 m/s at section X=-0.01m, which is at a very close proximity of the contraction plane. At a closer position (at X=-0.007m), profiles show higher velocity magnitude ($\approx$20 m/s). In addition to that, the shape of the velocity profile is very much distinct from that of the inlet velocity profile (Figure 6.4).

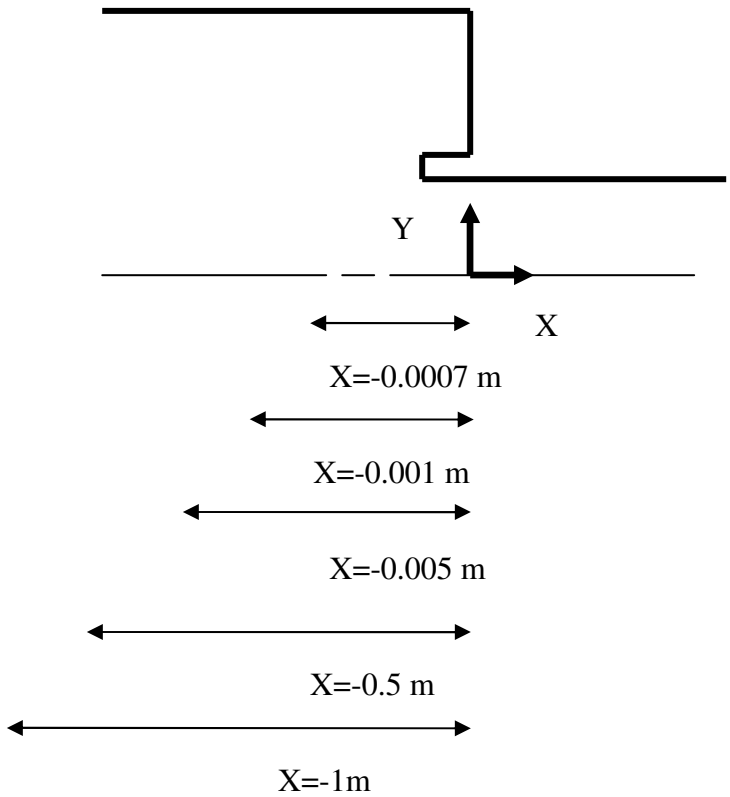

Figure 6.3: Schematic diagram of the different positions from the contraction plane along X-axis.

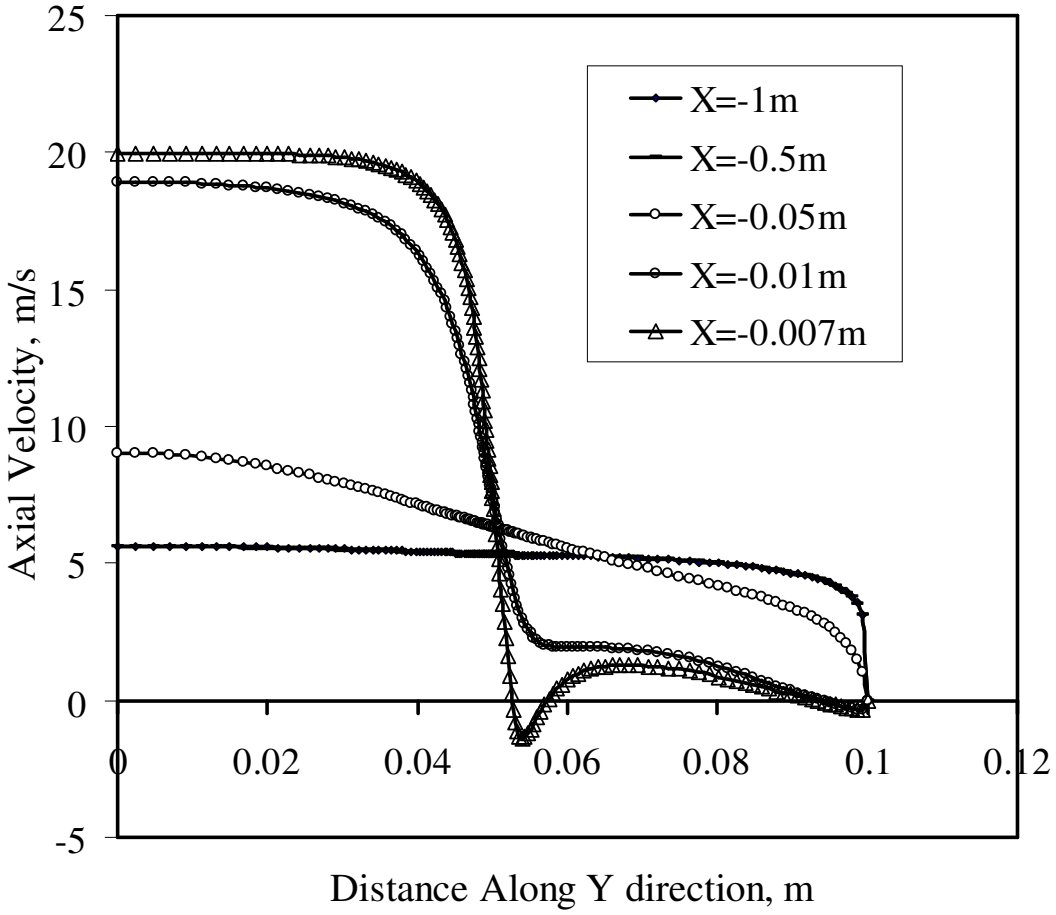

Figure 6.4: The axial velocity profiles at different axial distances from the contraction plane.

Radial velocity profile variations along the designated surfaces (Figure 6.5) are also investigated. It is observed in Figure 6.5 that the radial velocity profile variations are almost negligible at sections X=-1m, -0.5m and -0.05 m. The radial velocity component reaches values comparable to that of the axial velocity at sections X=-0.01m and -.007m. Large streamline curvature occurs upstream of the contraction plane, as the fluid approaches the inlet of the small Pipe. As a result, the increase in axial velocity (Figure 6.4) is counter balanced by the decrease in radial velocity (Figure 6.5) to guide the flow through the contraction plane.

6.2.2 Velocity Profiles along Three Surfaces of the Protruded Pipe

The details of the velocity field near the protruded pipe are of fundamental importance for understanding the erosion characteristics in that region. To identify the different surfaces of the protruded pipe; they are named as outer surface, face surface, inner surface. This nomenclature of the protruded pipe is shown in Figure 6.6. The velocity profiles along these three surfaces of the protruded pipe are shown in Figures 6.7, 6.8, 6.9.

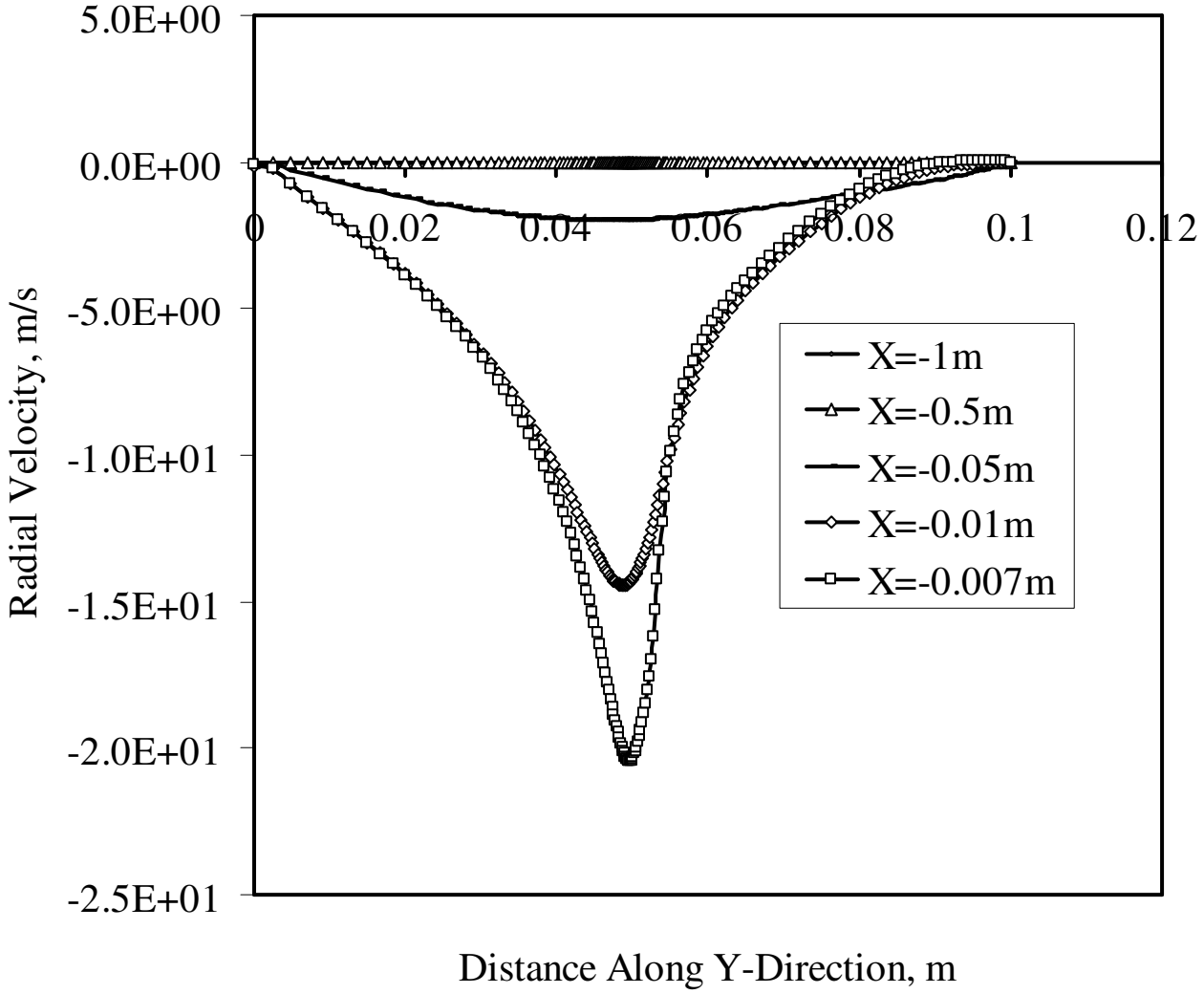

Figure 6.5: The radial velocity profiles at different axial distance from the constricted plane.

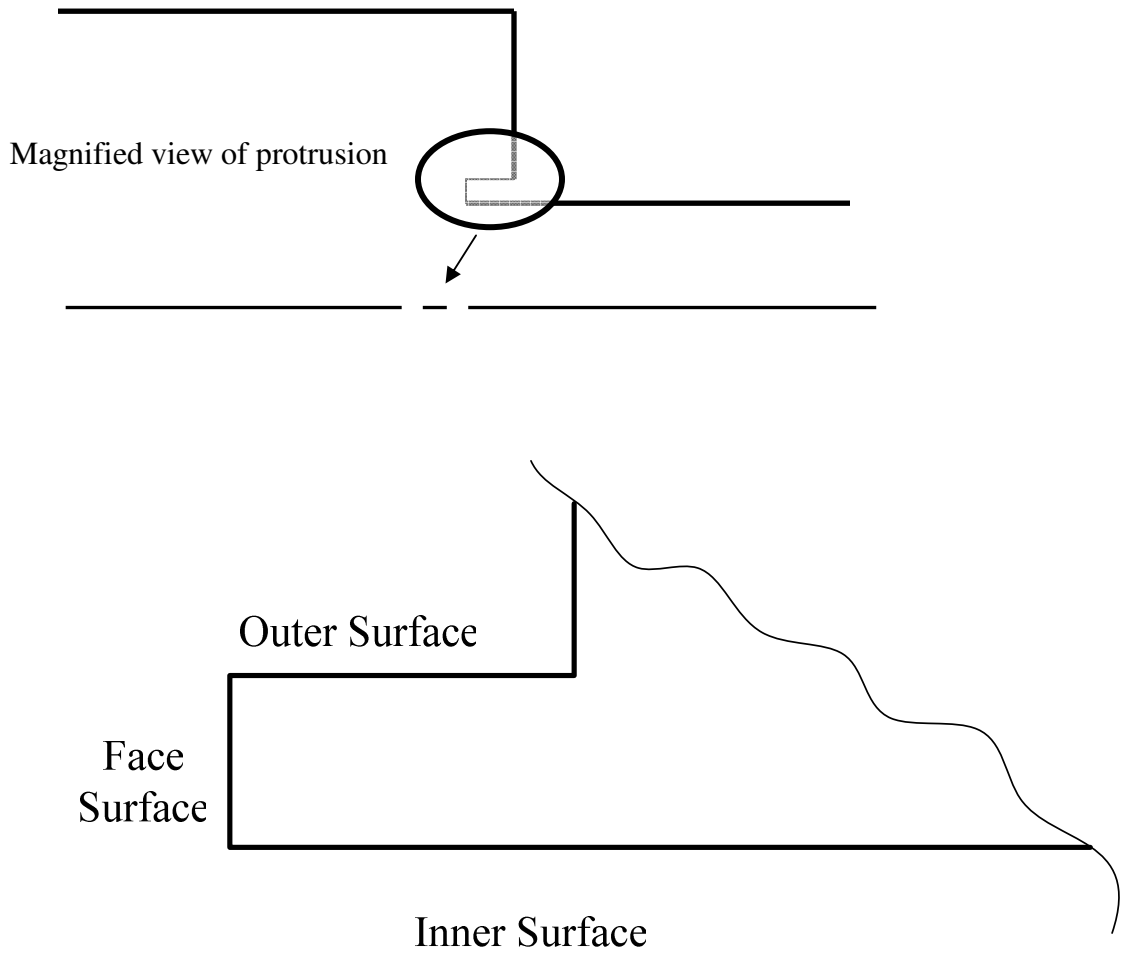

Figure 6.6: Magnified view of different surfaces of the protruded pipe.

In Figure 6.7, the axial velocity profile variation, along a horizontal line 2mm above the outer surface of the protruded pipe is shown. In the current analysis, the embedded protruded pipe outer radius is 0.053 m. Therefore, the designated line is located at Y=0.055m, as shown in Figure 6.7. Axial velocity remains unchanged from the inlet until the flow reaches at section X=-0.1m (Figure 6.7). As it approaches further closer the protruded pipe, the axial velocity reaches its highest peak. As a result, the shape of the profile is altered, now having a tip. After the protruded pipe, when the flow reaches the contraction plane, axial velocity magnitude decreases sharply to zero. In Figure 6.8, axial velocity component variation along a line 2mm below the inner surface of the protruded pipe is shown. It is observed that axial velocity remains unchanged from inlet to the neighborhood of the protruded pipe where severe fluctuations occur at inlet of the protruded pipe. As the fluid moves downstream, the axial velocity component again increases until reaching the fully developed flow region. Figure 6.9 shows the axial velocity component variation along a line X=-0.007mm. The axial velocity profile encounters a change in its shape, when it reaches near the protruded pipe at a radial distance between Y=0.05 m to Y=0.055 m. This velocity change is due to the presence of the protruded pipe. At a radial distance greater than Y=0.055 m, the axial velocity gradually decreases due to moving from high velocity region to lower velocity region.

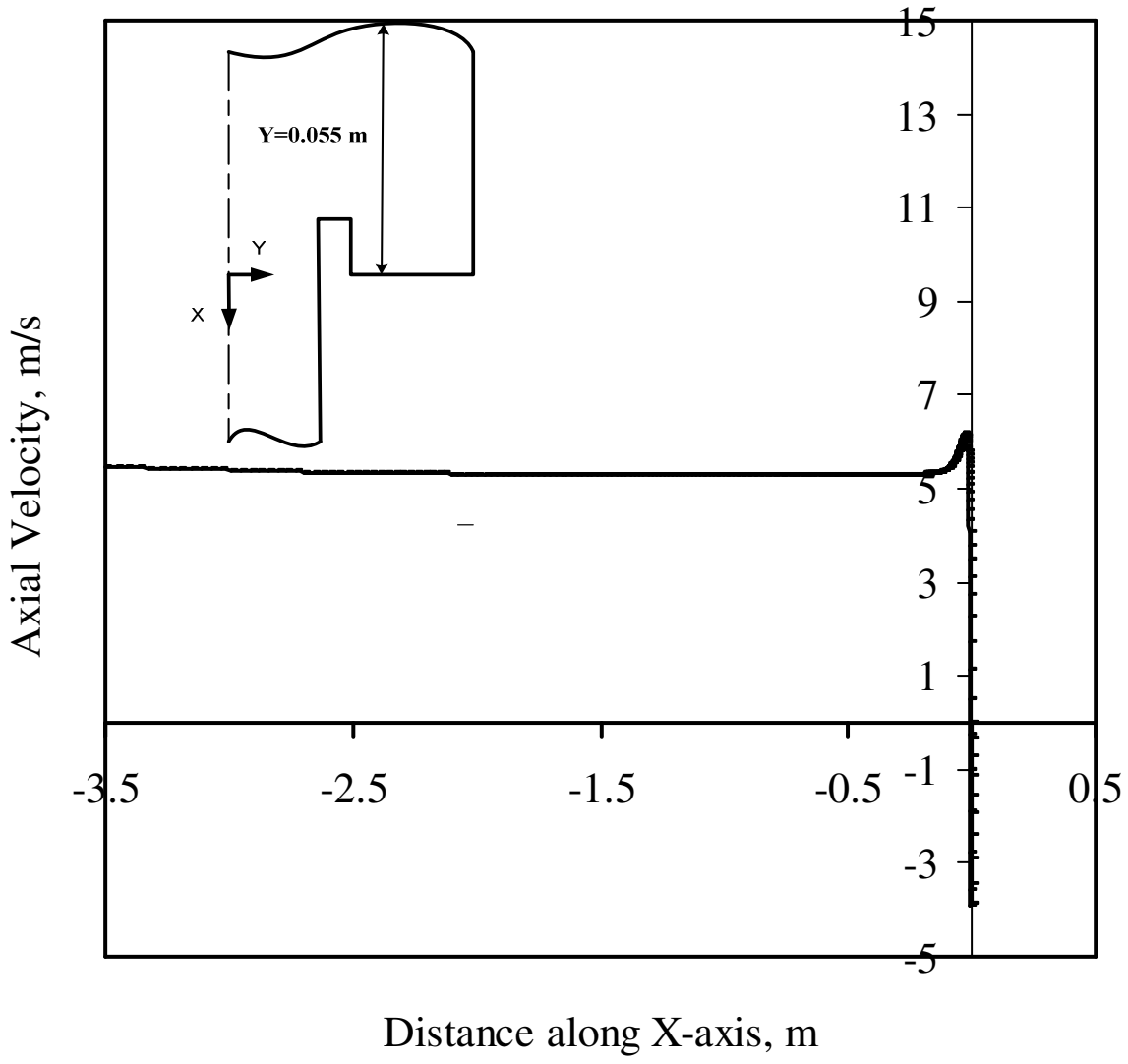

Figure 6.7: Velocity profiles near the outer surface of the protruded pipe along a line at Y= 0.055m.

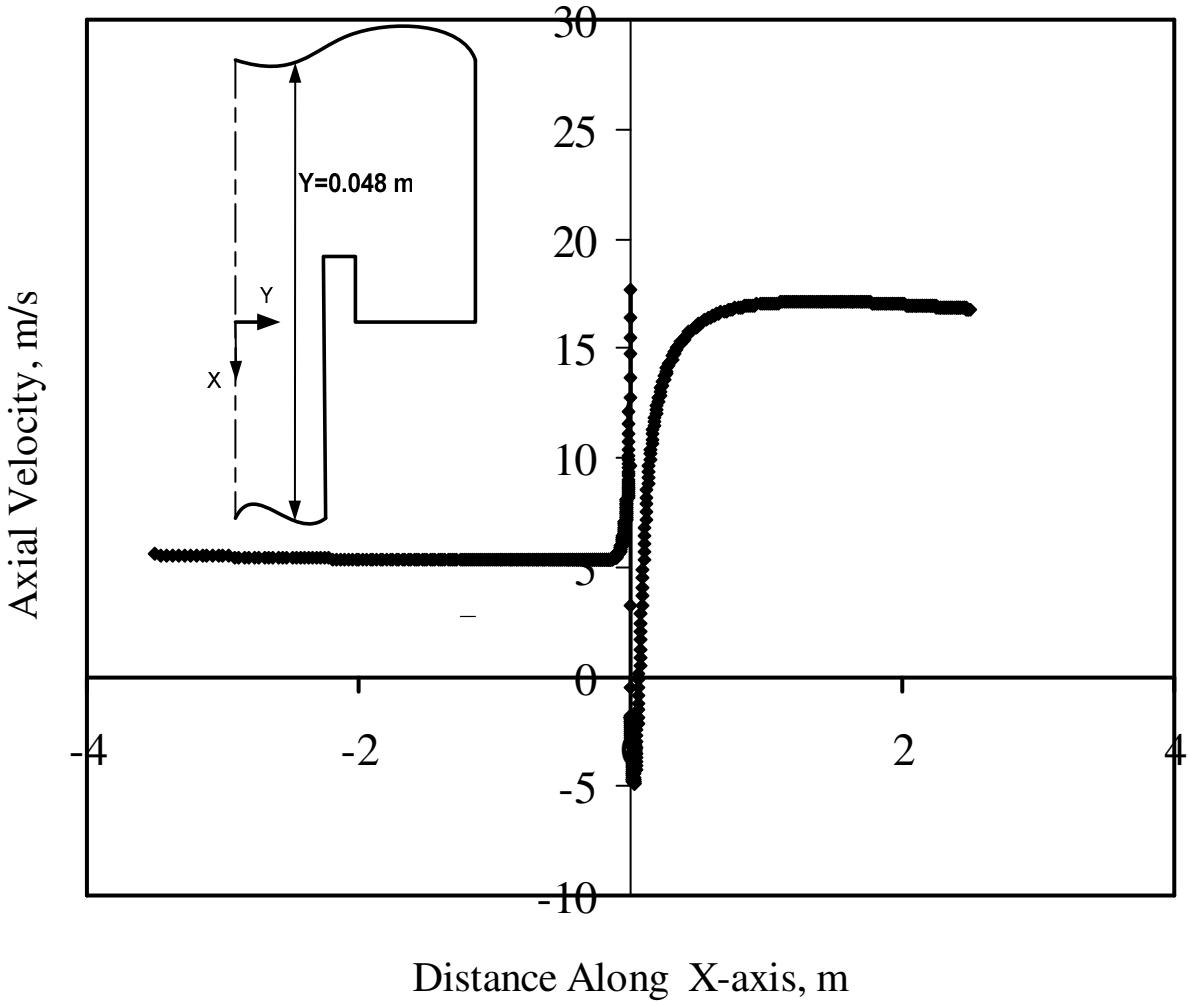

Figure 6.8: Velocity Profiles near the inner surface of the protruded pipe along a line at Y= 0.048m

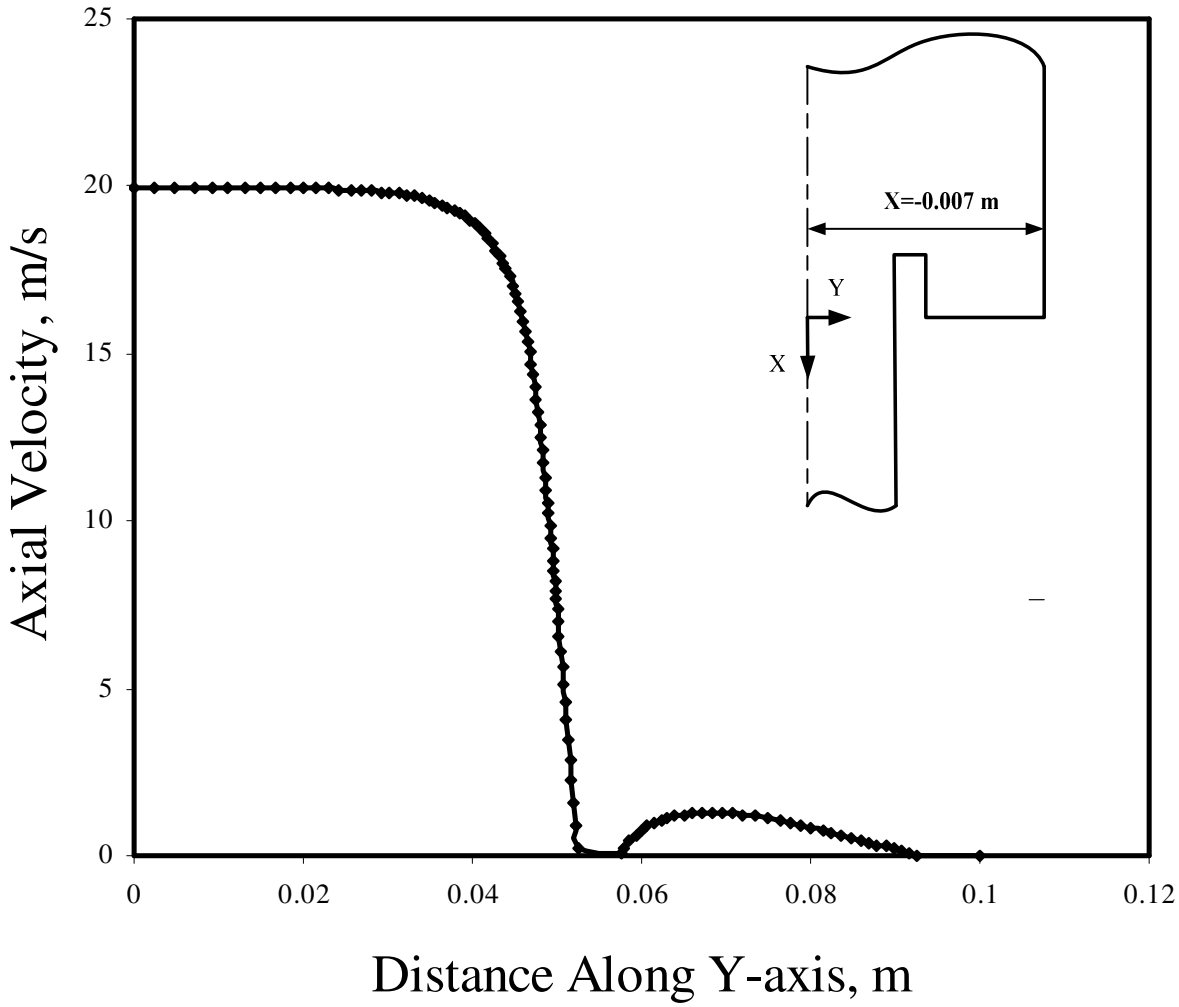

Figure 6.9: Velocity Profiles near the face surface of the protruded pipe along a line at X= -0.007m.

6.2.3 Pressure Variation

For further investigation of the flow field, pressure variation along the pipe centerline is presented in Figure 6.10. It is observed that upto the plane of contraction the static pressure remains almost constant. As the fluid approaches towards the small bore pipe, there is a decrease in the pressure. This phenomenon occurs as a result of velocity increase. It is a known that the greatest loss occurs downstream of the vena contracta where the flow boundaries expand from the vena contracta to the small bore pipe (Benedict et al., 1966). This is an uncontrolled expansion against an adverse pressure gradient. The smaller the area ratio, the larger the pressure gradients and hence greater the loss. The boundary between the mean flow and the recirculation region is highly unstable with energy being extracted from the mean flow to feed the large-scale turbulence generation within the recirculation region. The upstream recirculation region even though of much smaller extent compared to the downstream recirculation region; still needs to extract energy from the mean flow. It is the geometry of the inlet to the contraction which is responsible for the curvature of the streamlines and hence the extent of the contraction to the vena contracta.

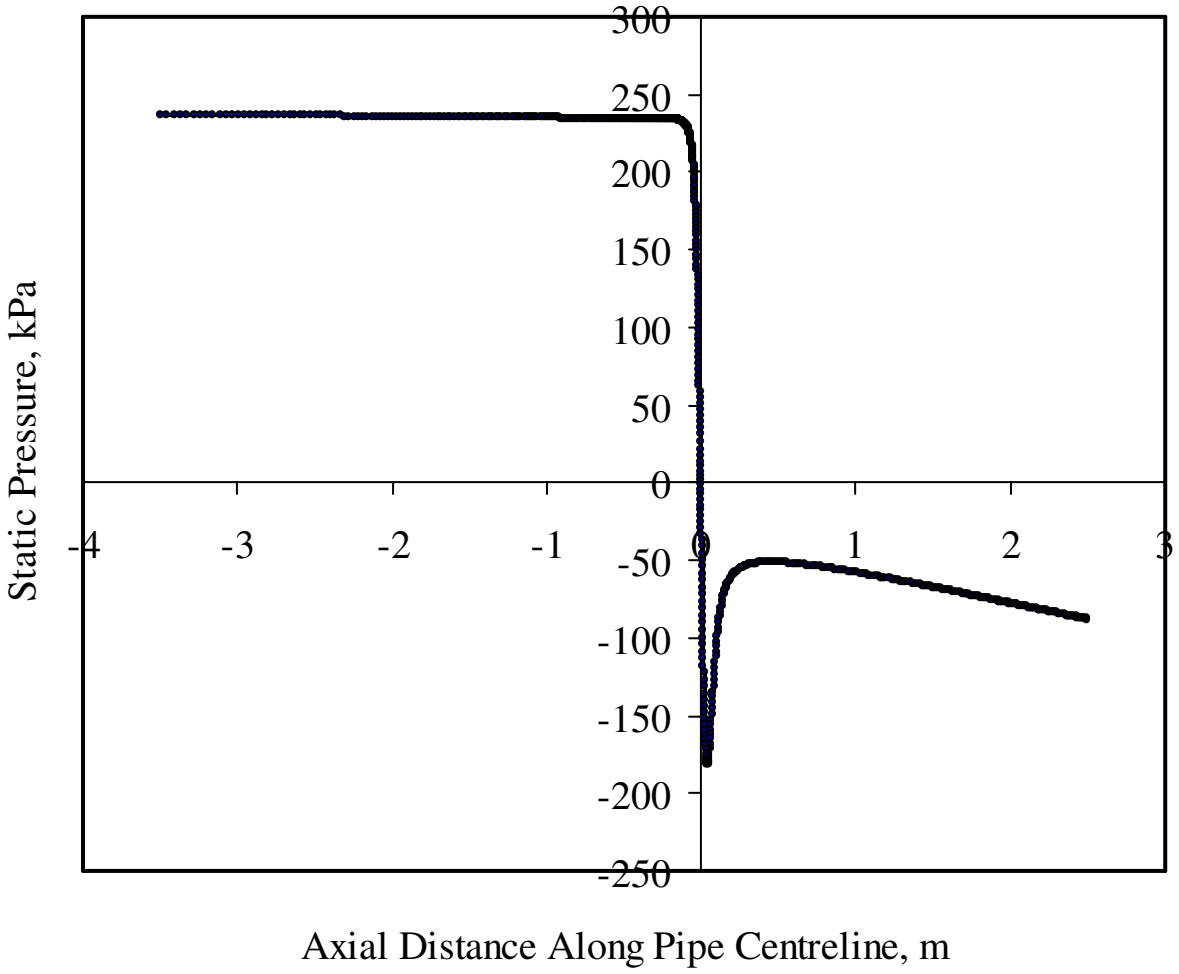

Figure 6.10: Static pressure variation along pipe centerline.

6.2.4 Influence of Flow Field over Particle Trajectories

As reported in the experimental work by Postlethwaite and Nesic (1993) for sudden contraction pipe geometry [Figure 5.2], the intensity of the particle impacts were localized at the lower part of the contraction plane [Figure 6.11(A)]. As a result, the sharp edge of the contraction plane is eroded and a new rounded surface is originated in that place [Figure 6.11(B)]. In the present work, a significantly different location of particle impacts is obtained. It is observed that particles are impacting the outer surface of the protruded pipe only. They are bypassing the face surface that was previously assumed as the impact location. The inner surface is also bypassed. From the physics of the problem, it is a known that the flow field has direct effect on the trajectories of the solid particles. The presence of the protruded pipe has imparted a direct effect on the flow pattern and subsequently on the particle trajectories. In this case, the protruded pipe might be acting as a “bluff” body to the approaching flow. As a result, particle path lines curves away from the face surface of the protruded pipe. To demonstrate this finding, Figures 6.12 and 6.13 are presented. Particle trajectories for the case of inlet flow velocity, V=10m/s, particle sizes of 200 μm and 400 μm respectively is shown. In both the cases, particle path lines are indicating the impact at the outer surface of the protruded pipe only.

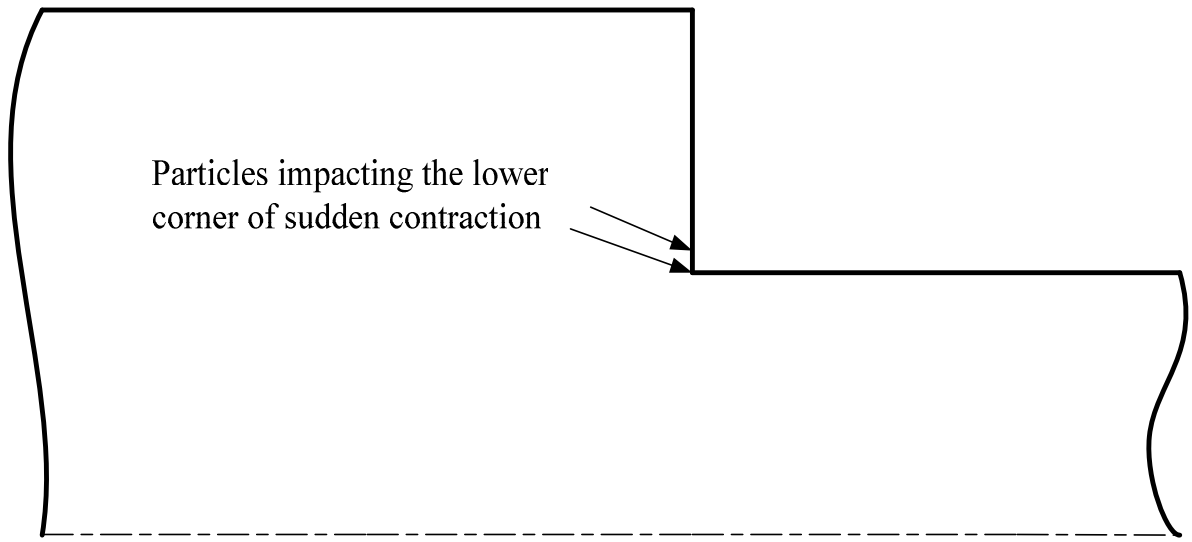

(A)

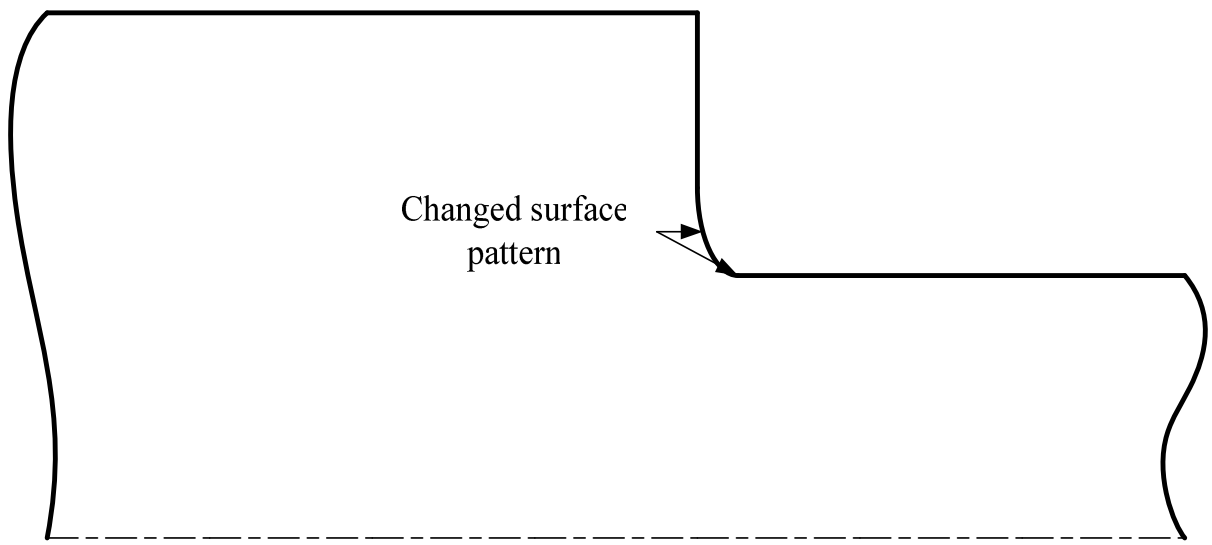

(B)

Figure 6.11: (A) Particles impacting the lower part of the contraction plane in the tube sheet (B) Change of contraction geometry due to erosion.

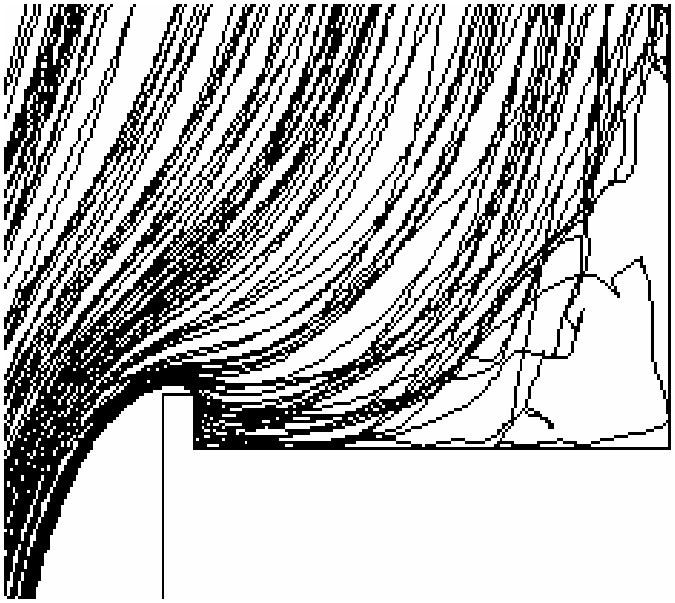

Figure 6.12: Path lines for particles of diameter 200 μm at inlet velocity 10m/s

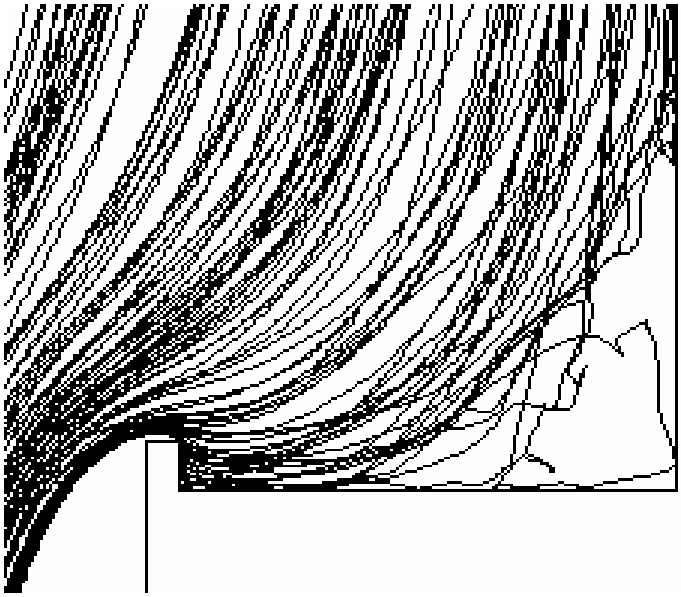

Figure 6.13: Path lines for particles of diameter 400 μm at inlet velocity 10m/s.

6. 3 Grid Independence Test

A grid independence test was carried out to make sure that the grid size does not affect the computational results. The solution domain was first divided into a large number of finite volumes. The equations are solved simultaneously using the solution procedure described by Patankar (1980). Fine grids were set in the areas where there are steep velocity gradients. Convergence is considered when the summation of the residuals of velocity components and pressure correction equations are less than 10^{-6}. Computations were carried out for three meshes having 61250, 64450 and 71250 control volumes. In the present work, local erosion rate variation for the three different meshes are calculated along the outer surface at different normalized position (L/H) from the inner to the outer tip of the protruded pipe depth. Figure 6.14 presents the results of the grid independence in terms of local erosion rate. It is observed that very negligible differences occurred in the values of local erosion rate in the different meshes. As a result, the finest mesh configuration of 71250 finite volumes is adopted for all subsequent calculations.

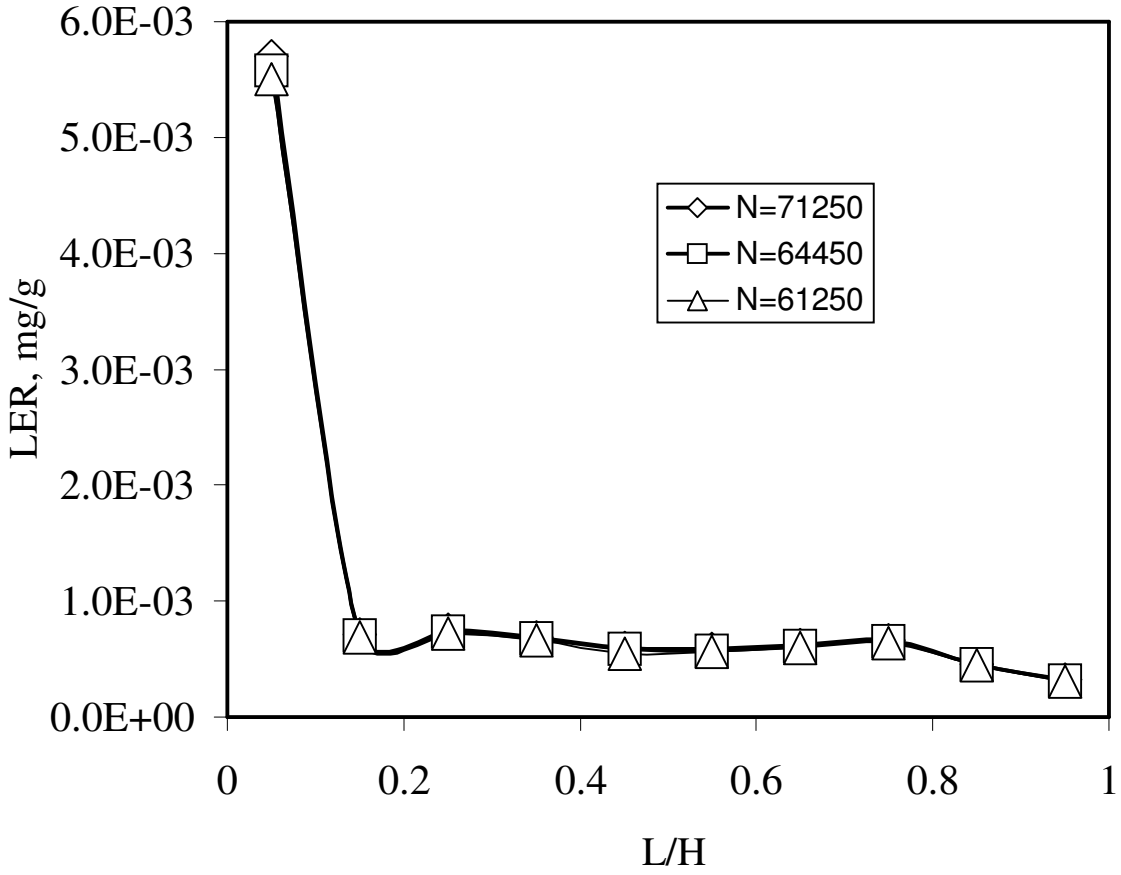

Figure 6.14: Grid independence test. Local erosion rate is presented along the outer surface and L is measured from the inner to the outer tip of protruded pipe depth (H).

6.4 Erosion Results

In the present work, different parametric studies were carried out to demonstrate the effect of different parameters on erosion rate of the protruded pipe. These parameters are inlet flow velocity, particle size, protruded pipe geometry, contraction ratio and pipe material. The subsequent sections contain the detailed results and analysis of the influence of each parameter on erosion and penetration rates of the protruded pipe.

6.5 Effect of Inlet Velocity on Erosion and Penetration Rates

In the present study, the inlet flow velocity is varied in the range from 0.5 m/s to 10 m/s. Thus, its influence is observed on the total erosion rate (mg/g) and penetration rate (mm/y). Effect of velocity variation is observed for the protruded pipe depth of 5mm, thickness of 3mm and the contraction ratio of 0.5. The solid particles of 200 μm diameter are selected as eroding material for the carbon steel pipe.

6.5.1 Effect of Inlet Velocity on Total Erosion Rate

The influence of inlet flow velocity on total erosion rate calculated in milligram of material removed per gram of solid particles (mg/g) is presented in Figure 6.15. It is observed that the inlet flow velocity has a very strong influence on the total erosion rate of the protruded pipe. The total erosion rate increases exponentially with the increase of

inlet flow velocity. This trend holds true for both the non-stochastic and stochastic approaches. It is noteworthy to mention that the total erosion rate values are insignificant for inlet flow velocity less than 3m/s. The total erosion rate curve follows an exponential pattern for inlet flow velocity values greater than 3m/s. A comparative study is presented here to support the above assertion. In non-stochastic cases, the total erosion rate is increased about 163% when the velocity is increased from 5m/s to 8 m/s. In the stochastic case, 262 % increase in total erosion rate resulted for the same velocity increment. Increasing the inlet flow velocity from 8m/s to 10 m/s, resulted total erosion rate increase of 167% for stochastic and 95% for non-stochastic cases respectively. Upon investigating these, the inlet flow velocity 3m/s can be considered as "threshold velocity" for significant erosion to take place. Inlet flow velocity greater than 8 m/s can be considered "alarming/hazardous limit" for the protruded pipe. Solid particle trajectories are performed to investigate the above phenomenon. Figures 6.16 (a-b) shows solid particle trajectories for an inlet flow velocity of 5m/s with particle diameter 200 μm. Figures 6.17 (a-b) shows the corresponding particle trajectories when flow velocity is 8 m/s. By close investigation of the magnified views of the particle trajectories at Figures 6.16 (b) and 6.17 (b), it is seen that the number of particles impacting the outer protrusion surface is more for the case of higher flow velocity of 8m/s. From that viewpoint, the erosion is higher for higher flow velocity value.

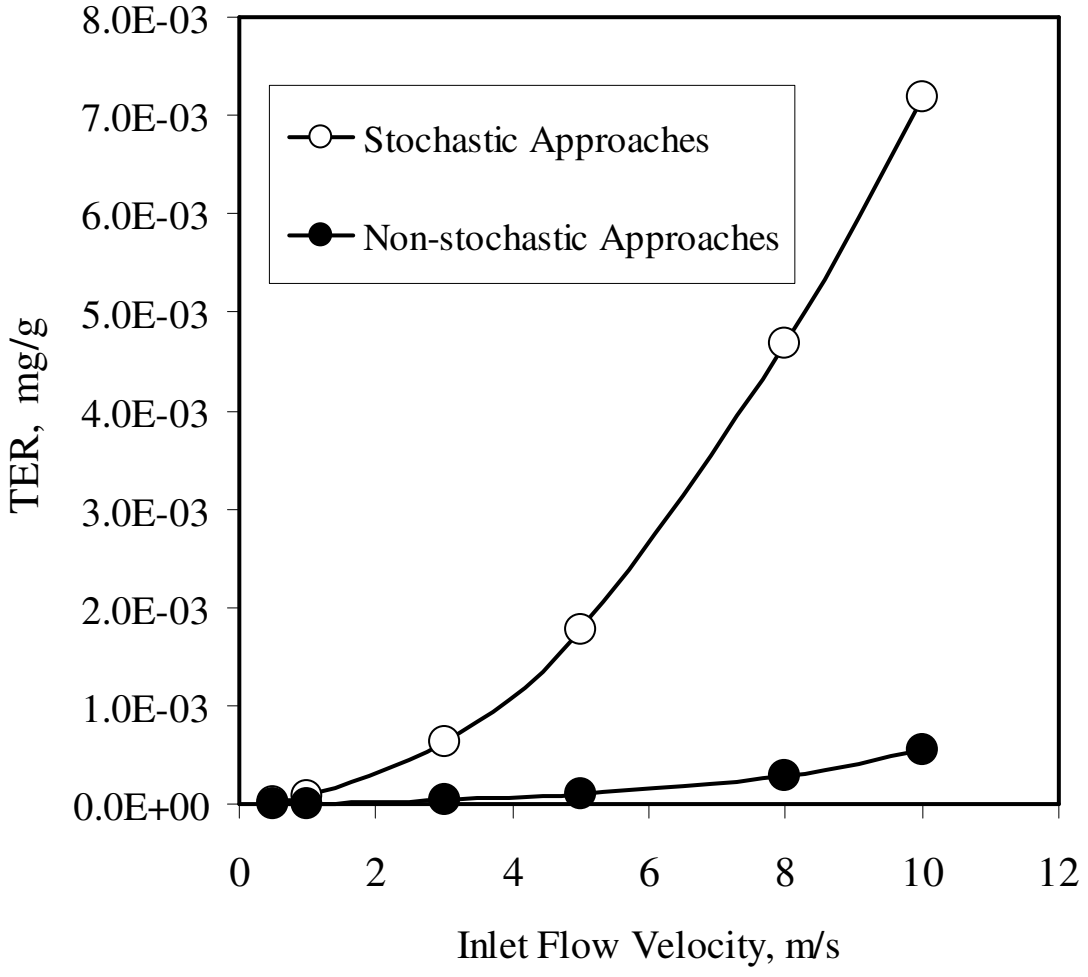

Figure 6.15: Effect of inlet flow velocity on the total erosion rate for stochastic and non-stochastic approaches, for the case of H= 5mm, T= 3mm, d_p =200 μm.

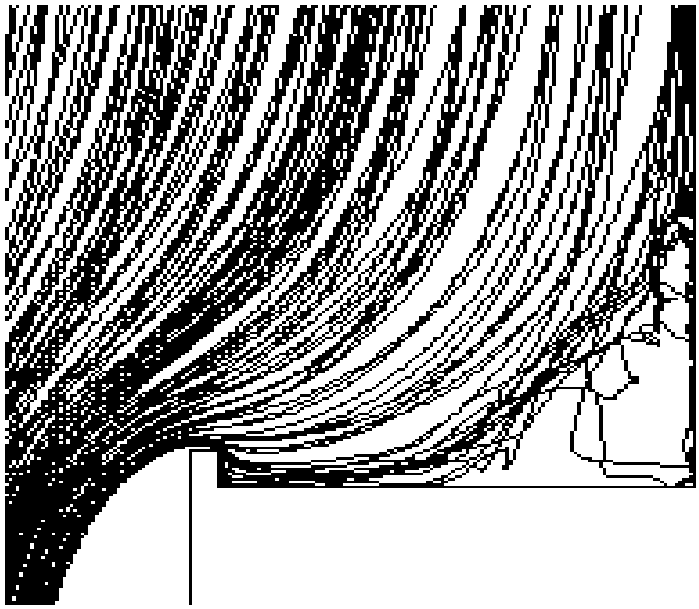

Figure 6.16 (a): Stochastic Particle trajectories for the case, V= 5 m/s, H= 5mm, T= 3mm.

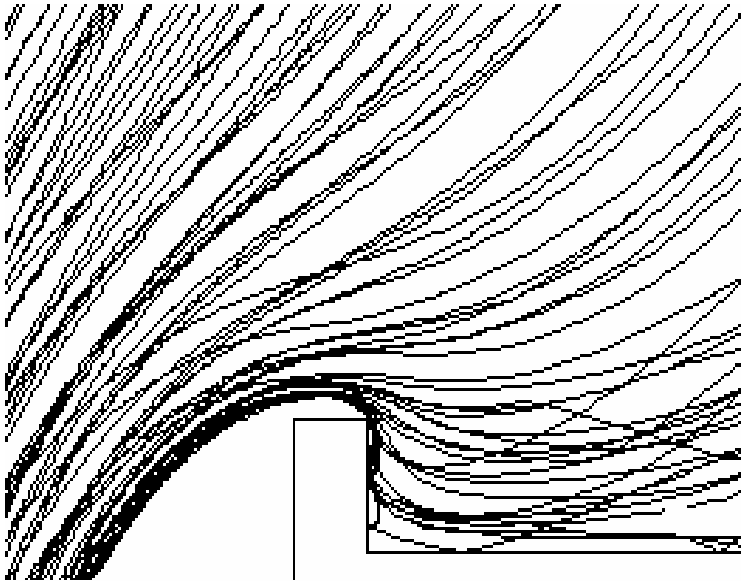

Figure 6.16 (b): Magnified view of the stochastic particle trajectories in the immediate neighborhood of the pipe protrusion for the same case as Figure 6.16(a).

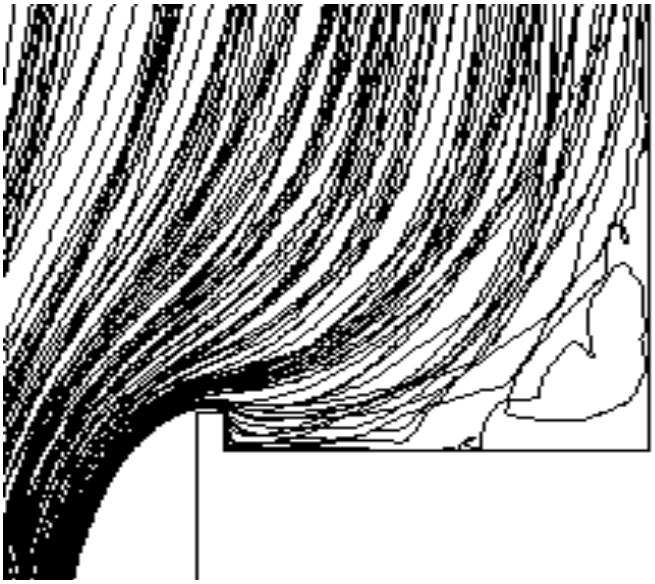

Figure 6.17 (a): Stochastic Particle tracking for the case, V= 8 m/s, H=5mm, T=3mm.

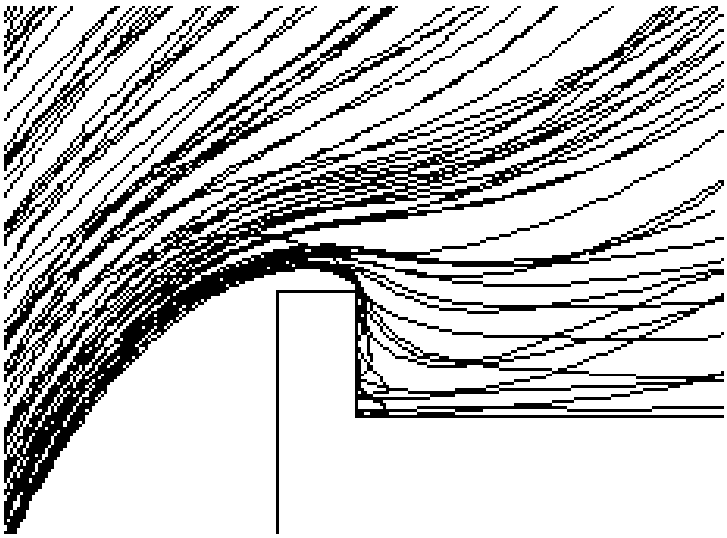

Figure 6.17 (b): Magnified view of the particle trajectories in the immediate neighborhood of the pipe protrusion for the same case as Figure 6.17 (a).

6.5.2 Effect of Inlet Velocity on Penetration Rate

The effect of inlet velocity on the penetration rate is investigated for a pipe protrusion of depth 5mm, thickness 3mm, considering 200 μm particle diameters. The penetration rate is calculated using the following equation proposed by Shirazi *et al.* (1995):

$$Pn = \frac{\dot{s}}{\rho_m A N_p} E_{lc} x 31536000$$

where $\dot{s}$ denotes sand rate (kg/s), E_{lc} is the local erosion rate (mg/g), ρ_m is the density of target material, N_p is the number of particles throughput and A is the impingement area. Figure 6.18 shows the penetration rate based on stochastic calculations versus the inlet flow velocity. It is observed that penetration rates are negligibly small for velocity value less than 3m/s. Further increase of velocity caused exponential increase in penetration rate. For example, increasing the flow velocity from 3 m/s to 5 m/s resulted in about five times increase in the penetration rate. Increasing the flow velocity from 5m/s to 8 m/s caused 4.25 times increase in penetration rate. Moreover, it is observed that the penetration rate curve resembles the same trend as that of the total erosion curve. It can be concluded that inlet flow velocity has a very prominent influence on the erosion rates of the protruded pipe.

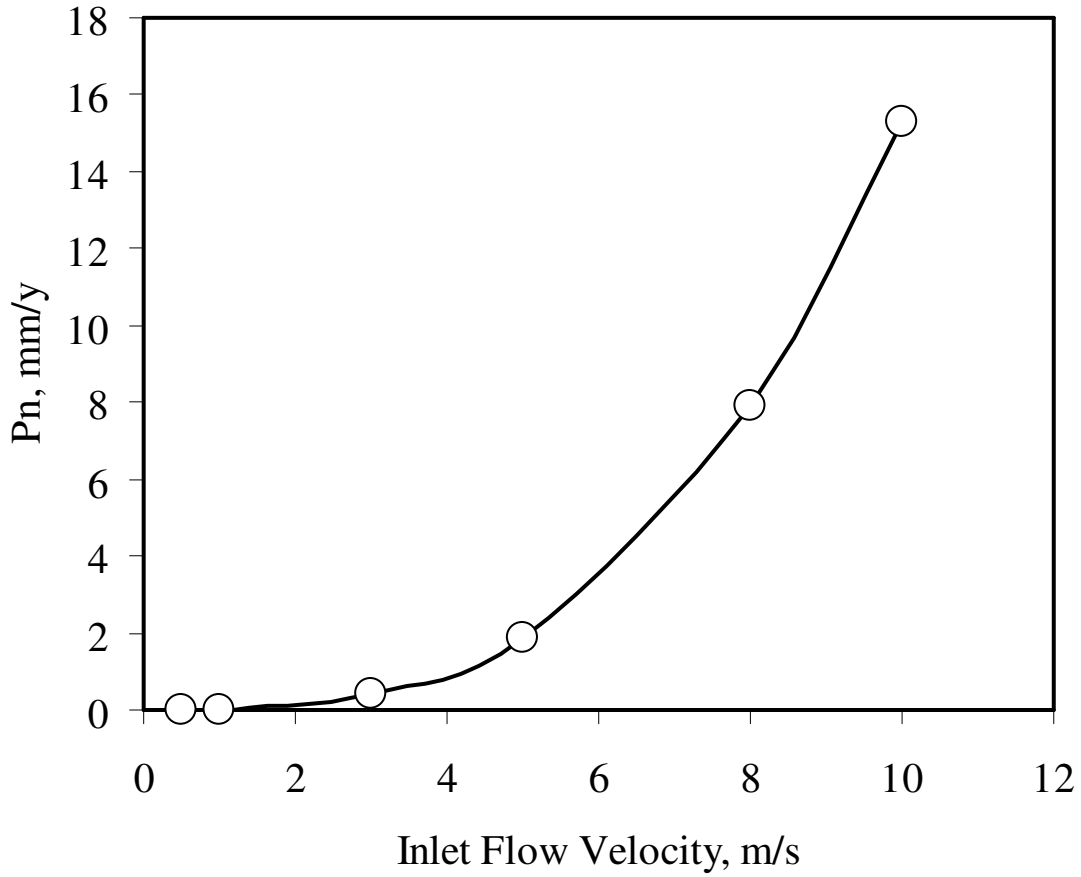

Figure 6.18: Effect of inlet flow velocity on penetration rate for the case, H= 5mm, T= 3mm, d_p =200 μm.

6.6 Effect of Particle Diameter on Erosion and penetration rates

The effect of particle diameter on both erosion and penetration rates was investigated, considering the typical flow velocity of 5m/s, protruded pipe depth 5mm, thickness 3mm. Figures 6.19 and 6.20 show the variations of total erosion rate and penetration rate with particle size respectively.

6.6.1 Effect of Particle Diameter on Total Erosion Rate

Figure 6.19 shows continuous increase in total erosion rate with particle size. This trend is proven to be the same for both stochastic and non-stochastic approaches. For example, total erosion rate in stochastic cases increases around 1.15 for particle diameter increment from 0 μm to 400 μm.

6.6.2 Effect of Particle Diameter on Penetration Rate

Similar type of trend is obtained for the penetration rate. From Figure 6.20, it is clearly seen that penetration rate increases continuously with the increase in particle diameter. An increase in particle diameter from 10 μm to 400 μm yields about 16% increase in penetration rate.

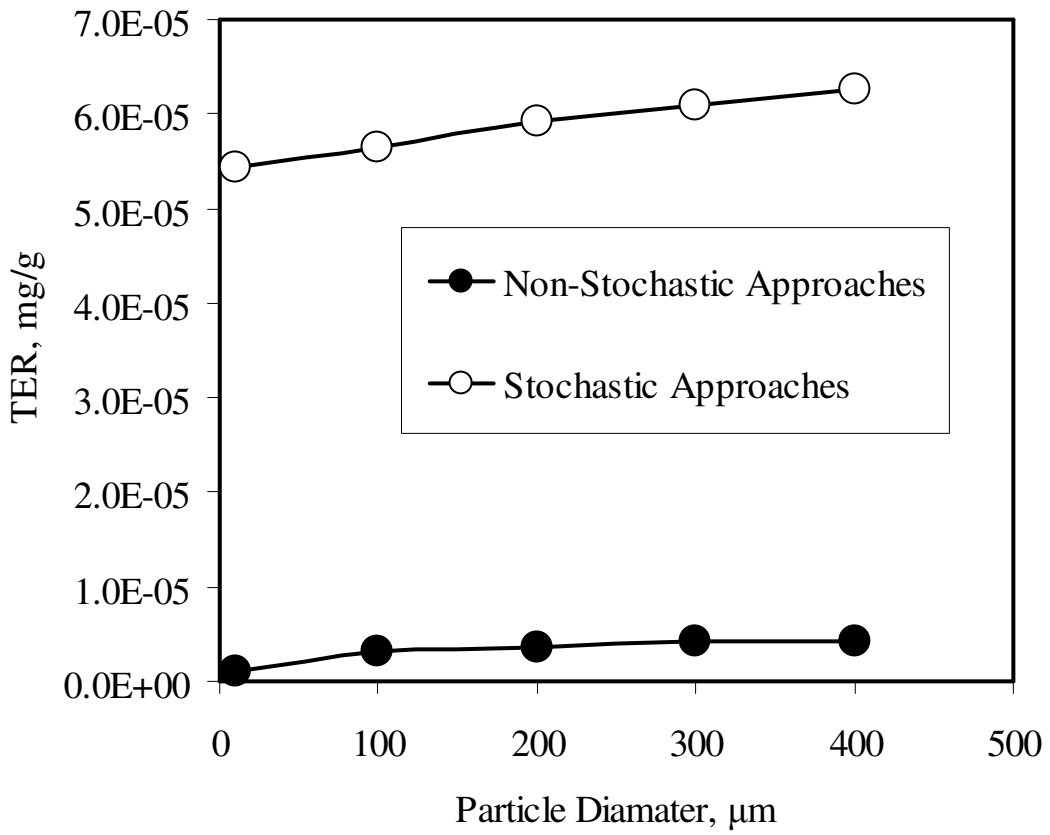

Figure 6.19: Influence of particle diameter on total erosion rate, for the case H=5mm, T= 3mm, V= 5m/s.

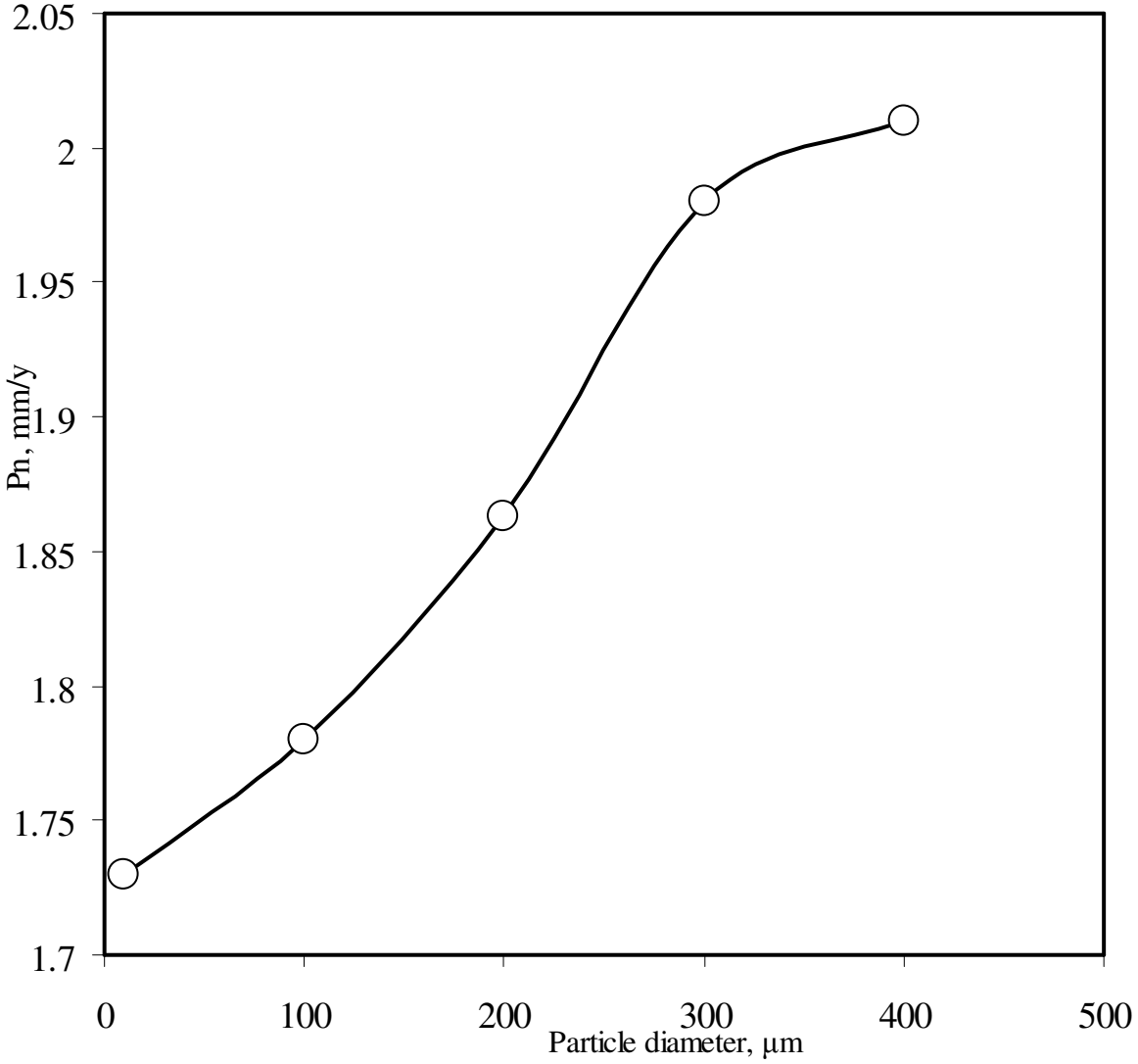

Figure 6.20: Influence of particle diameter on penetration rate, for the case,

H= 5mm, T=3mm, V= 5m/s.

Explanation of the effect of particle diameter is not that much simple like that of the inlet flow velocity. Several factors are involved in the analysis of particle diameter influence on total erosion rate. It is well known that the erosion rate depends on the particle size as well as number of impacts. Interesting thing to note that for the same total mass of particle released at inlet section, the number of large size particle (400 μm) is much less than that for the small size particles (10 μm). Nevertheless, mass removed from the protruded pipe depends on impact velocity and angle as well. From that viewpoint, the mass removed from the protruded pipe is more for larger particles, which is demonstrated in the higher total erosion rate for larger particle diameter. In addition, larger particles have more inertia that can deviate the particle trajectories considerably from the fluid streamlines. As a result, there will be a difference in the location of surface impacts as well as particle velocity (magnitude and direction) immediately before each impacts.

6.7 Effect of Protruded Pipe Geometry on Erosion and Penetration Rates

In the present work, two geometric parameters of the protruded pipe depth and thickness (Figure 6.1) are varied to observe their effect on erosion. A range of values from 1mm to 5mm is selected for both protruded pipe depth and thickness, to demonstrate their influence on total erosion rate and penetration rate.

6.7.1 Effect of Protruded Pipe Depth on Erosion Rates

The influence of the protruded pipe depth on the total erosion rate is presented in Figure 6.21. For an inlet flow velocity of 5m/s and particles of diameter 200 μm, the total erosion rate decreases with the increase in protruded depth. This pattern is consistent for both non-stochastic and stochastic approaches. To investigate the reason of such phenomenon, particle trajectories are examined. Figures 6.22-6.25 shows stochastic particle trajectories for depth 1mm, 2mm, 3mm, and 4mm respectively. By carefully reviewing the magnified views of Figures 6.22 (b), 6.23 (b), 6.24 (b), 6.25 (b), it is observed that the curvature of the particle path lines gradually increases with increasing depth. The larger the angle of impact, the higher the erosion rate. For a depth of 1mm (as in Figure 6.22), particles impact the outer surface at larger impact angles (close to 90°) in comparison with the impact angles for the case of 2mm depth (Figure 6.23).The same trend is continued as the depth is increased. For all these cases, variation in impact angle contributes to the variation in total erosion rate.

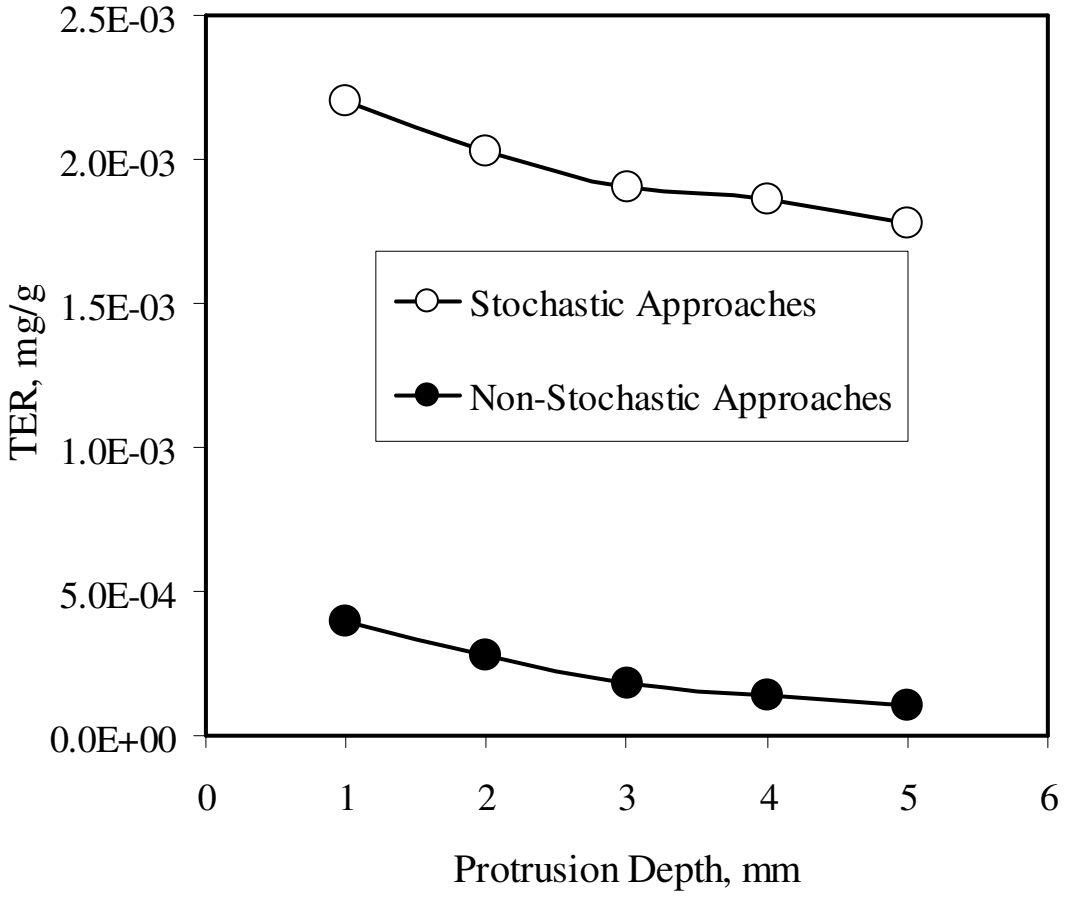

Figure 6.21: Influence of protruded pipe depth on total erosion rate, for the case of T=3mm, V= 5m/s, d_p= 200 μm.

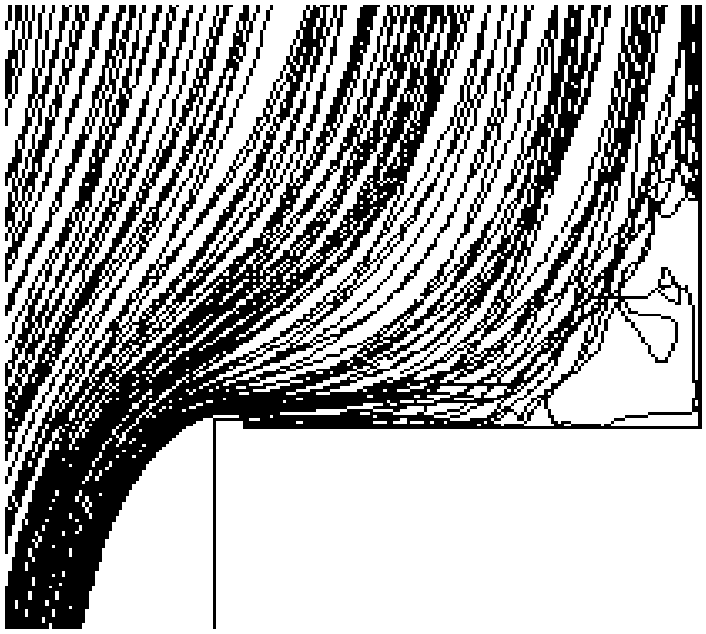

Figure 6.22 (a): Particle trajectories for protruded pipe depth of 1mm, for the case, V=5m/s, T=3mm, d_p=200μm

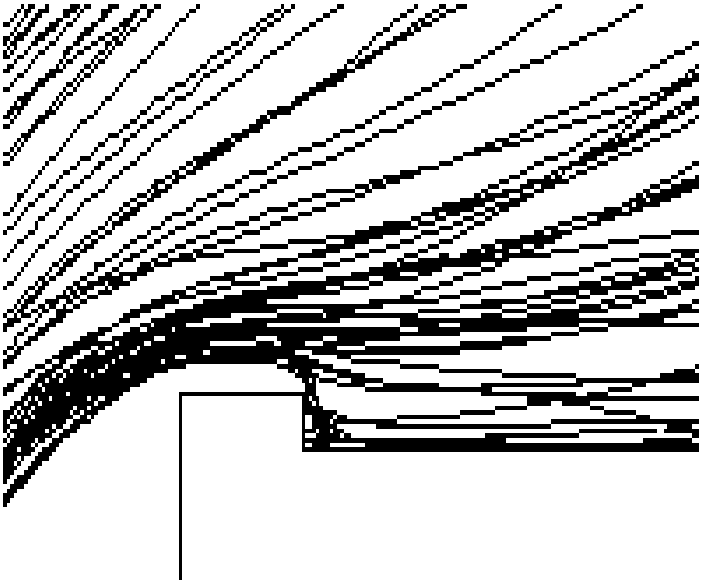

Figure 6.22 (b): Magnified view of particle trajectories for the same case as Figure 6.22 (a).

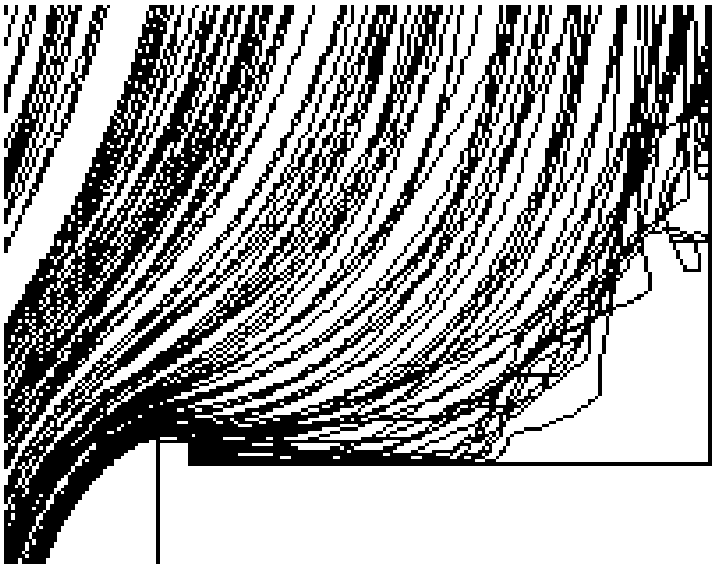

Figure 6.23 (a): Particle trajectories for protruded pipe depth of 2mm, for the case, V=5m/s, T=3mm, d_p=200μm.

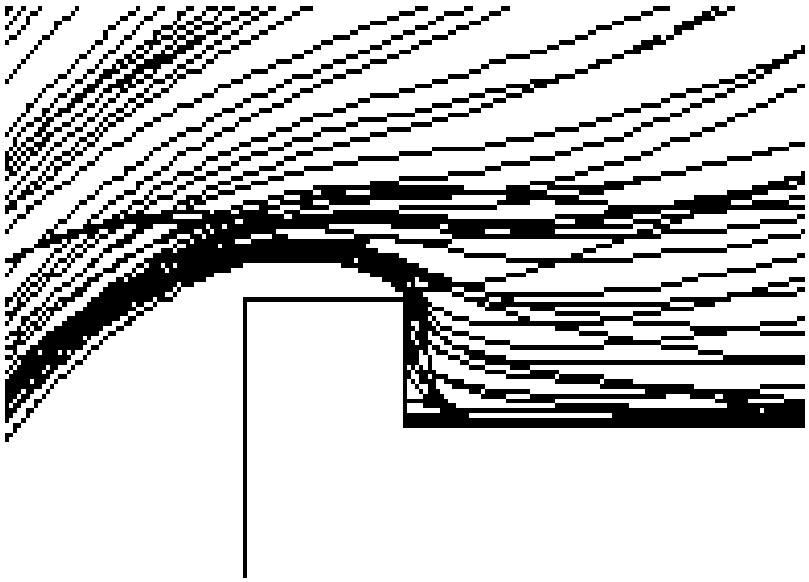

Figure 6.23(b): Magnified view of particle trajectories for the same case as Figure 6.23 (a).

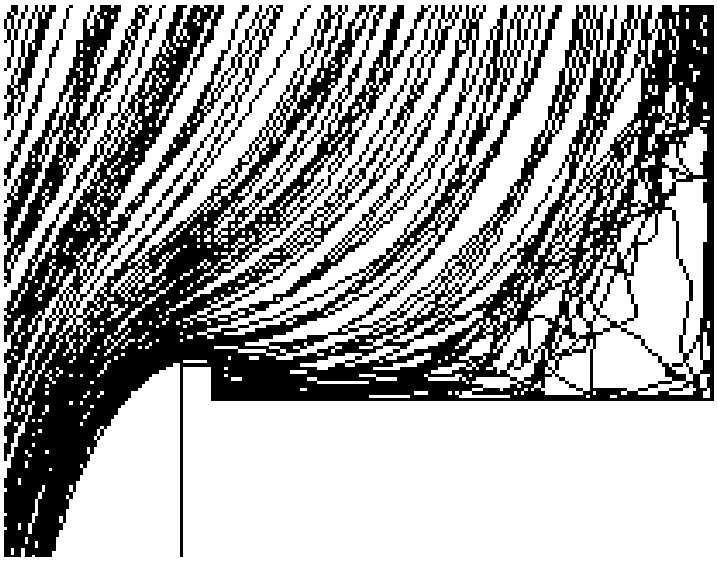

Figure 6.24 (a): Particle trajectories for protruded pipe depth of 3mm, for the case,

V=5m/s, T=3mm, d_p=200μm

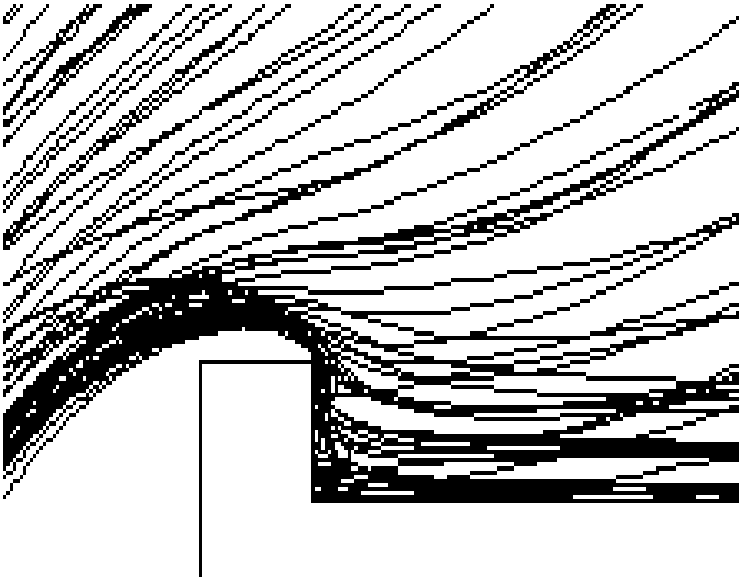

Figure 6.24 (b): Magnified view of particle trajectories for the same case as

Figure 6.24 (a).

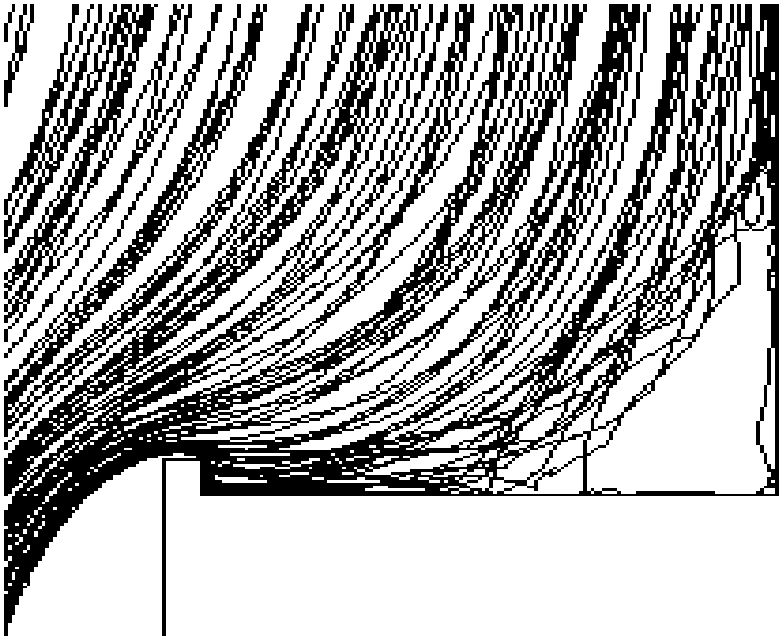

Figure 6.25 (a): Particle path lines for protruded pipe depth of 4mm, for the case, V=5m/s, T=3mm, d_p=200μm

Figure 6.25 (b): Magnified view of particle trajectories for the same case as Figure 6.25 (a).

6.7.2 Effect of Depth on Penetration Rates

To investigate the effect of depth variation on the penetration rate, Figure 6.26 is presented. The penetration curve in Figure 6.26 shows consistent pattern with the total erosion curve Figure 6.21. It is clearly seen that penetration rate is inversely proportional to the depth of the protruded pipe and the 1mm depth protruded pipe is the most erosion prone geometry. In order to have a better insight into the effect of protruded pipe depth on the total erosion and penetration rates, the average impact angle and average impact velocity values are computed for different protruded pipe depths. Figures 6.27 (a) & (b) show the variation of the average impact angle and average impact velocity with the change in protruded pipe depth. It is observed that both impact angle and impact velocity decrease with the increase in depth. This pattern explains the decrease of the erosion and penetration rates with the protruded pipe depth. The variation in protruded pipe depth causes changes in the streamline pattern of the ensuing flow. This change eventually causes changes in particle trajectories in the form of impact angle and impact velocity. As a result, erosion rate is influenced.

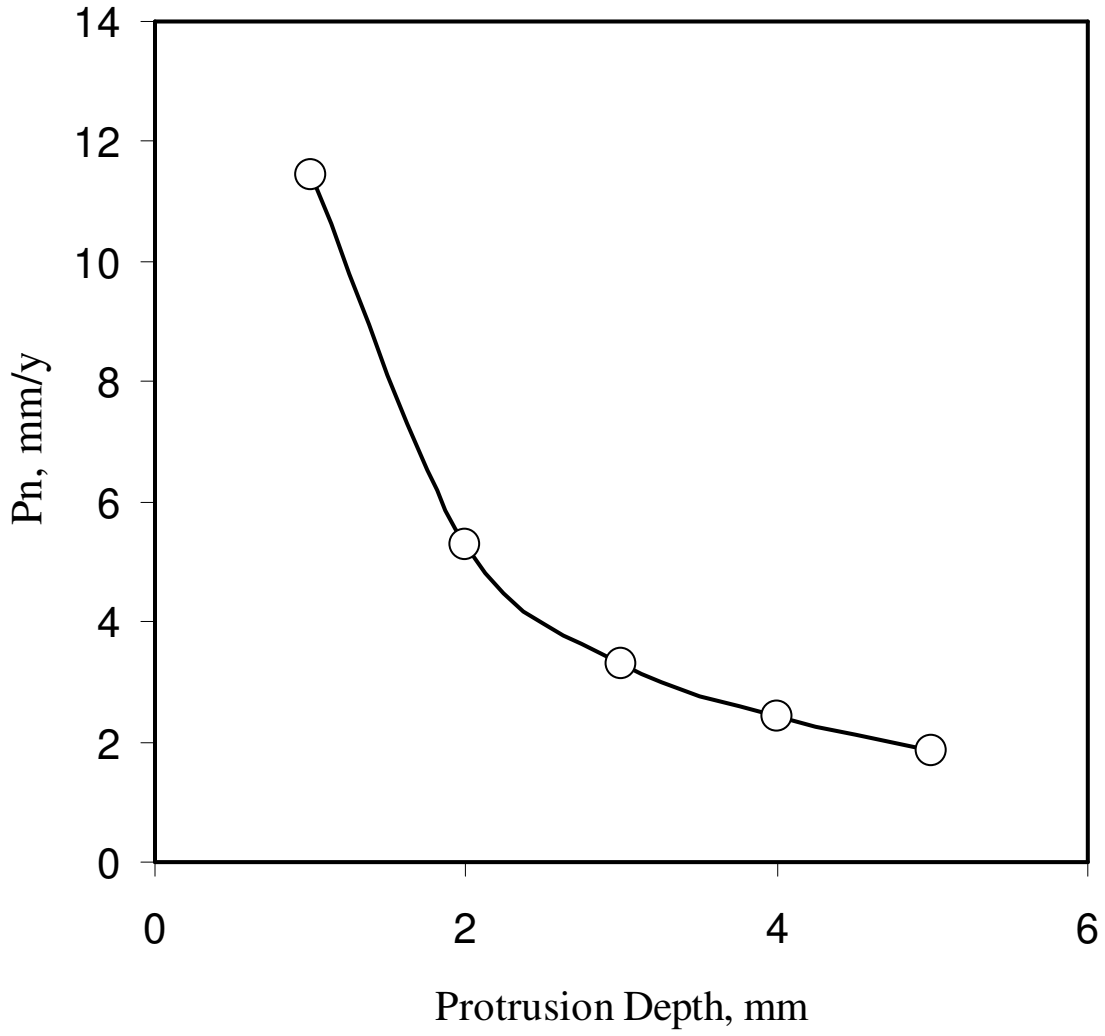

Figure 6.26: Influence of depth variation on penetration rate, for the case, T= 3mm, V= 5m/s, d_p= 200 μm.

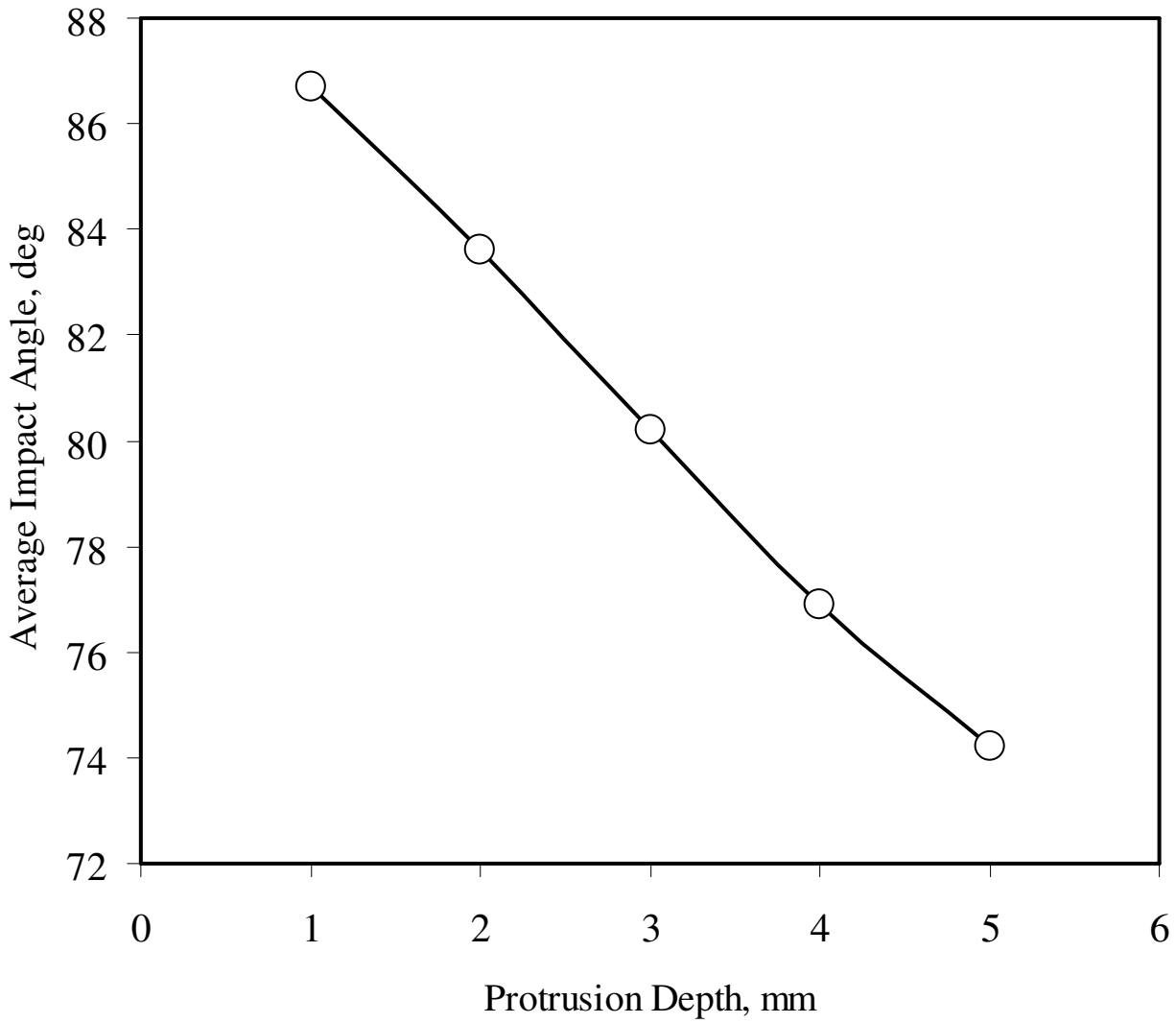

Figure 6.27 (a): Average Impact angle variation with protrusion depth, for the case T= 3mm, V= 5m/s, d_p= 200 μm.

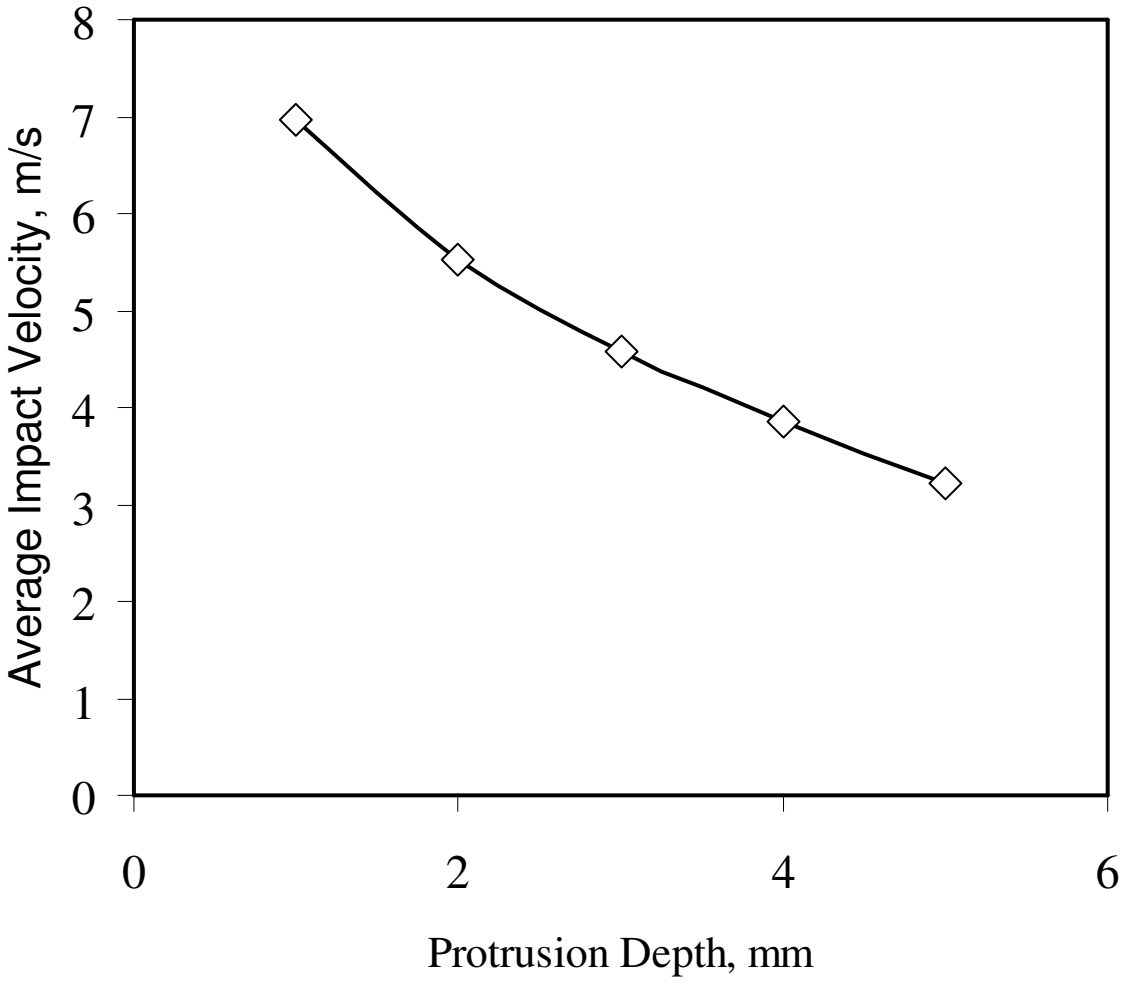

Figure 6.27 (b): Average impact velocity variation with protrusion depth, for the case T= 3mm, V= 5m/s, d_p= 200 μm.

6.8 Effect of Protrusion Thickness on Erosion and Penetration rates

The effect of protruded pipe thickness on the erosion and penetration rates was investigated. Protruded pipe thickness was varied for a range 1mm to 5mm with steps of 1mm. Inlet flow velocity of 5m/s, protruded pipe depth 5mm, particle diameter 200 μm are kept constants for this analysis.

6.8.1 Effect of Protrusion Thickness on the Total Erosion Rates

The influence of protruded pipe thickness on the total erosion rate was found to be dominant. The influence of protruded pipe thickness on total erosion rate is presented in Figure 6.28. It is observed that the total erosion is highest when the thickness is minimum and vice versa. Similar results are obtained for both stochastic and non-stochastic approaches. To investigate this behavior, particle trajectories for two values of thickness (3mm and 4 mm) are plotted. Figures 6.29-6.30 show the trajectories. Careful monitoring of the Figures reveals that the curvature of particle pathlines increases with increasing pipe thickness. For thickness of 3mm, particle trajectories are more parallel to the wall than they are for the 4mm thickness. This implies for thickness 3mm, the impact angles are larger than those of thickness 4mm.

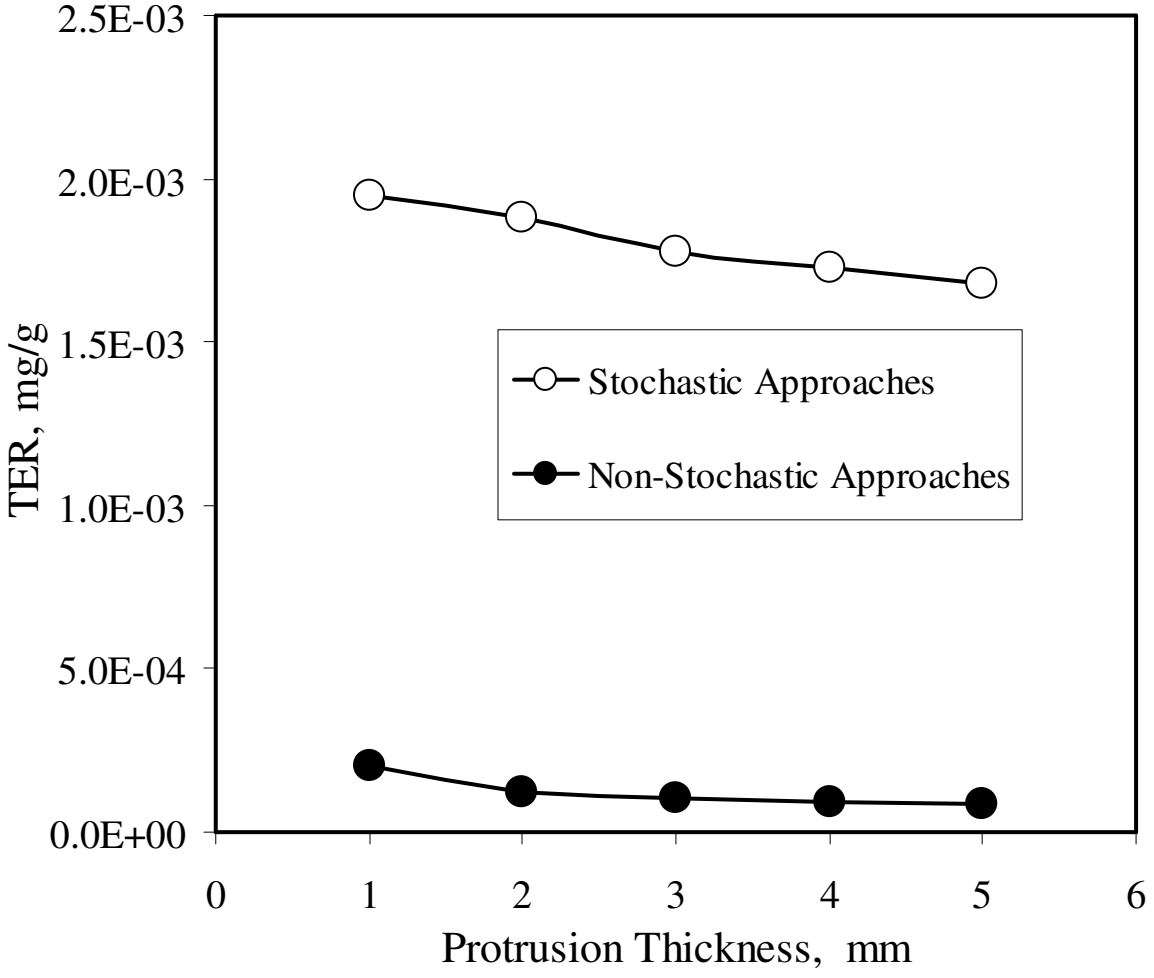

Figure 6.28: Effect of thickness variation on total erosion rate, for the case, H= 5mm, V= 5m/s, dp= 200 μm.

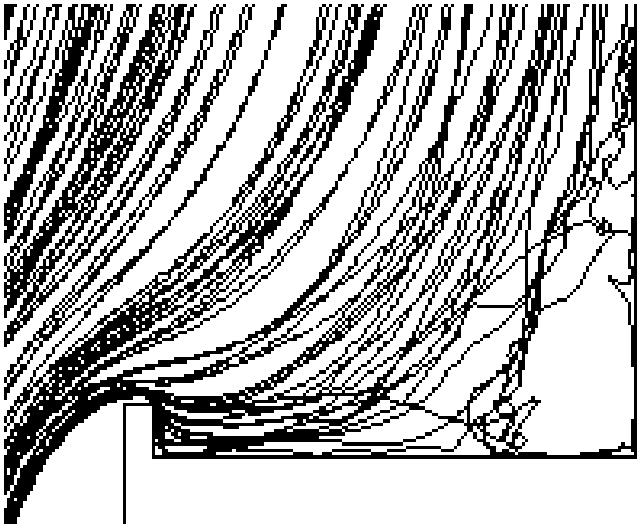

Figure 6.29 (a): Particle trajectories for thickness of 3mm, for H= 5mm, V=5m/s, dp= 200 μm.

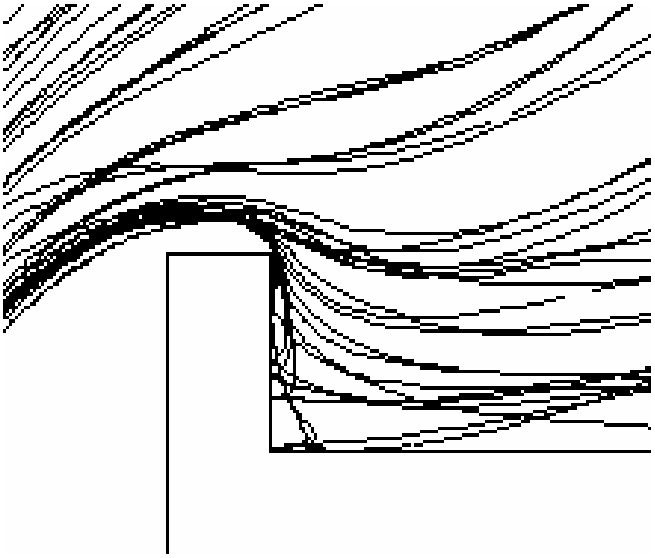

Figure 6.29 (b) Magnified view of the particle trajectories for the same case as Figure 6.29 (a).

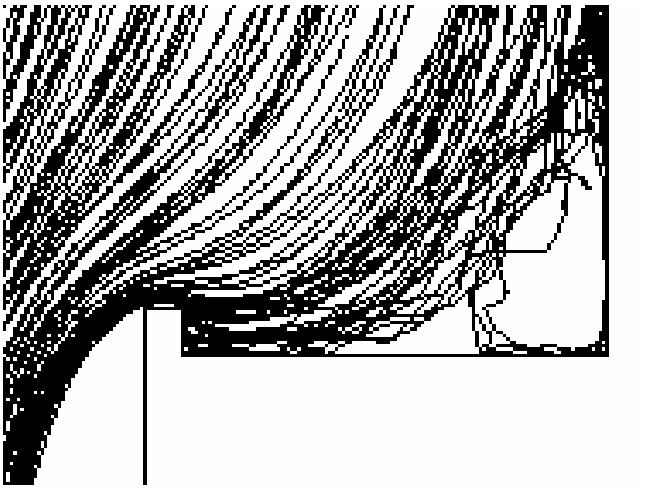

Figure 6.30 (a) Particle path lines for protruded pipe thickness of 4mm, for H= 5mm, V=5m/s, dp= 200 μm.

Figure 6.30 (b): Magnified view of the particle trajectories for the same case as Figure 6.30 (a).

6.8.2 Effect of Protrusion Thickness on Penetration Rates

The penetration curve in Figure 6.31 shows a similar pattern like that of the total erosion curve in Figure 6.30. The smallest thickness of the protruded pipe yields the largest value of penetration rate to occur. Average impact angle and average impact velocity are computed for different thicknesses. These values are plotted in the Figures 6.32 (a) and (b). It is observed that both average impact velocity and average impact angles decrease with the increasing thickness. As a result, the geometric configuration of 1mm thickness is found out to be the most erosion prone geometry.

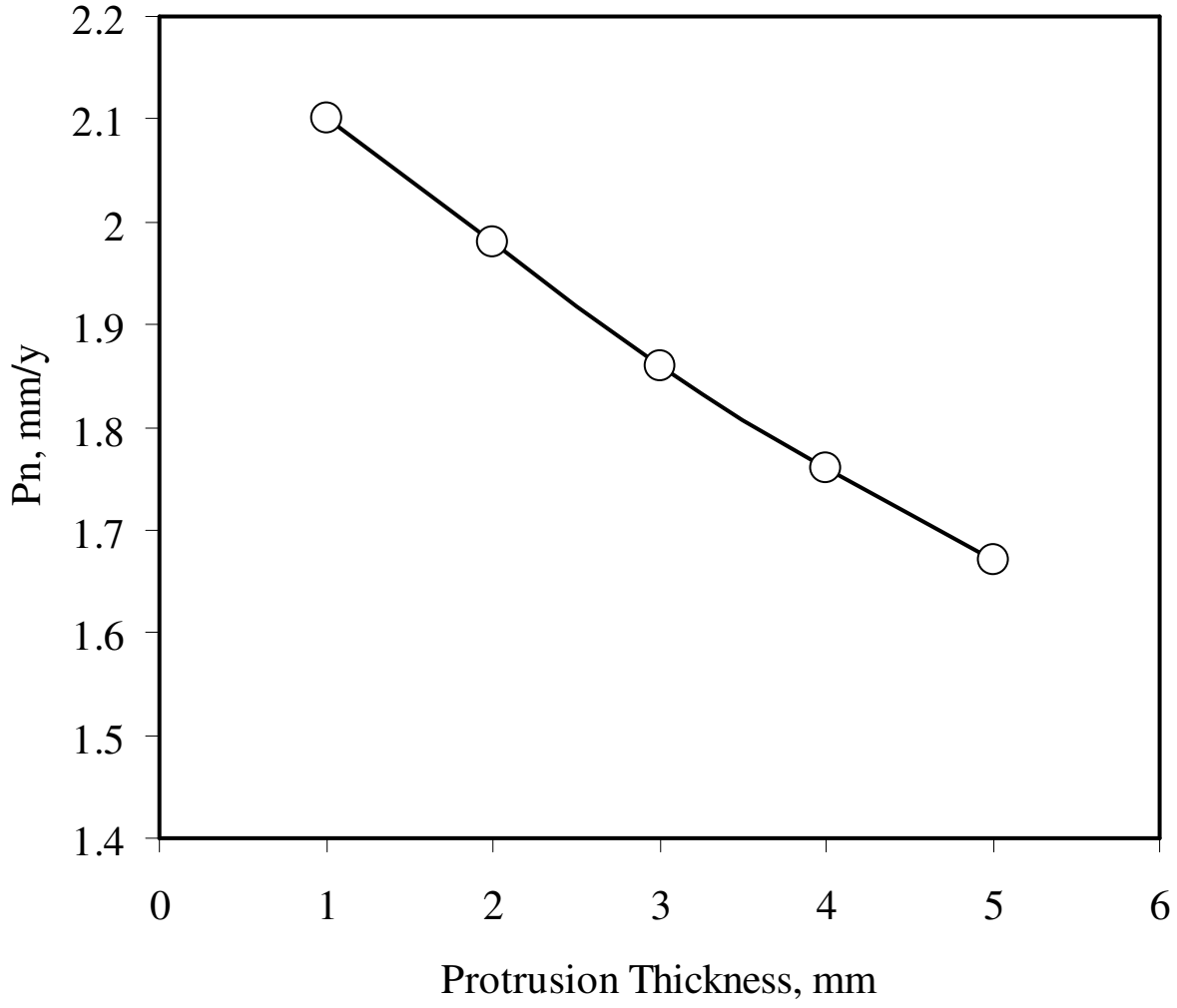

Figure 6.31: Effect of the protruded pipe thickness on penetration rate, for the case

H= 5mm, V= 5m/s, dp =200 μm

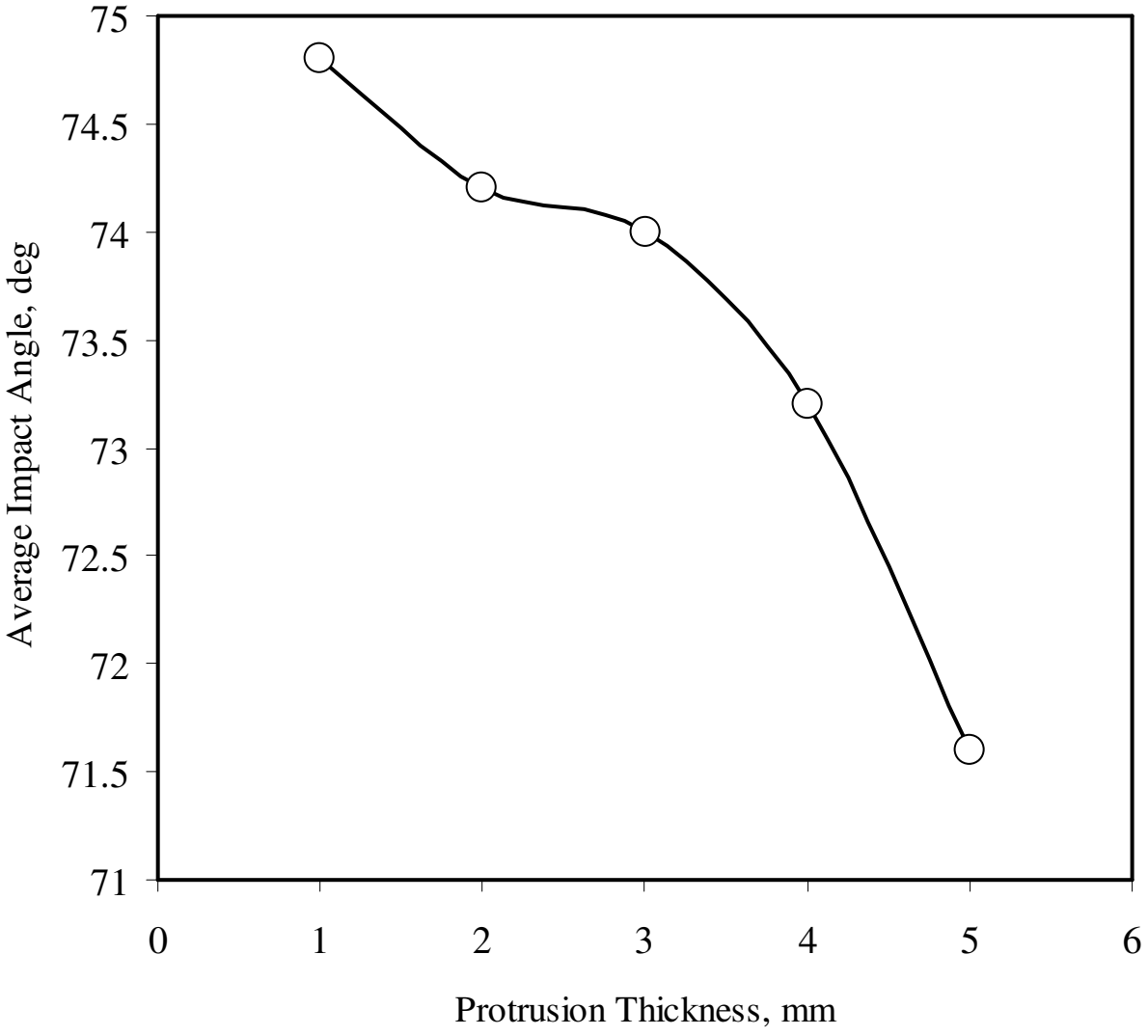

Figure 6.32 (a): Average Impact angle variation with protrusion thickness, for the case H= 5mm, V= 5m/s, dp =200 μm.

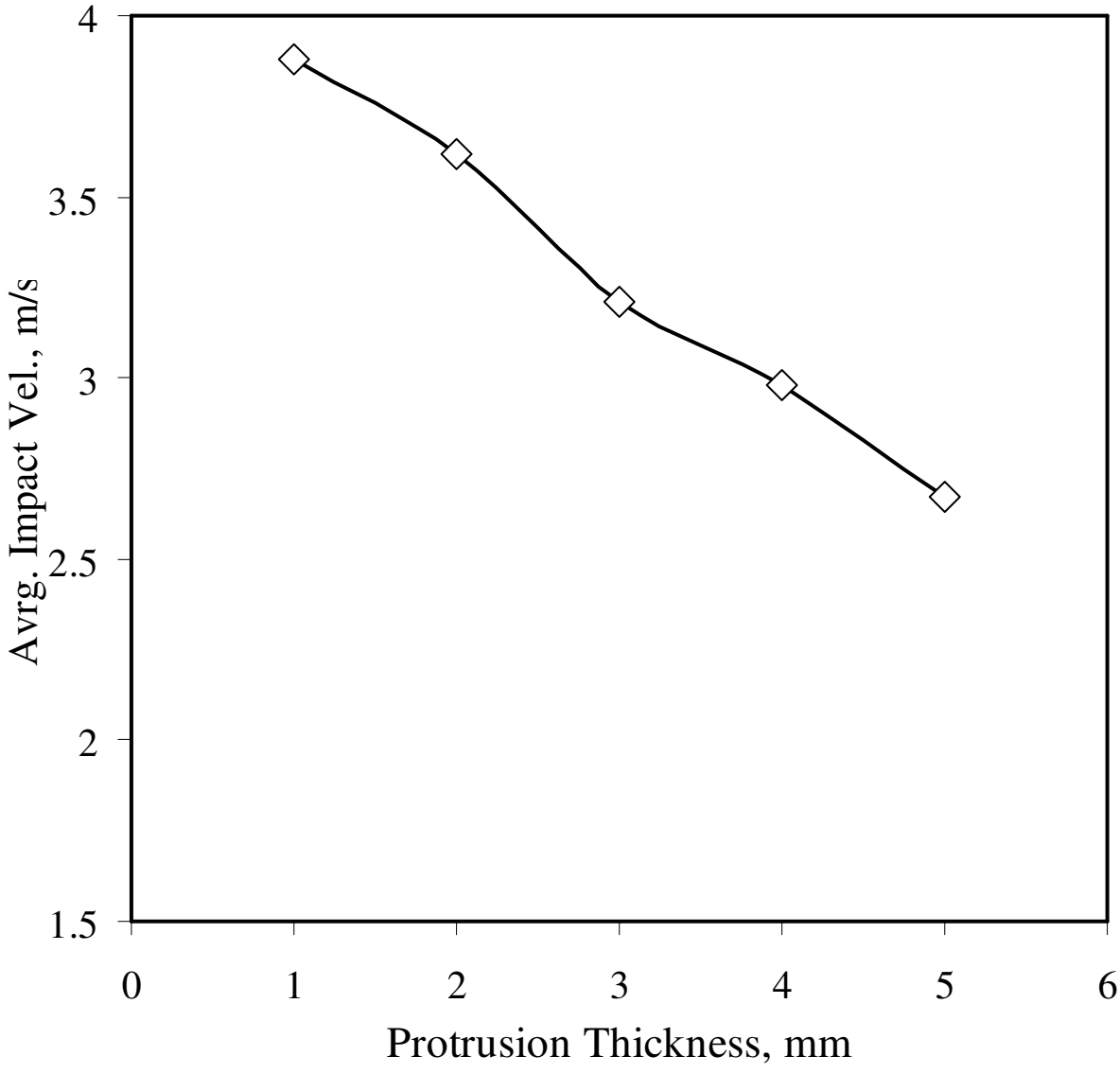

Figure 6.32 (b): Average Impact velocity variation with protrusion thickness, for the case H= 5mm, V= 5m/s, dp =200 μm.

6.9 Effect of Contraction Ratio on Erosion Rates

In the present work, contraction ratio, Cr, is defined as the ratio of diameter of small bore pipe to large bore pipe. The effect of the contraction ratio on total erosion and penetration rates, for inlet flow velocity of 5m/s, protruded pipe depth of 5mm and thickness of 3mm are shown in Figures 6.33-34. It is clearly seen both total erosion and penetration rates are inversely proportional to the contraction ratio of the geometry. For the flow and geometric configurations mentioned above, the total erosion rate is reduced ten times as the contraction ratio is increased from 0.2 to 0.5. Penetration rate also decreased about 9 times when the contraction ratio is increased from 0.2 to 0.5. For the lowest value of the contraction ratio (in this case 0.2), the fluid stream is contracted to the highest extent. As a result, higher values of impact velocity and impact angle are occurred causing the highest value of erosion rate. As the contraction ratio increases, (i.e. the small-bore pipe diameter gradually increases), the fluid stream contraction is gradually decreased. As a result, the resulting lower values of impact angle and impact velocity caused lower values of total erosion and penetration rates eventually. Therefore, the contraction ratio of the pipe geometry has a very significant influence on the erosion rates of the protruded pipe.

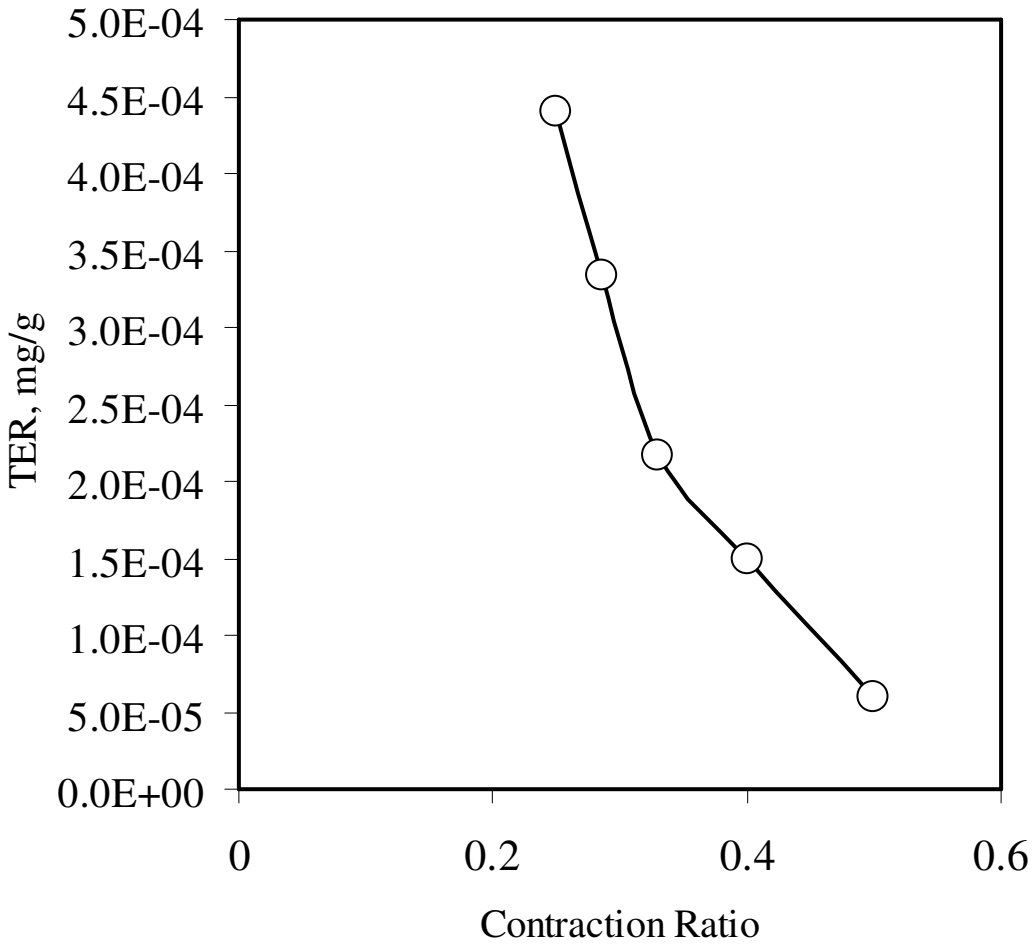

Figure 6.33: Effect of contraction ratio on total erosion rate, for the case V=5m/s, H= 5mm and T= 3mm, d_p=200 μm.

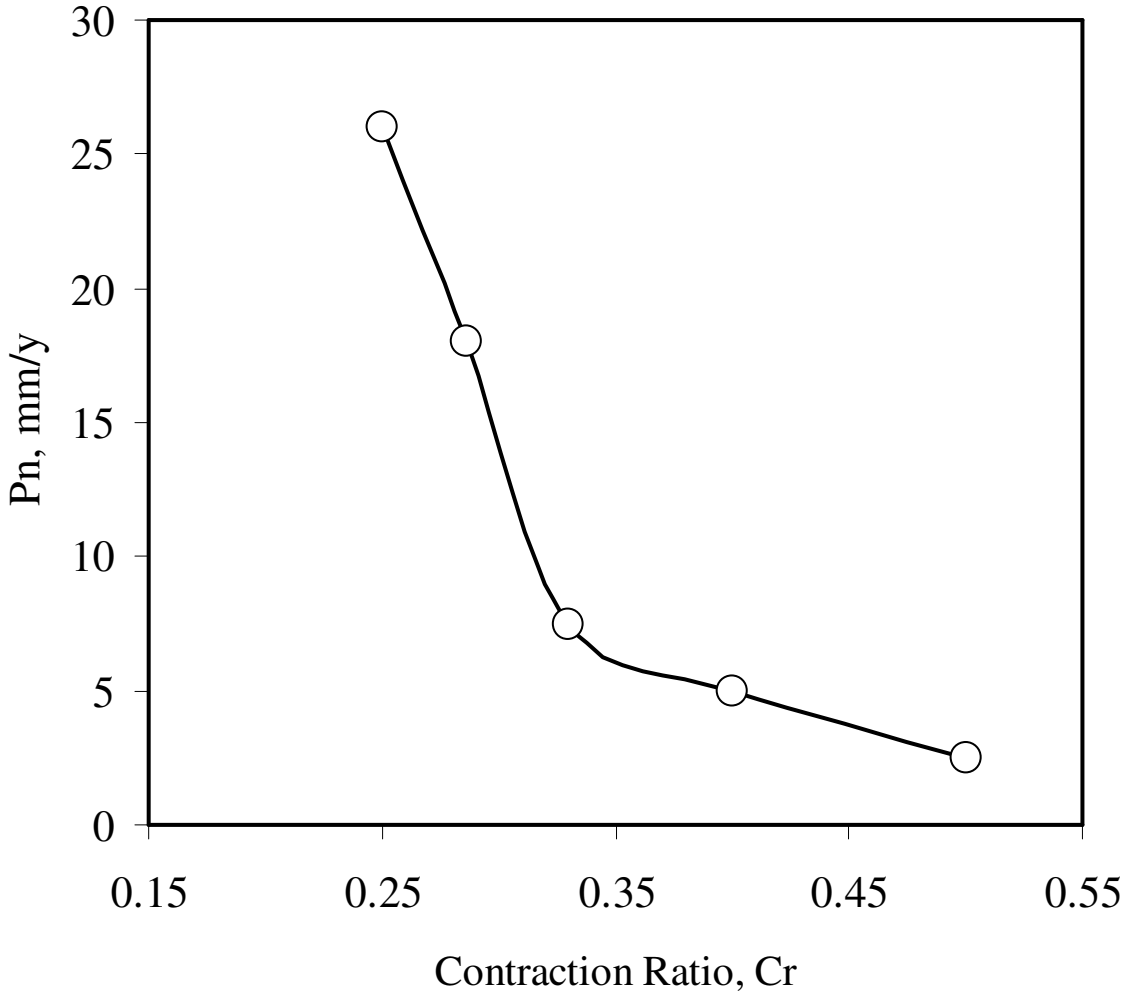

Figure 6.34: Effect of contraction ratio on penetration rate, for the case V=5m/s, H= 5mm and T= 3mm, , d_p=200 μm.

6.10 Effect of Material on Erosion Rates

Due to the distinct properties of each material, the erosion rate is also different for different materials. Edwards et al. (2000) proposed their own empirical equation for the calculation of the erosion rate of carbon steel and aluminum, which was used in the present calculations. From their experimental results, Edwards et al. (2000) proposed an empirical equation for carbon steel and aluminum. Moreover, they specified different values of the empirical constants contained in that equation. Total erosion rate versus the BHN (Brinell Hardness Number) curve is obtained in Figure 6.35 to show comparison in total erosion rate of carbon steel and aluminum. In Figure 6.35, it is observed that aluminum has very high erosion rate compared to carbon steel. From Figure 6.35, it is clear that the erosion rate decreases as the material hardness number, BHN increases. Softer materials have lower BHN and more prone to erosion. Moreover, from the curve in Figure 6.35, the erosion rate of a material having BHN in between Aluminum and carbon steel can be approximated.

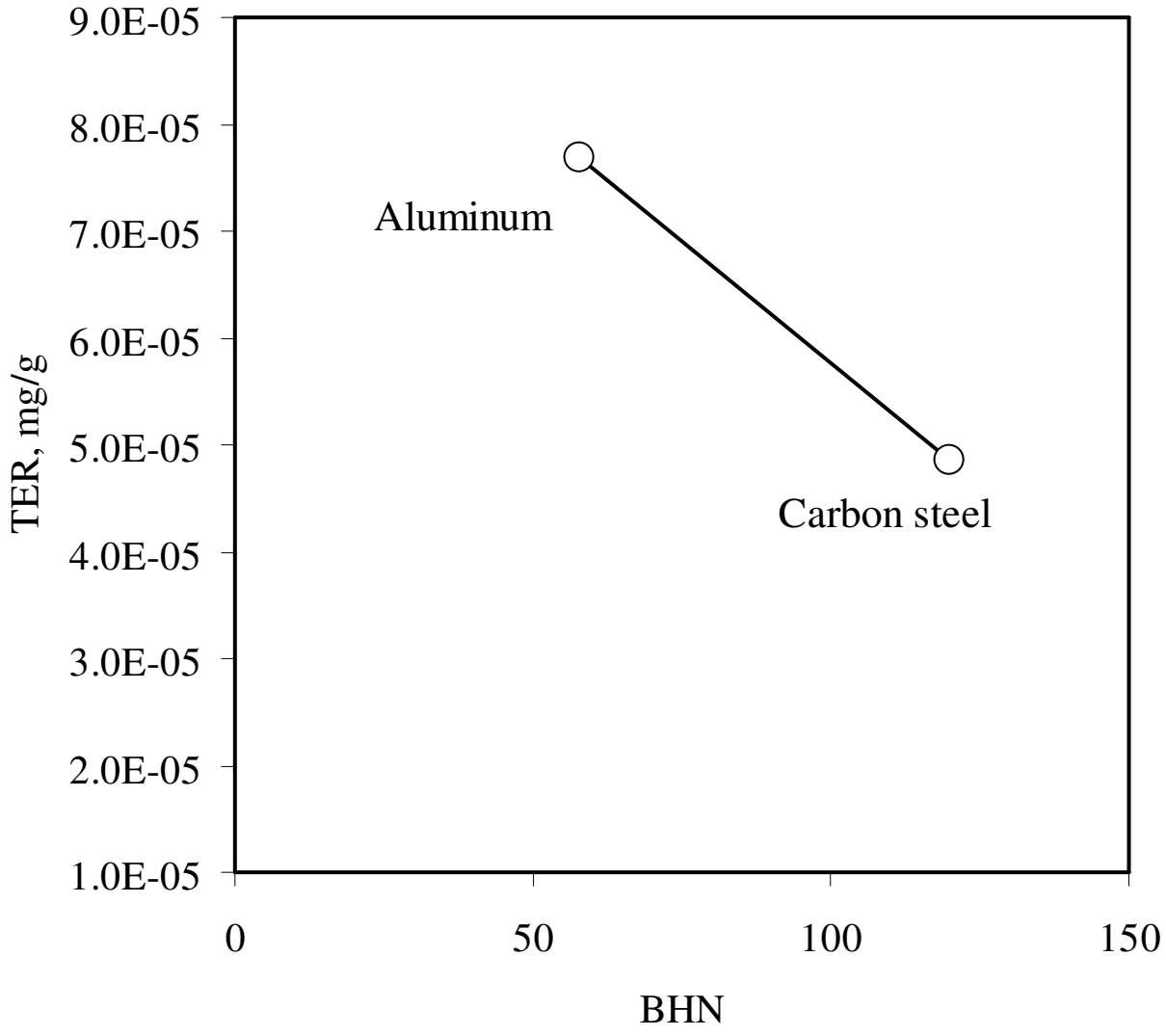

Figure 6.35: Effect of material hardness number BHN on TER of the protruded pipe, for the case, H= 5mm, V= 5m/s, d_p= 200 μm, T= 3mm.

6.11 RNG Model vs. Reynolds Stress Model

In the present work, the entire calculations are performed using the Renormalized group (RNG) option available in the k-ε model. This model is suitable for rapidly strained flow and for flows that encounter streamlines curvatures. In order to validate the results, some calculations are performed using Reynolds's Stress model (RSM). This model is considered the most comprehensive among the current turbulence models available to analyze strained flow analysis (Wilcox 2000).

Calculation for inlet flow velocity and particle diameter variation and their influence on total erosion rate & penetration rate are done in RSM and comparison is made between RNG and RSM results. For an inlet flow velocity of 10 m/s, the difference in the total erosion and penetration rates between the calculated values using the two models (RNG and RSM) is about 8% for total erosion rate and about 10% for the penetration rate, as shown in Figures 6.36 (a) & (b) . Below 5m/s, both curves are almost identical with a difference in values not exceeding 2%. Similar type of agreement is obtained for particle diameter variation and its influence on erosion and penetration rates in the Figures 6.37 (a) & (b). So the validity of the calculations performed in the present study by choosing the RNG model option, holds true.

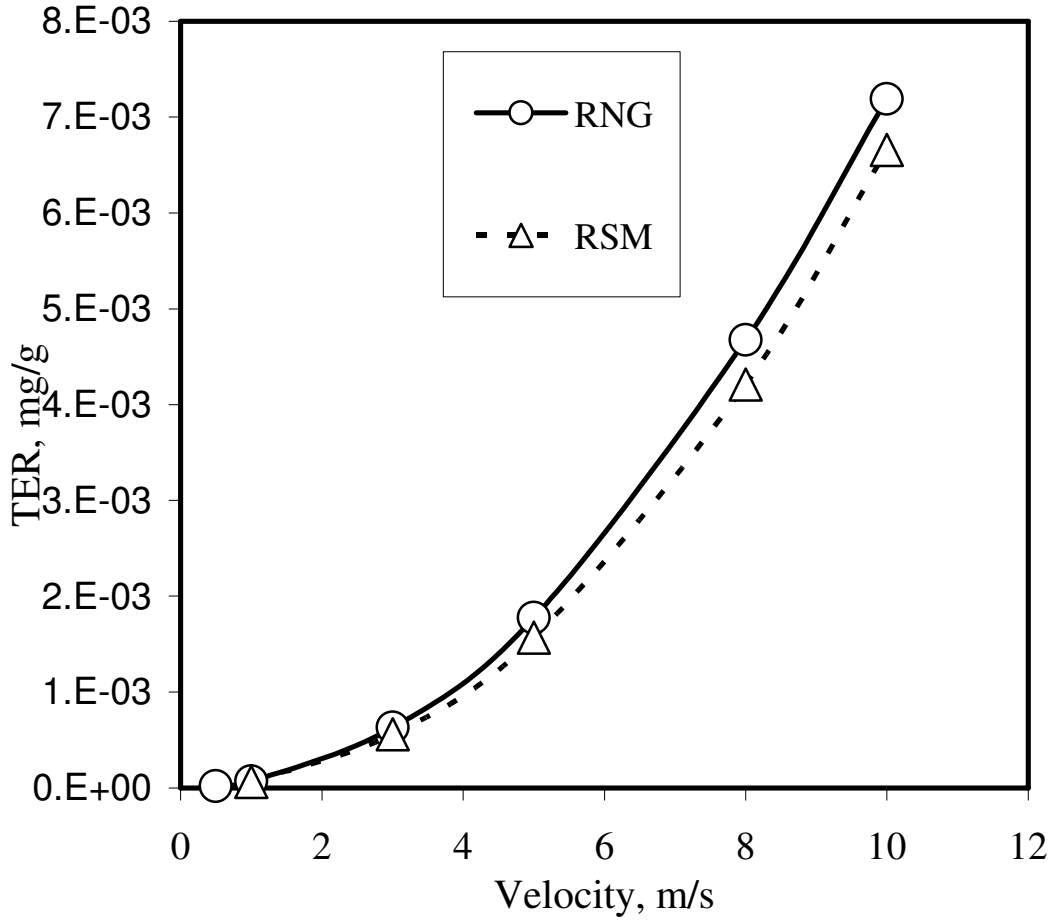

Figure 6.36 (a): Comparison between RNG and RSM model on total erosion rate, for the case, H= 5mm, V= 5m/s, T= 3mm.

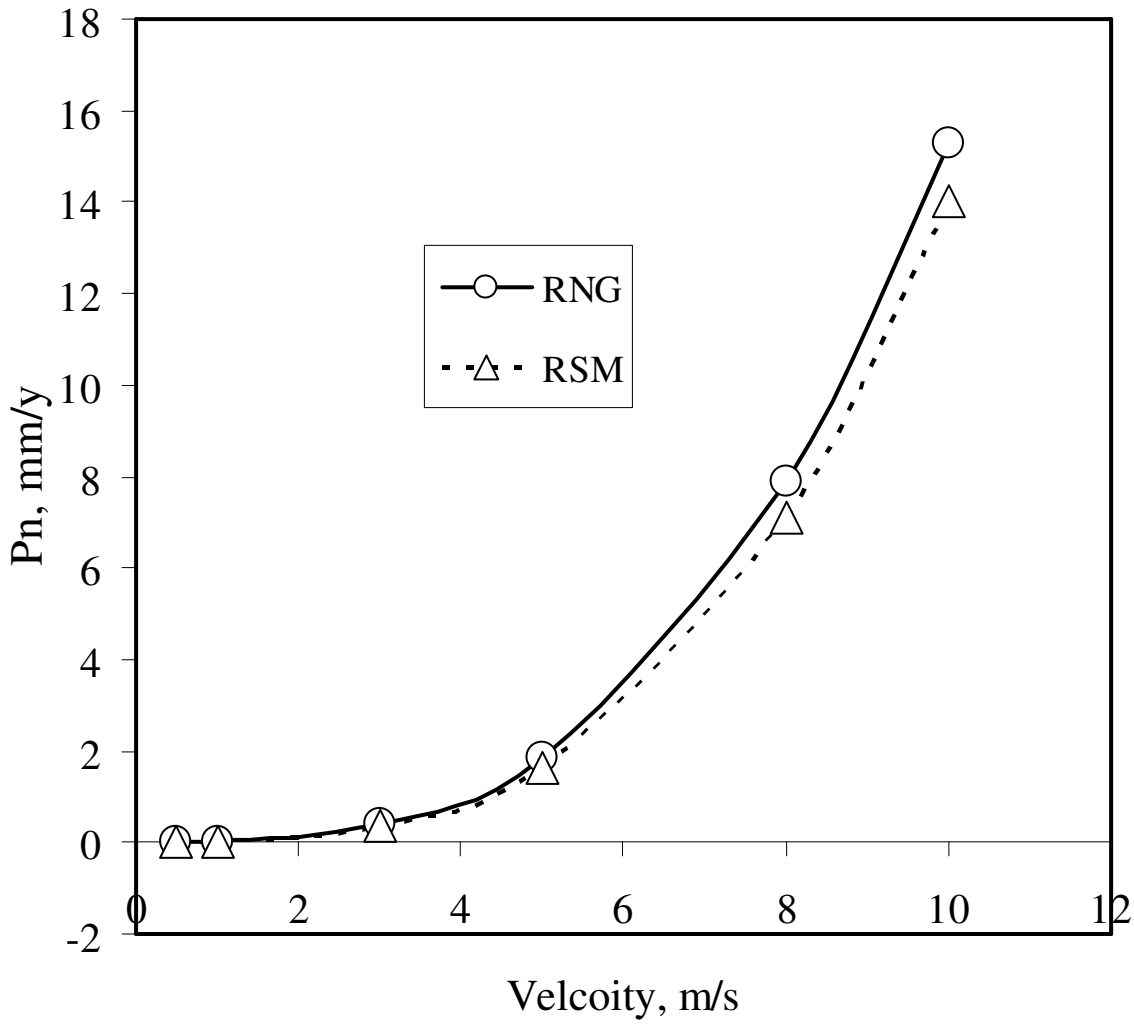

Figure 6.36 (b): Comparison between RNG and RSM model on penetration rate, for the case, H= 5mm, V= 5m/s, T= 3mm.

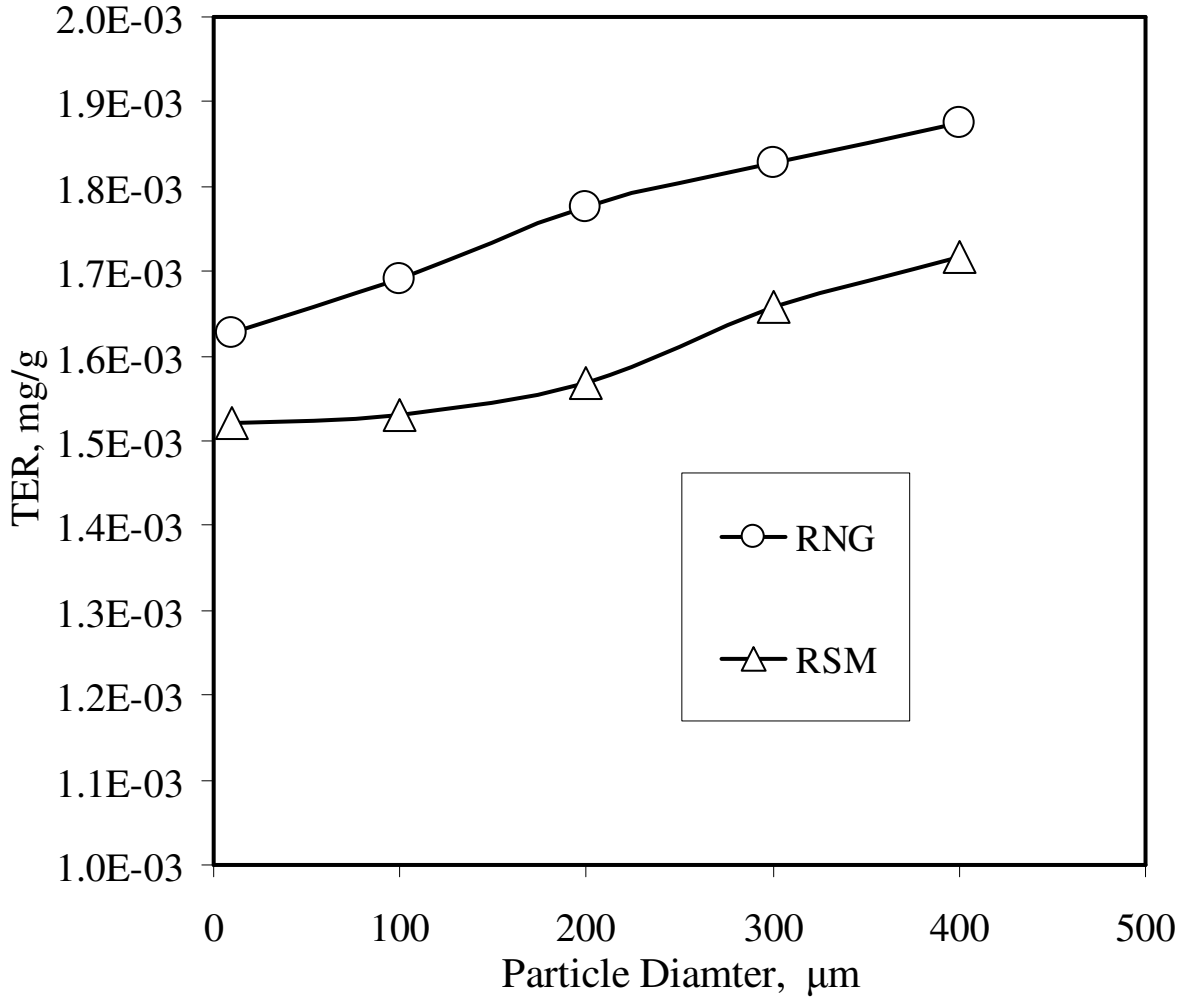

Figure 6.37 (a): Comparison between RNG & RSM model values for the influence of particle diameter on total erosion rate, for the case, V=5m/s, H= 5mm, T= 3mm.

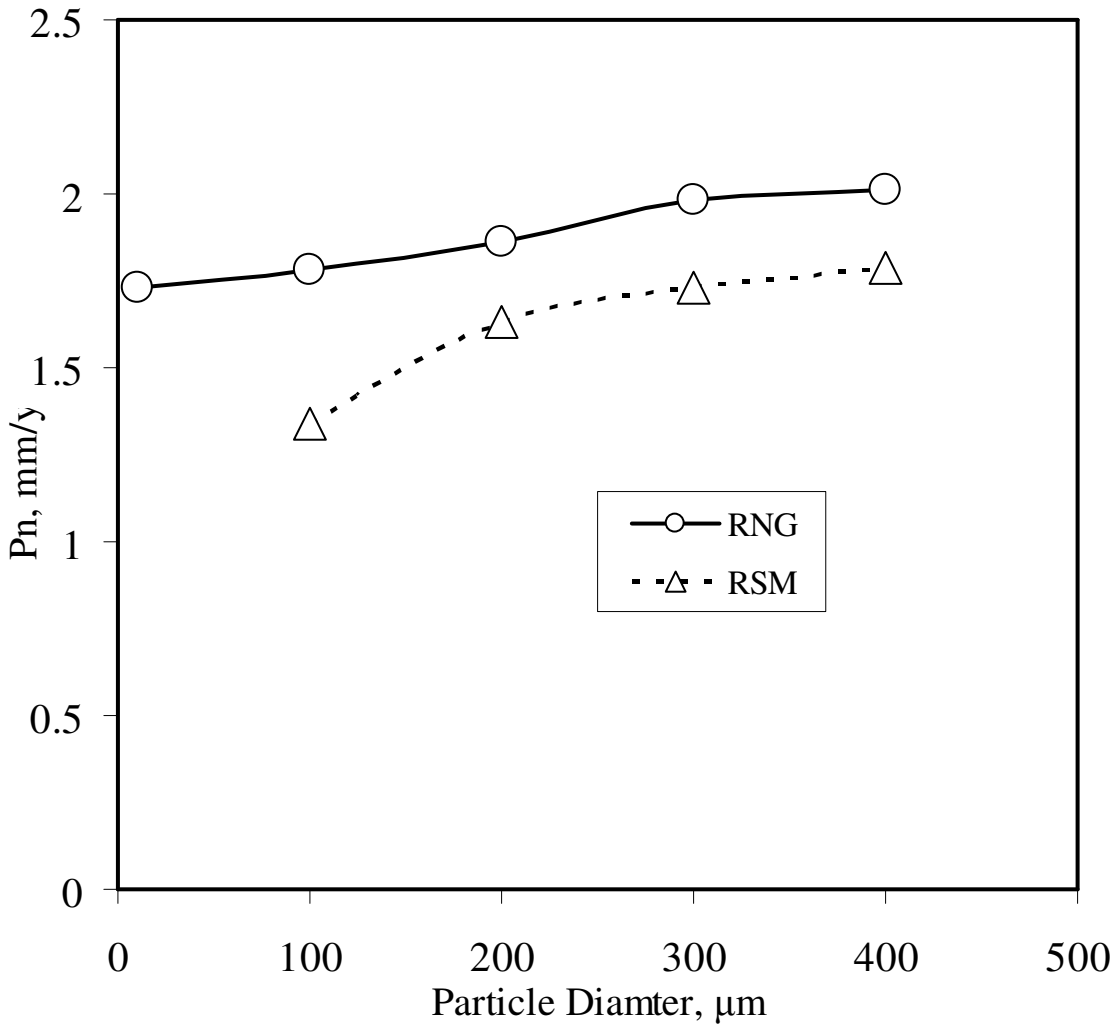

Figure 6.37(b): Comparison between RNG & RSM model values for the influence of particle diameter on penetration rate, for the case, V=5m/s, H= 5mm, T= 3mm.

6.12 Determination of a Threshold Depth

The erosion pattern in the protruded pipe depends strongly on the protrusion depth. A prime finding in this research is that the impacting particles are hitting only the outer surface of the protruded pipe. It was previously assumed that the face surface would be the impacted surface. The fluid streamline patterns are altered due to the presence of the protruded pipe that caused this difference. One of the objectives of this study is to determine the protruded pipe depth (for a certain contraction ratio), below which the impacting particles start impacting any surface other than the outer surface. Such depth is termed as the threshold depth in the present study. Different depths of 0.2mm, 0.1mm, 0.08mm, 0.05mm are examined for a flow condition of 10 m/s, particle diameter of 400 μm and contraction ratio of 0.5. Stochastic particle trajectories are shown in Figures 6.38 (a)-(d). Particle impact positions are observed carefully to check whether particles are only impacting the outer surface. In Figure 6.38 (a), it can be seen that the particles are bypassing all the surfaces of protruded pipe for a protrusion depth of 0.05mm. For a depth of 0.08 mm, the particles are impacting the face surface of the protrusion only [Figure 6.38 (b)]. In Figure 6.38 (c), it is observed that the particles started to impact the outer surface when the depth is 0.1 mm. The same type of impact at outer surface is observed for depth of 0.2mm [Figure 6.38 (d)]. From this analysis, two domains can be selected based on the impact location of the particles. Particles will impact the face surface or bypass the protruded pipe completely if the depth is less than 0.1 mm (H <0.1mm). When the depth is 0.1 mm or larger, the particles will start impacting the outer surface. This depth is termed as the “threshold” depth for a contraction ratio of 0.5.

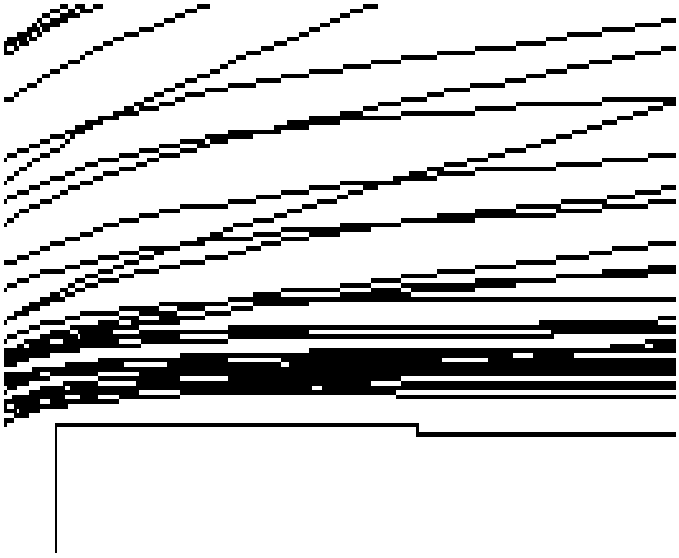

Figure 6.38 (a): Particle trajectories for a protrusion H= 0.05 mm, for Cr=0.5, T=3mm, V=10m/s, d_p=200 μm.

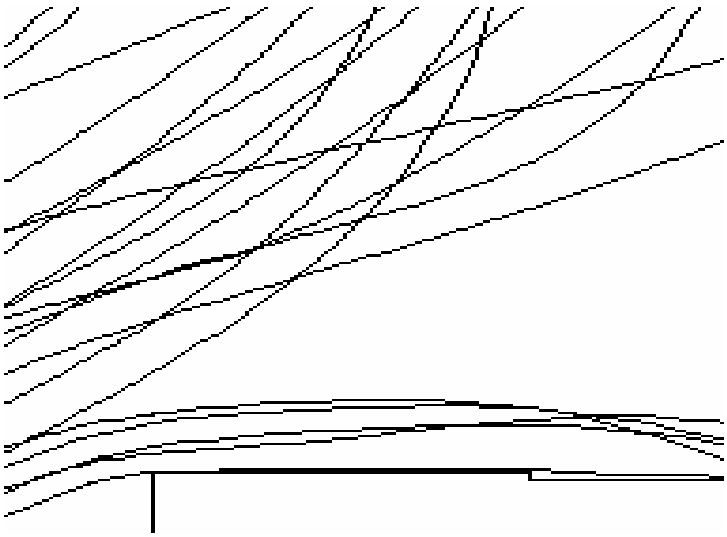

Figure 6.38 (b): Particle trajectories for a protrusion depth 0.08 mm, for Cr=0.5, T=3mm, V=10m/s, d_p=200 μm.

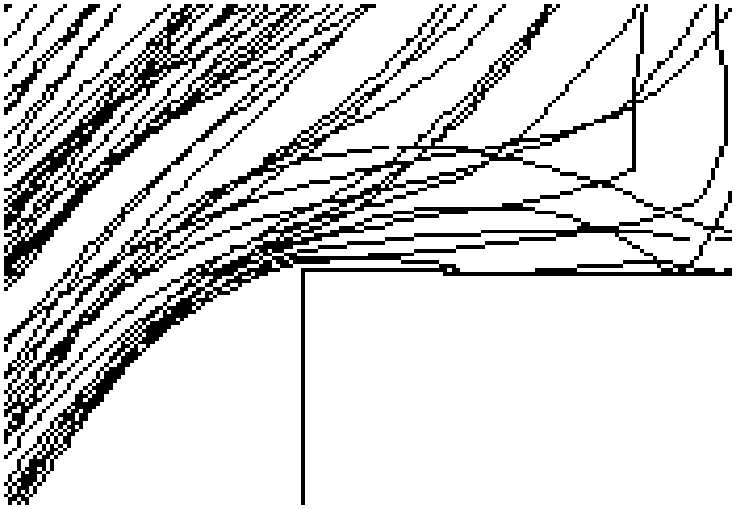

Figure 6.38 (c): Particle trajectories for a protrusion depth 0.1 mm, for Cr=0.5, T=3mm, V=10m/s, d_p=200 μm.

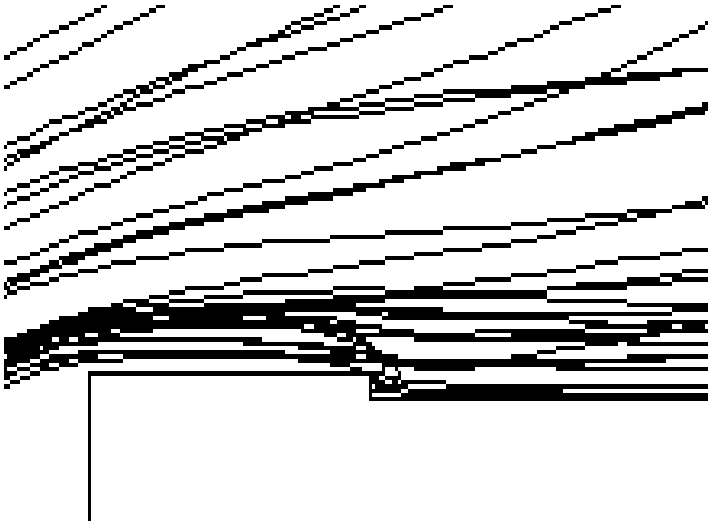

Figure 6.38 (d): Particle trajectories for a protrusion depth 0.2 mm, for Cr=0.5, T=3mm, V=10m/s, d_p=200 μm.

Another contraction ratio (Cr=0.75) is also considered to find out how the particles behave in that case. For a contraction ratio of 0.75, protrusion depths of 1mm, 0.8mm, 0.5 mm, 0.1mm, and 0.08mm are examined. It is observed that for protrusion depth of 0.08mm only, the particles are impacting the face surface only [See to Figure 6.39]. For depths greater than 0.08mm, particles are impacting the outer surface of protrusion. Therefore, for a contraction ratio of 0.75, two distinct phenomena are found. First phenomenon is that the particles are impacting the face surface of the protrusion only when $H \leq 0.08$ mm. The other one is that the particles impact the outer surface of the protruded pipe when $H > 0.08$mm.

In the present study, all subsequent erosion calculations are performed on the outer surface of the protruded pipe. The current analysis for determining a threshold depth limit will be very beneficial for any future work with geometries containing very small depth ($H<1$mm).

6.13 Additional Analysis of Erosion Phenomena

For acquiring more insight into the erosion phenomena for a pipe protruded in sudden contraction geometry, some additional analysis are done. In the preceding sections, influence of different flow and geometric parameters are examined on local and total erosion rate on individual geometry of the typical configuration [Table 6.2].

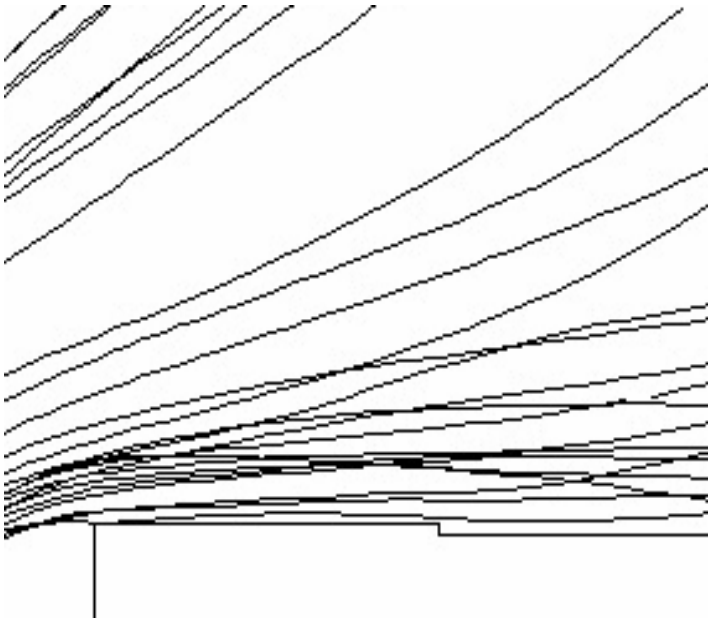

Figure 6.39: Particle trajectories for a protrusion depth 0.08 mm, for the case, Cr=0.75, T=3mm, V=10m/s, d_p=200 μm.

In the subsequent sections, analysis will be presented on the influence of inlet flow velocity and particle diameter on local and total erosion rates for different geometric configurations. The depth and thickness of the protruded pipe will be made constant alternatively and the influence of inlet flow velocity and particle diameter on either depth or thickness variation will be presented.

6.13.1 Variation in Local and Total Erosion Rates at different L/H

Local erosion rate variations for different particle diameter are observed at different normalized distances (L/H) along the protruded pipe depth. The inlet flow velocity is kept constant at 10 m/s. For this analysis, protruded pipe depth of 1mm and thickness of 3mm is kept unchanged. In the present work, depth is divided into 10 equal segments from the inner to the outer tip of the protruded pipe. Each segment is normalized by the entire length of the depth (in this case1mm). Erosion rate calculations are done at the mid point of each segment length. Figure 6.40 shows the pattern of the local erosion curve for a particle diameter range of 10 μm to 400 μm. Close observation of Figure 6.40 shows that the highest local erosion rate occurred at a normalized distance, L/H =0.05, for the entire particle diameter range. This value signifies that erosion phenomenon is localized near the inner tip of the outer surface of the protruded pipe. The magnitude of this local erosion rate is around 0.006 mg/g. Further observation of the results in Figure 6.40 shows that the highest local erosion rate occurred at a particle diameter of 400μm for all L/H values. The particle diameter 300 μm caused next higher erosion rate to occur at all L/H values. Next severe erosion rates occurred in the ascending order of particle diameters from 200 μm to 10 μm. Another inlet velocity of 8 m/s was employed to repeat the above analysis by keeping all other stated conditions

unchanged. Figure 6.41 shows the results. It is observed that the local erosion rate curves show similar trends to those of the curves in Figure 6.40. Alike the inlet velocity of 10 m/s, highest local erosion occurred at L/H= 0.05 for an inlet velocity of 8 m/s. This is same for the entire particle diameters range. Therefore, the erosion is localized at the inner tip of the outer surface of the protruded pipe for an inlet flow velocity of 8 m/s also. This value of the highest local erosion rate was found to be around $4x10^{-3}$ mg/g for a particle diameter 400μm. The subsequent higher local erosion rates occurred in an ascending order of the particle diameters from 300 μm to 10 μm. To investigate why this erosion phenomenon is localized at the inner tip of the protruded pipe; particle trajectory analysis was performed to observe the particle impingement angles. Figure 6.42 shows the particle path lines to facilitate the analysis. It is observed that near inner tip of the outer surface of the protruded pipe, particles impact the surface in almost straight angles. By approaching from inner tip to the outer tip of the outer surface, these particle path lines were found to become comparatively oblique. As a result, the impingement angle decreases due to gradual streamline curvature. Comparative analysis is done to observe the variation in total erosion rates for the above-mentioned two inlet flow velocity cases discussed. Figure 6.43 shows the comparison. Higher of the two inlet flow velocities, 10 m/s, resulted higher total erosion rates for the entire range of diameter.

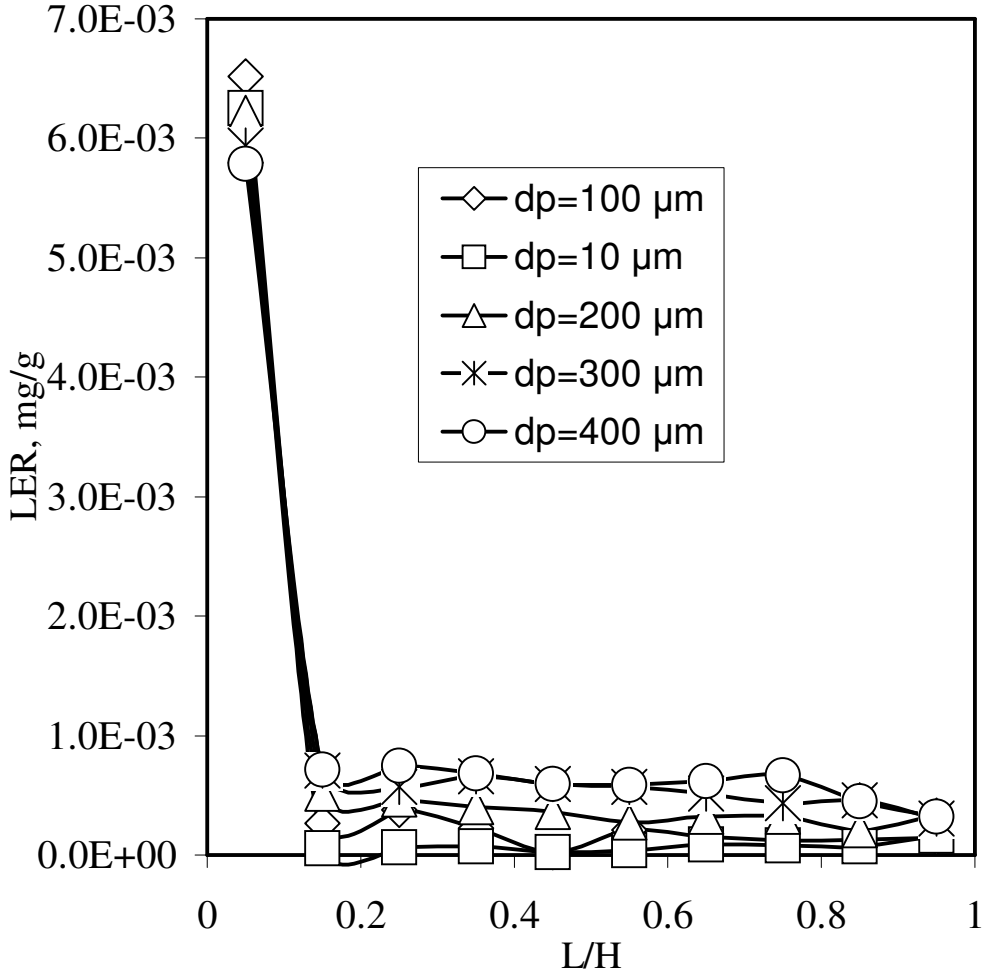

Figure 6.40: Variation of local erosion rates at different normalized distances along depth (L/H) for different particle diameters (for the case V= 10 m/s, H= 1mm, T= 3 mm).

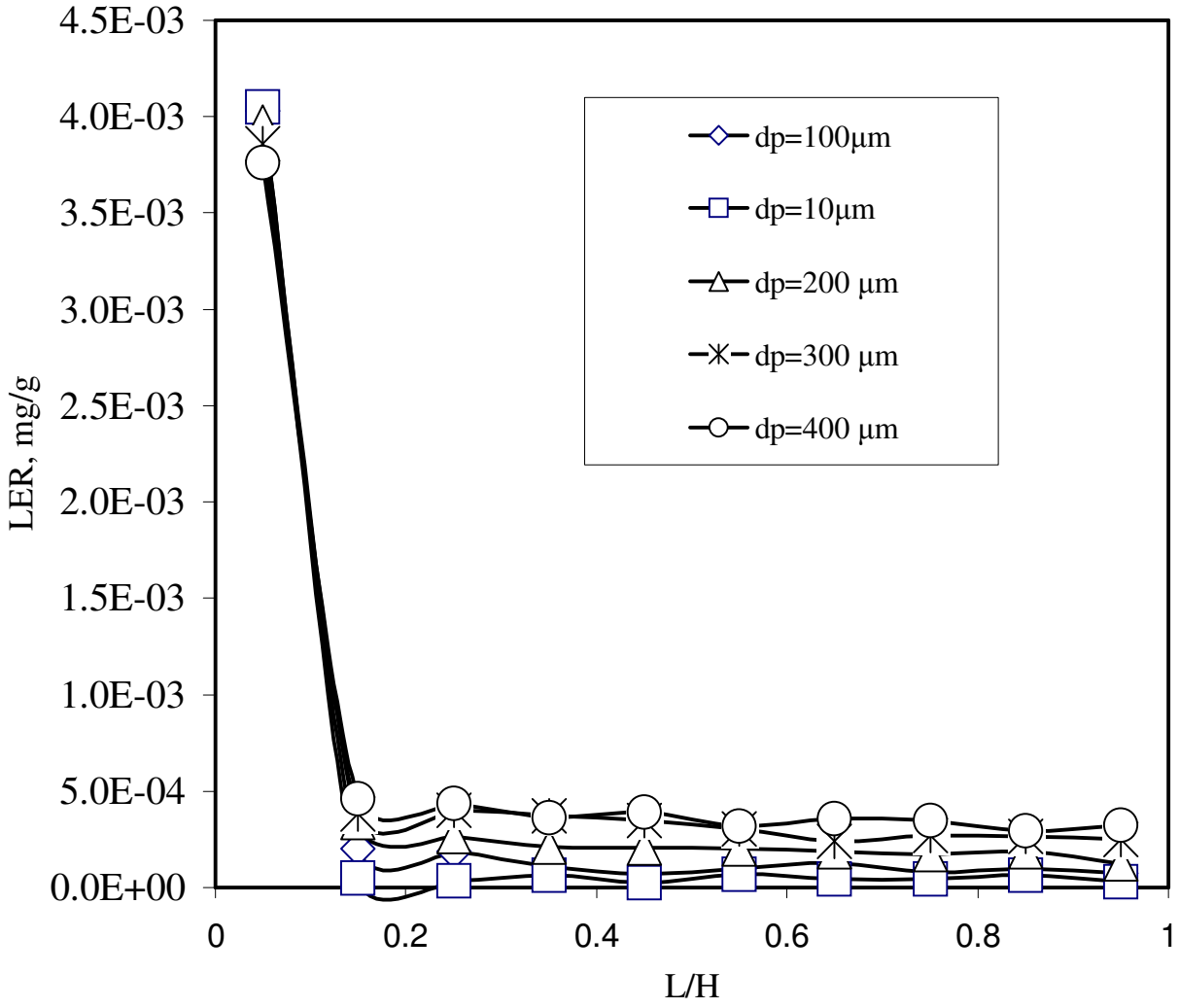

Figure 6.41: Variation of local erosion rates at different normalized distances along depth (L/H) for different particle diameters (for the case V= 10 m/s, H= 1mm, T= 3 mm).

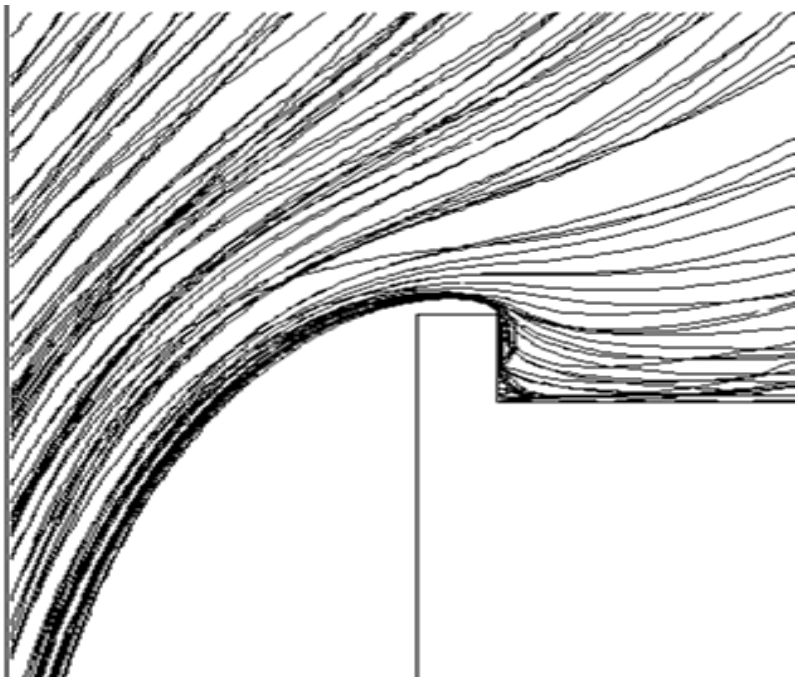

Figure 6.42: Particle trajectories for the case H= 1mm, T= 3mm, V=10m/s.

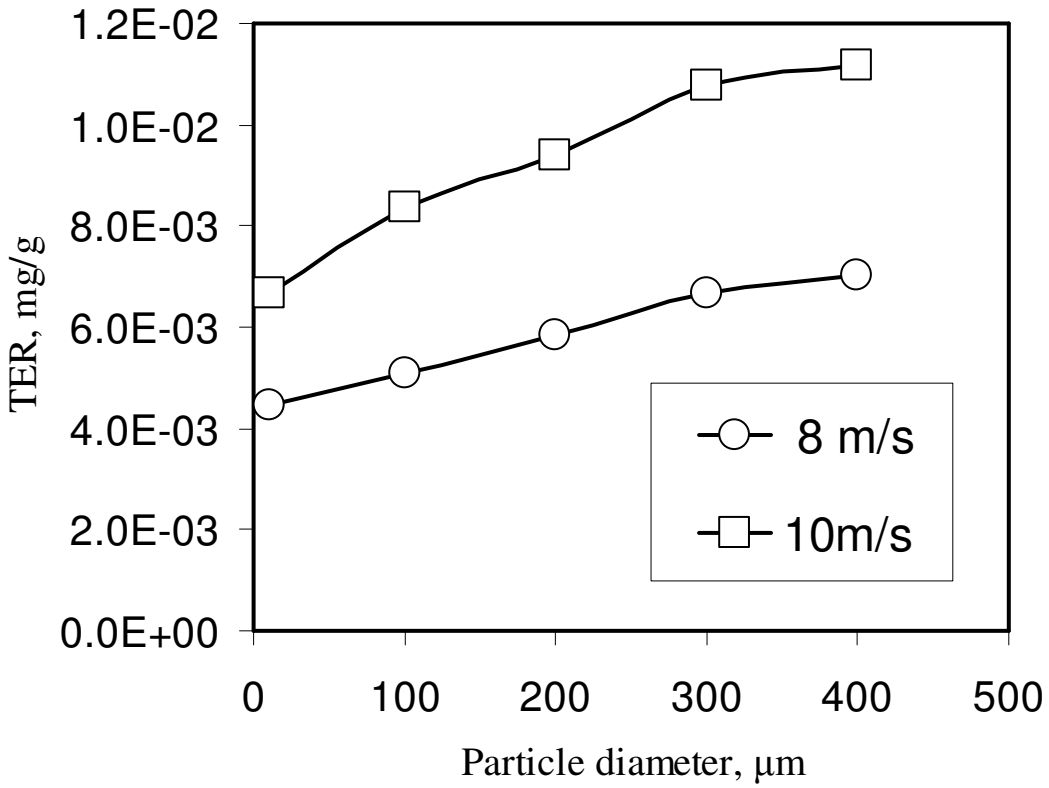

Figure 6.43: Influence of particle diameter on TER at different inlet velocities (for a case H=1mm, T= 3mm).

6.13.2 Effect of Particle Diameter and Protrusion Thickness on the Total Erosion and Penetration Rates

In this analysis, the protruded pipe thickness is varied for a range of values 1mm to 5mm. The depth is kept constant at 5mm for an inlet flow velocity of 10 m/s and contraction ratio of 0.5. Particle diameters are varied from 10-400 μm and their influence on protruded pipe erosion and penetration rates are plotted in Figures 6.44-6.45 respectively. It is observed that for each individual geometry of thickness 1mm, 3mm 4mm, 5mm, the total erosion rate increases with the increase of particle diameter. Comparisons are made among the geometries of various thicknesses. It is observed that the smallest thickness (1mm) is the maximum erosion prone for all the particle sizes. The other geometries in ascending order of thickness 3mm, 4mm, and 5mm are next most erosion prone geometries. The particles are impacting the outer surface of least thickness with the largest impingement angle. Thickness increment causes more and more fluid streamline curvature causing smaller impingement angle and subsequently lower erosion rates resulted. Similar trend is demonstrated for the penetration rate, as shown in Figure 6.45. Close observation of Figure 6.45 shows that 1mm thickness is the most penetrated geometry, for the same inlet flow velocity, depth and other conditions mentioned above.

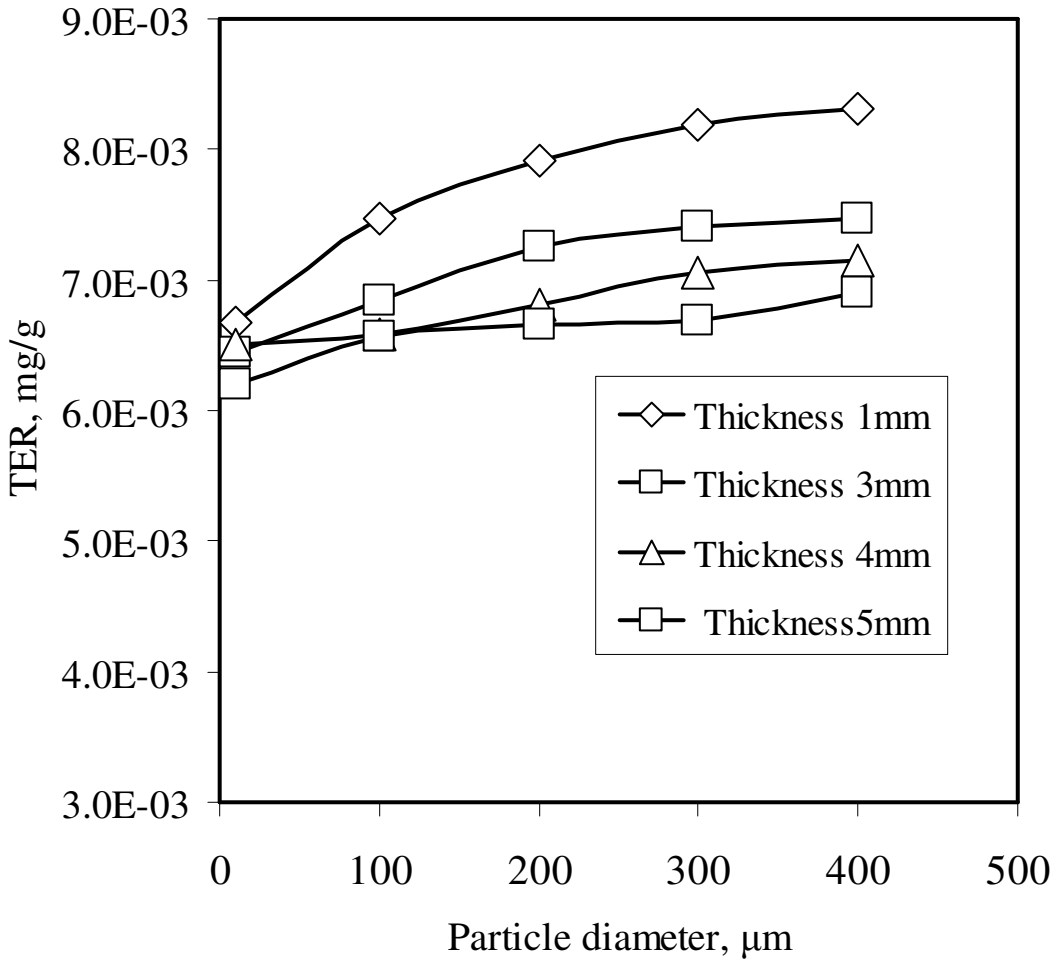

Figure 6.44: Influence of particle diameter on total erosion rates for different thicknesses, for the case V= 10 m/s, H=5mm, Cr=0.5.

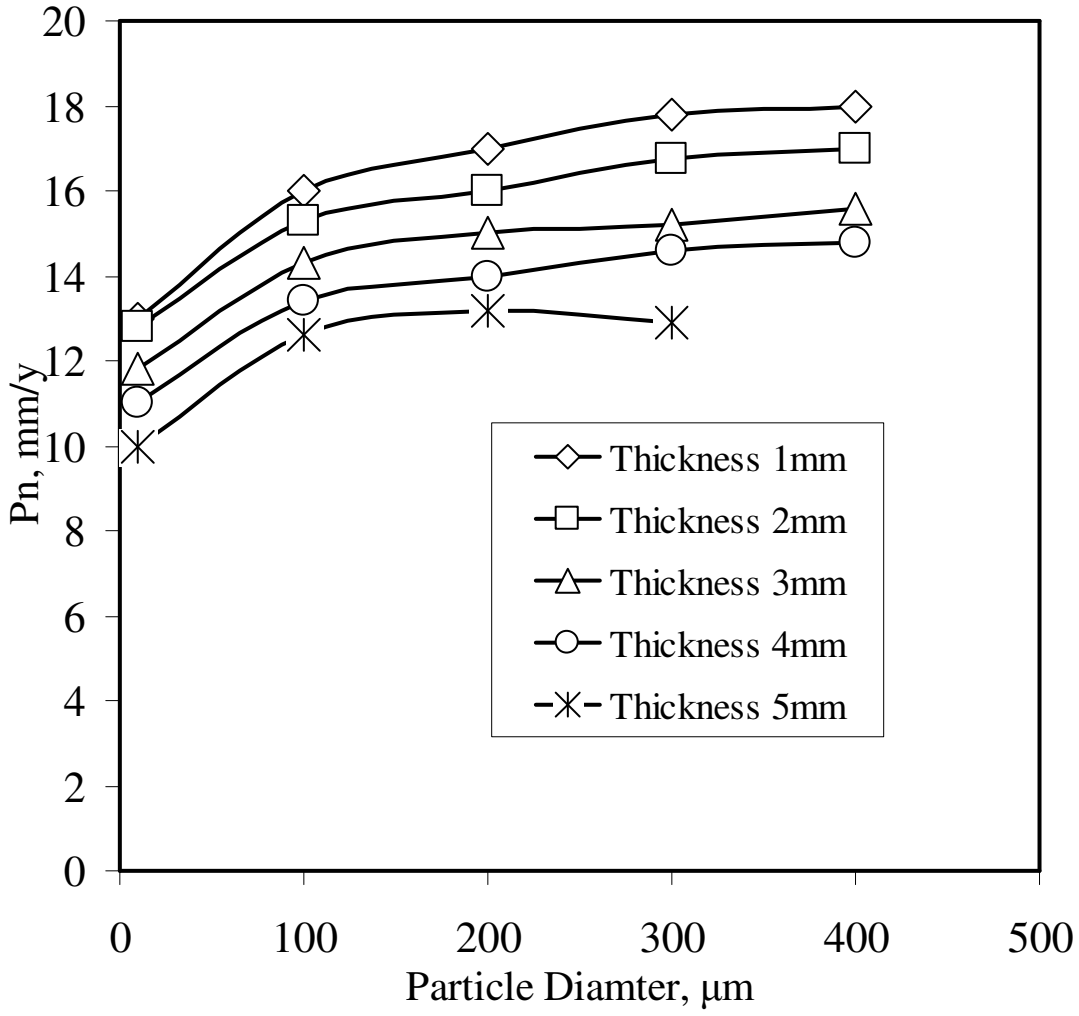

Figure 6.45: Influence of particle diameter on penetration rates for different thicknesses, for the case V= 10 m/s, H=5mm, Cr=0.5.

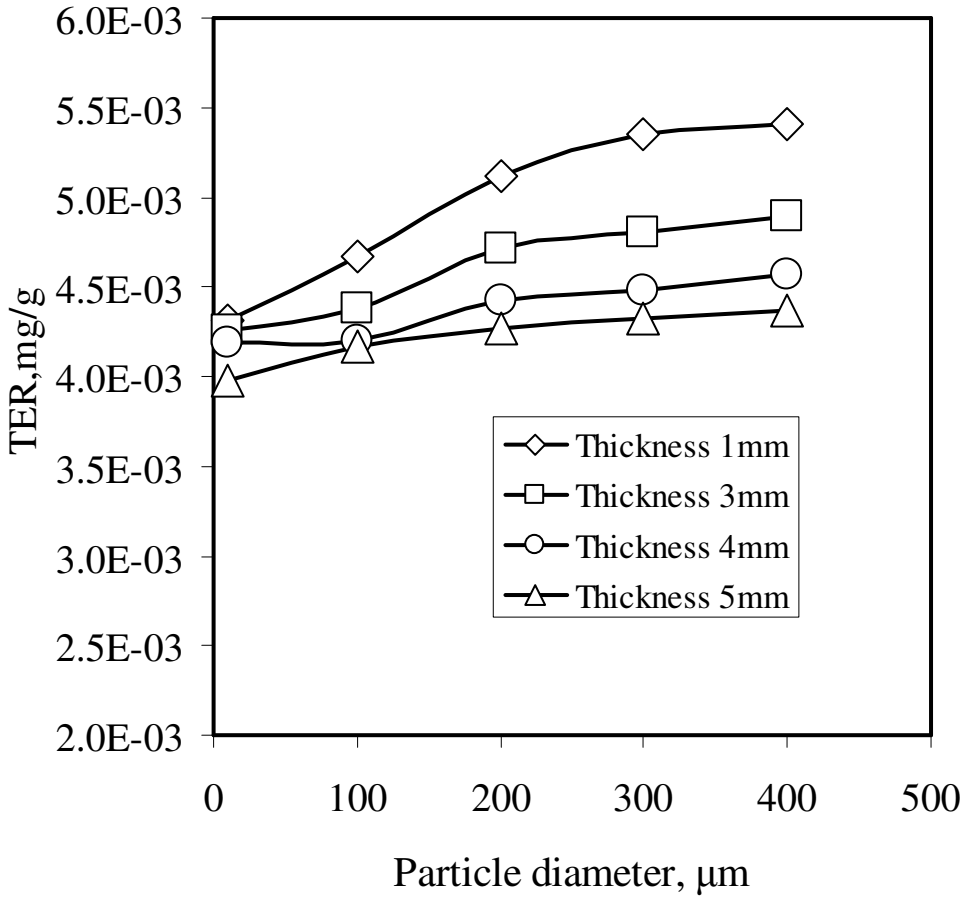

Figure 6.46: Influence of particle diameter on total erosion rates for different thicknesses, for the case V= 8 m/s, H=5mm, Cr=0.5.

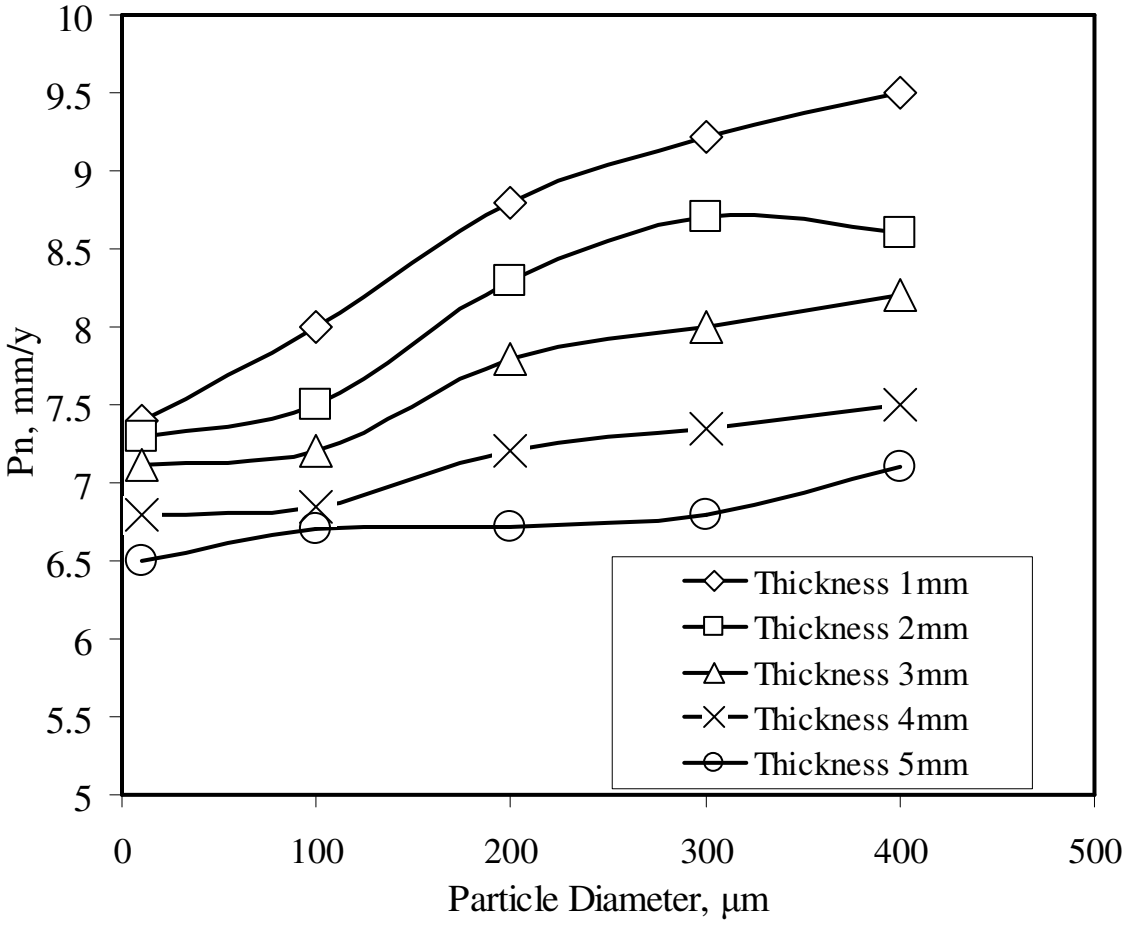

Figure 6.47: Influence of particle diameter on penetration rates for different thicknesses, for the case V= 8 m/s, H=5mm, Cr=0.5.

Considering the inlet flow velocity of 8m/s, depth 5mm, contraction ratio 0.5, a similar investigation is done. The results are shown in Figure 6.46 and 6.47. Here the findings are also the same as those for 10 m/s inlet flow velocity in Figures 6.44-6.45. Thickness 1mm, for a fixed depth of 5mm, is found to be the most eroded geometry. This is followed by subsequent thickness of 2mm, 3mm, 4mm, and 5mm (Figure 6.46). Observing Figure 6.47 reveals that 1mm thickness is the most penetrated geometry . For all the particle diameters values ranging from 10 μm to 400 μm, each geometry of follows the increasing trend in penetration rates. Comparing among themselves in terms of their thickness, the 1mm thickness has been found to be the most penetrated.

6.13.3 Effect of Particle Diameter and Protrusion Depth on the Total Erosion and Penetration Rates

In this section, the effects of particle diameter and protrusion depth on the total erosion and penetration rates are investigated. For all cases considered, the inlet flow velocity is kept constant (V=10 m/s) and the protrusion thickness was kept unchanged (T=3mm). The study was considered for a contraction ratio of 0.5. Figure 6.48 shows the variation in total erosion rate with particle diameter for four different values of protrusion depth. It is observed in Figure 6.48 that the total erosion rates increases with higher particle diameter for each of the depth considered. For the entire protrusion depth range from 2mm to 5mm, the highest total erosion rate occurred at a particle diameter of 400μm. This is consistent with the findings of the section 6.6. For all the particle sizes,

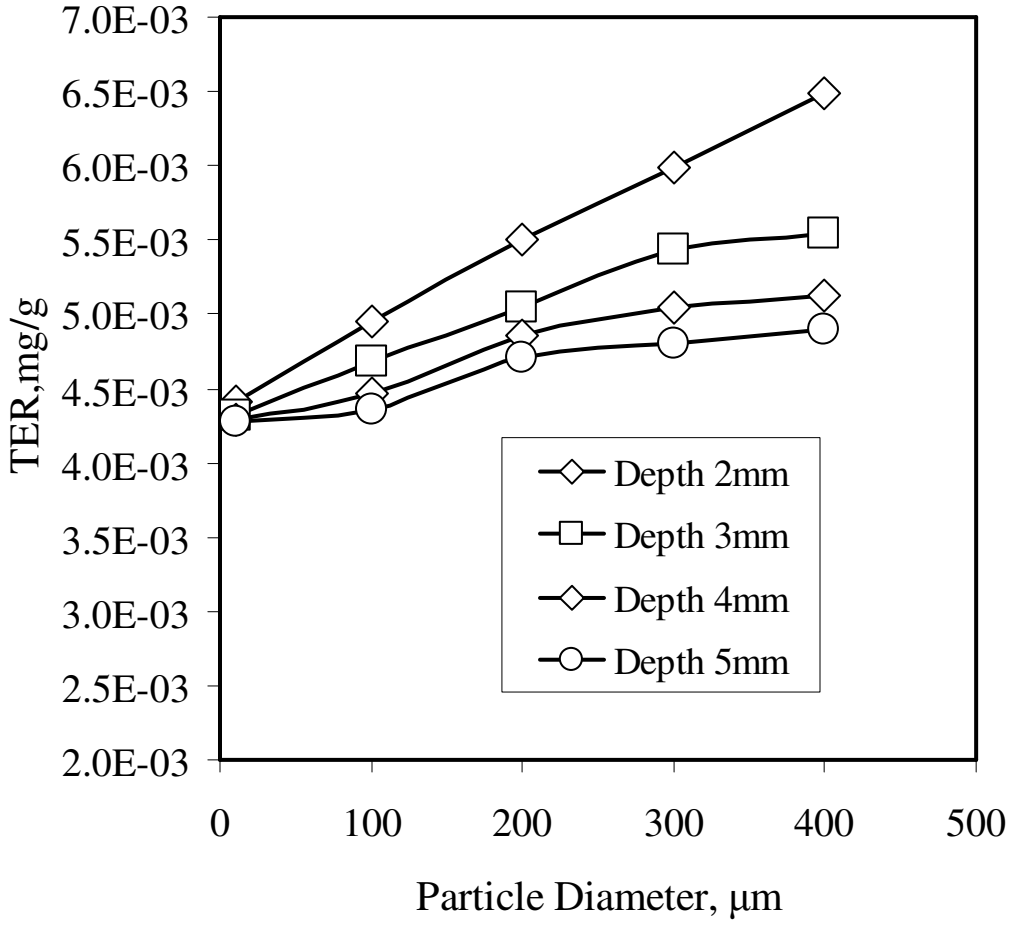

Figure 6.48: Influence of particle diameter on total erosion rate for different depths, for the case V= 8 m/s, T=3 mm, Cr=0.5.

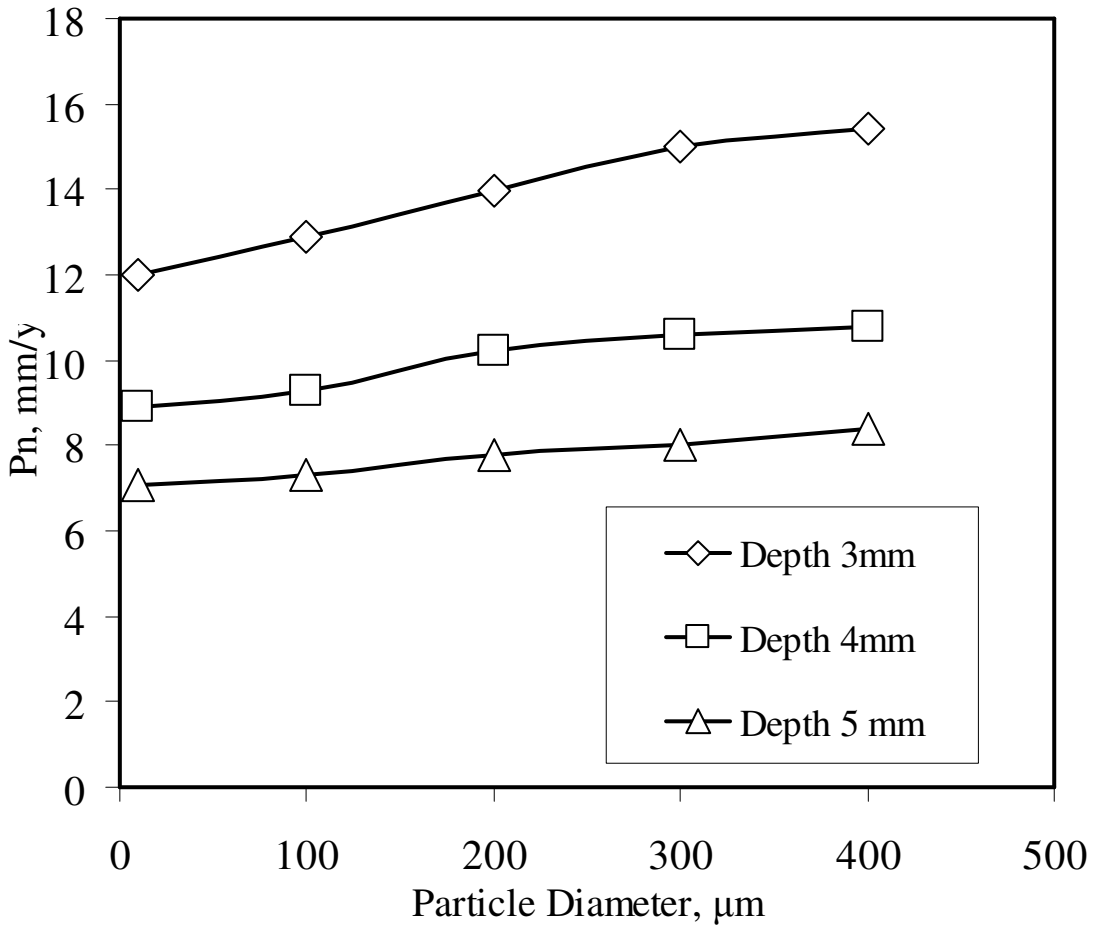

Figure 6.49: Influence of particle diameter on penetration rates for different depths, for the case V= 10 m/s, T=3 mm, Cr=0.5.

the maximum erosion rate occurred at the smallest depth of 2mm (Figure 6.48). Therefore, 2mm depth is the most eroded depth for the entire range of particle diameter from 10μm to 400 μm. The other depths of 3mm, 4mm, and 5mm, are the next most erosion prone depths in the ascending order. The particles are impacting the outer surface of the smallest depth with the largest impingement angle. Depth increment causes more and more fluid streamline curvature. As a result, smaller impingement angles occurred for higher values of depths. Subsequently, lower erosion rates resulted. Similar trend is observed for the penetration rates as shown in Figure 6.49. Close observation of Figure 6.49 shows that the smallest depth considered (3mm) is the most penetrated geometry, for all the operating conditions mentioned above. Higher depth values of 4mm and 5mm are respectively at the next places in terms of the most penetrated depths.

6.13.4 Effect of Inlet flow velocity and Protrusion Thickness on the Total Erosion and Penetration Rates

Analysis is done in this section to observe the influence of inlet flow velocity and protrusion thickness on the total erosion and penetration rates. For all the cases, the depth of the protrusion is kept constant at 5mm for a contraction ratio of 0.5. Inlet flow is varied in a range of values from 3 m/s to 10 m/s. Two sets of particle diameter (200 μm and 400 μm) are utilized for subsequent erosion and penetration rates calculations. Figure 6.50 and Figure 6.52 shows the variation of the total erosion rate with inlet flow velocity for four different protrusion thickness values, for particle diameters of 400 μm and 200

μm respectively. It is observed in Figure 6.50 that for all the thicknesses, total erosion rate exponentially increases with the inlet flow velocity. For a particle diameter of 400μm, smallest thickness of 1mm is the most erosion prone geometry followed by the subsequent larger thickness of 3mm, 4mm, 5mm. The similar trend is observed in Figure 6.52 where particle diameter of 200 μm was used. Trends of the penetration rates are presented in Figure 6.51 and Figure 6.53 for particle diameters of 400 μm and 200 μm respectively. Close observation of the Figure 6.51 shows that the smallest thickness of 2mm is the most penetrated thickness for the entire range of inlet flow velocity and for the particle diameter of 400 μm. Higher thickness values of 3mm, 4mm, and 5mm are the next most penetrated thicknesses respectively. Figure 6.53 shows the similar trend where the diameters of the eroding particles are kept constant at 200 μm. 1mm thickness is found to be the most penetrated geometry for the entire velocity range. Subsequent thickness in ascending order of 2mm, 3mm, 4mm, 5mm are at the next positions in terms of penetration rates.

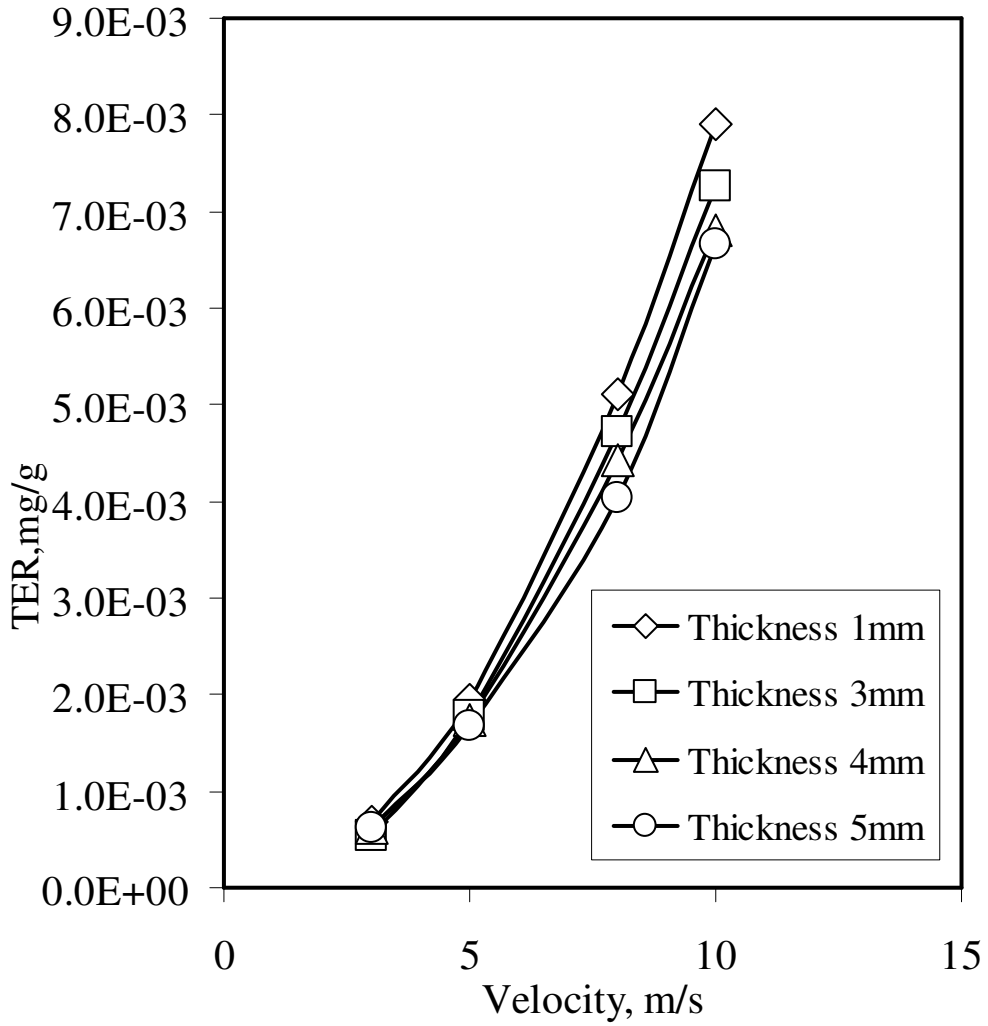

Figure 6.50: Influence of inlet flow velocity on total erosion rate for different thicknesses, for the case, H=5 mm, d_p =400 μm, Cr=0.5.

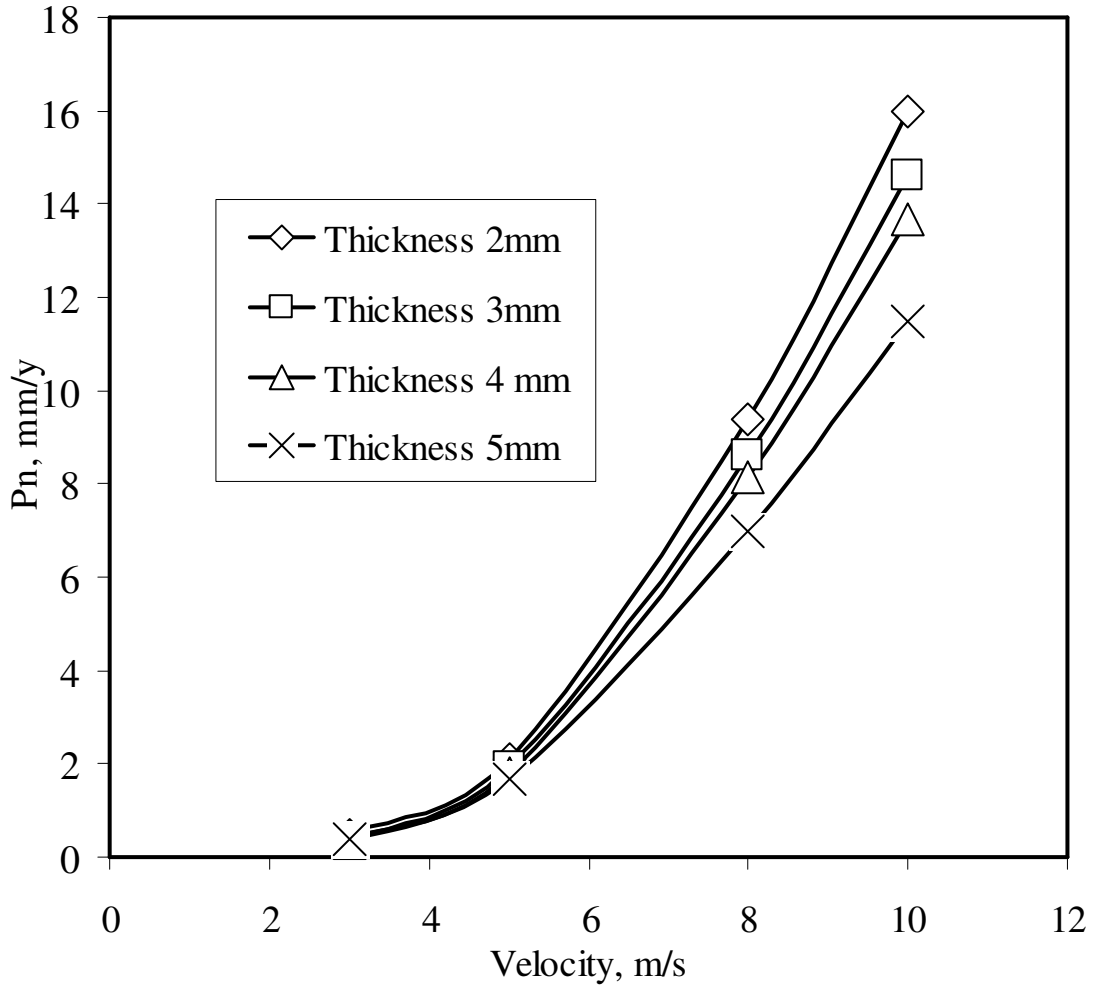

Figure 6.51: Influence of inlet flow velocity on penetration rate for different thicknesses, for the case, H=5 mm, d_p =400 μm, Cr=0.5.

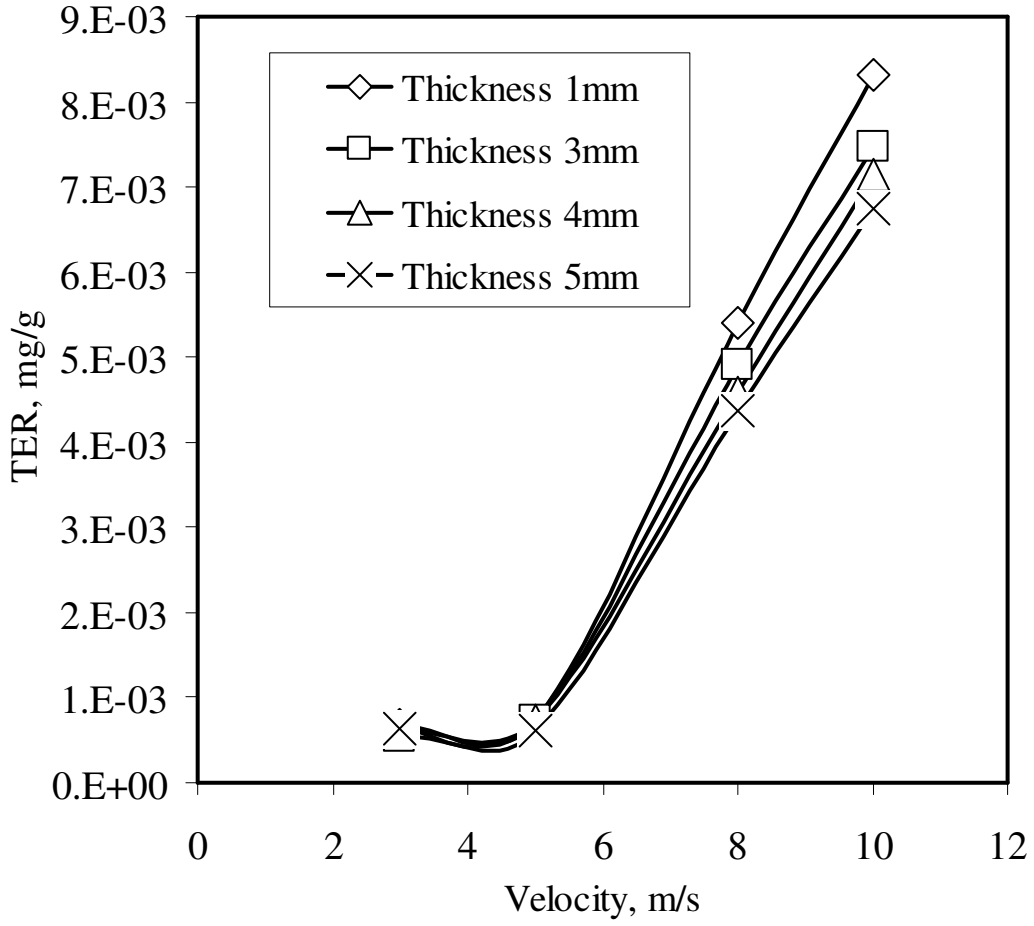

Figure 6.52: Influence of inlet flow velocity on total erosion rate for different thicknesses, for the case, H=5 mm, d_p =200 μm, Cr=0.5.

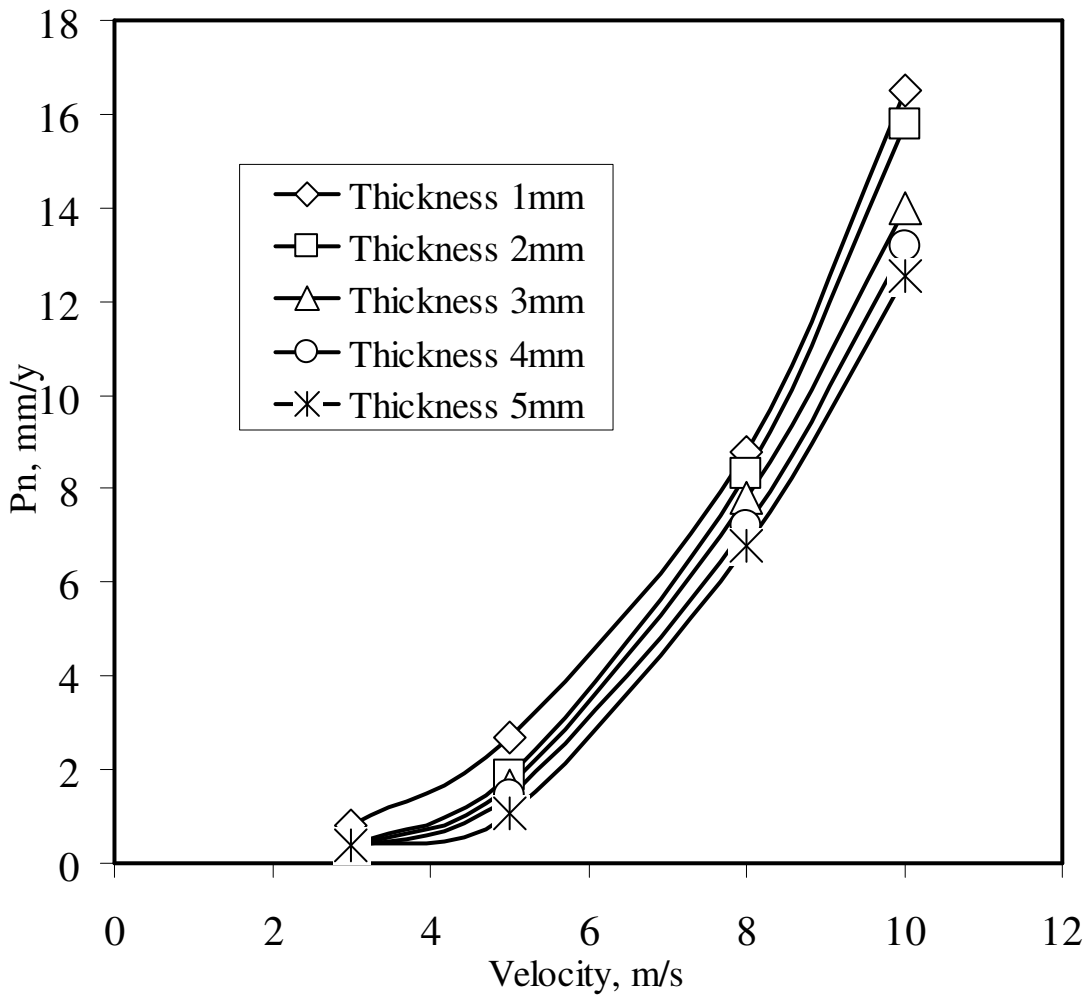

Figure 6.53: Influence of inlet flow velocity on penetration rate for different thicknesses, for the case, H=5 mm, d_p =200 μm, Cr=0.5.

6.13.5 Effect of Inlet Flow Velocity and Protrusion Depth on the Total Erosion and Penetration Rates

In this section, the effect of inlet flow velocity and protrusion depth on total erosion and penetration rates for different depths is analyzed. For all the cases considered here, the thickness is kept unchanged at a value 3mm for a particle diameter of 200 μm. The study was considered for a contraction ratio of 0.5. Figure 6.54 shows the variation of total erosion rate with inlet flow velocity for three values of protrusion depth. Total erosion rates for all these values of depth (2mm, 3mm, 4mm) increase exponentially with higher inlet flow velocities ranging from 3 to 10 m/s. The smallest depth of 2mm is found to be the most erosion prone for the entire range of inlet flow velocity. Results from the penetration curve in Figure 6.55 show similar findings. In Figure 6.55, it is observed that the smallest value of depth (2mm) is the most penetrated geometry for the entire velocity range (3 m/s to 10 m/s). These results are the further proof of curving away of the fluid streamlines when the depth is increased. Lower values of particle impingement angles occurred for higher depths and subsequently lower erosion and penetration rates resulted.

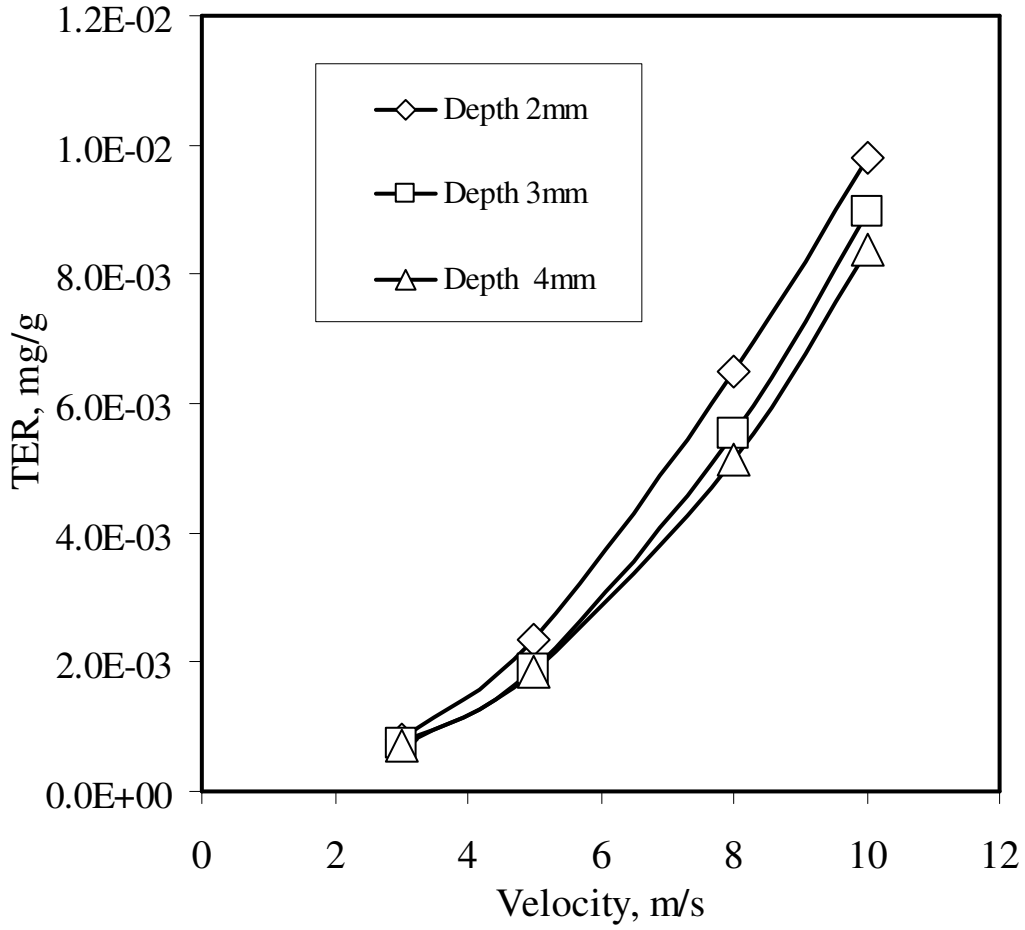

Figure 6.54: Influence of inlet flow velocity on total erosion rate for different depths, for the case T=3 mm, d_p =400 μm, and Cr=0.5.

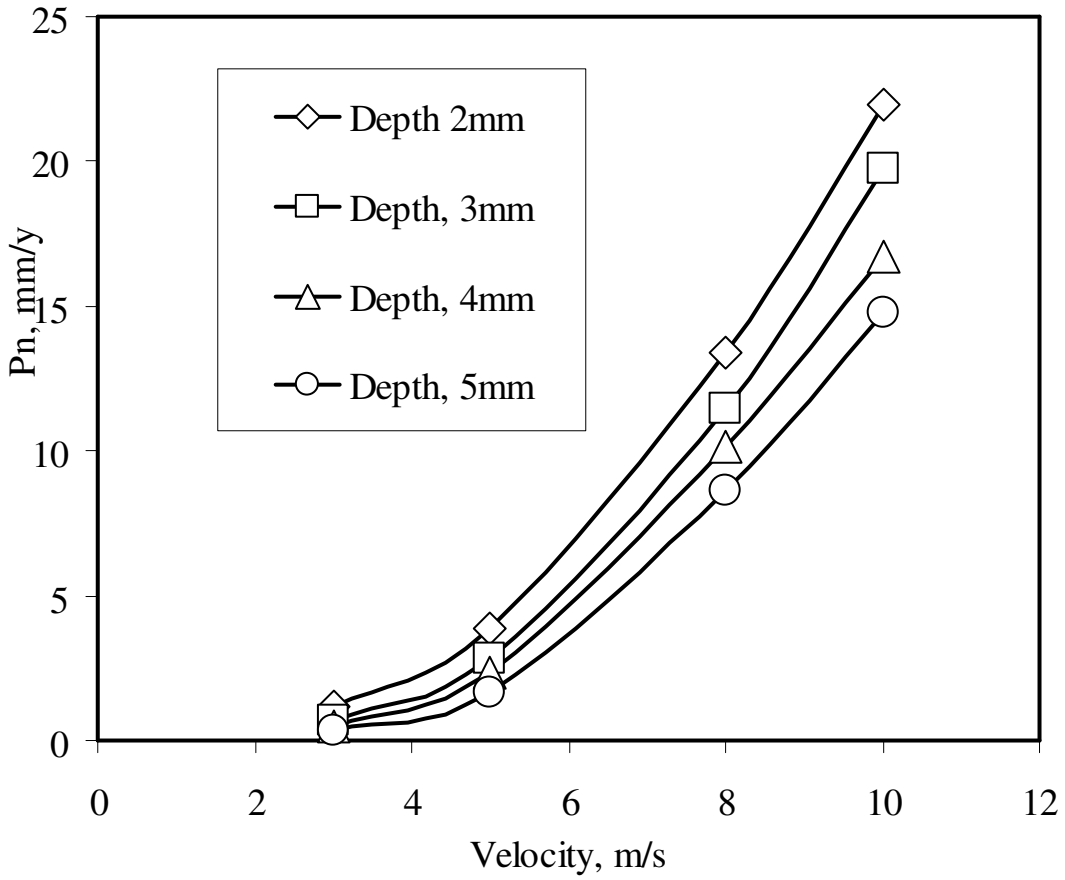

Figure 6.55: Influence of inlet flow velocity on penetration rate for varying depths, for the case T=3 mm, d_p =400 μm, and Cr=0.5.

Chapter 7

Conclusions and Recommendations

7.1 Conclusions

The present research work constitutes a comprehensive numerical study of erosion of a pipe protruded in sudden contraction. Various parameters related to flow conditions and the geometry of interest were varied to demonstrate their influence on the erosion rates of the protruded pipe. These parameters were the inlet flow velocity, V (m/s), the particle diameter, d_p (μm), the protruded pipe depth, H (mm), the protruded pipe thickness, T (mm), the contraction ratio, Cr, and the pipe wall material. In this research work, the results of erosion rates were reported in terms of total erosion rate (mg/g), penetration rate (mm/y) and local erosion rate (mg/g) of the protruded pipe.

The conclusions derived from the present study include:

1. The fully developed velocity profile remained almost constant along the pipe from inlet to a very close region of the protruded pipe. It was observed that the axial velocity profile showed significant change as it reached a position of 0.01m in front of the contraction plane. The axial velocity magnitude increased

significantly at that position, which was at very close proximity of the protruded pipe.

2. For the prescribed range of protruded pipe depths (1mm to 5mm), the particles impacted the outer surface of the protruded pipe only and completely bypassed the face and the inner surfaces.

3. For a protruded pipe depth larger than 0.1mm (for a contraction ratio 0.5), the above finding was valid. Below the depth of 0.1mm, the particles were found to be impacting the face surface of the protruded pipe. Thus, protruded pipe depth of 0.1mm for a contraction ratio 0.5, was termed as a "threshold limit" for the findings at number 2.

4. The comparison of calculations using RNG k-ε and Reynolds Stress Model (RSM) indicated that the differences in results between the two models were less than 10 %.

5. In particle tracking, it was observed that incorporating turbulence velocity fluctuation in the fluid flow equation yielded better results than those of the "mean" flow approach. A statistical representation of the spread of particle stream due to turbulence was adopted in the "stochastic approach" that caused this improvement.

6. Erosion rate of the protruded pipe was very prominently influenced by the variation of inlet flow velocity. In this study, the inlet flow velocity larger than 8m/s was marked as "alarming" limit for protruded pipe erosion. Inlet velocity

value of 3m/s was found to be the “threshold limit” for the occurrence of significant erosion.

7. It was found that with increasing particle diameter, the erosion rate gradually increased.

8. It was observed that the erosion rates were inversely related to both protruded pipe depth and thickness. Erosion rates were increased due to decrease in the protruded pipe depth and thickness respectively. The opposite was also true.

9. Erosion rate Material was found to be inversely related to the material Hardness Number (BHN). Higher BHN resulted in lower erosion rate and vice versa.

10. From different combinations of geometries (by varying depth and keeping thickness fixed or vice versa), it was found that the geometry with the smallest depth or thickness was the most erosion prone and the most penetrated geometry. This finding holds true for an entire range of particle diameter and inlet flow variations.

11. Erosion rate was found to be inversely proportional to the Contraction ratio, Cr, of the pipe geometry. Higher contraction ratio resulted in lower erosion rate and vice versa.

12. It was observed that the erosion of the protruded pipe is a highly localized phenomenon. Intensity of the local erosion rates was very high at the inner tip of the outer surface of protruded pipe.

7.2 Recommendations for future work

1. The scope of the present study is limited by the assumption of two-dimensional, axi- symmetric flow. Extension of the present study is required for three-dimensional turbulent flows to gain a deeper insight into the erosion phenomenon of the present geometry.

2. Further investigations can be performed with the parameters and their influence on erosion rate of the protruded pipe. Erodent material of different shapes, different inlet condition can be applied to observe their influences on the erosion rates. More comprehensive studies can be performed using different target material.

3. Experimental study is required to get more representative results on erosion rates. Moreover, better validation for future numerical works can be attained in this way.

Bibliography

Adeniji-Fashola, A., Chen, C.P., "Modeling of confined turbulent fluid-particle flows using Eulerian and Lagrangian schemes". International Journal of Heat and Mass transfer, Vol. 33, No. 4, pp. 691-701, 1990.

Ahlert, K.R., "Effects of particle impingement angle and surface wetting on solid particle erosion of ANSI 1018 steel". M.S. Thesis, University of Tulsa, 1994.

Astarita, G., Grego, G., "Excess pressure drop in laminar flow through sudden contraction". Int. Eng. Chem. Fundamentals, Vol. 7, No. 1, pp. 27-31, 1968.

Badr, H.M., Habib, M.A., Ben-Mansour, R., Said, S.A.M., "Effect of flow velocity and particle size on erosion in a pipe with sudden contraction". The 6th Saudi Engineering Conference, Vol. 5, Dhahran, K.S.A., 14-17 th December, 2002.

Badr, H.M., Habib, M.A., Ben-Mansour, R., Said, S.A.M., "Numerical investigation of erosion threshold velocity in a pipe with sudden contraction". Computers & Fluids, Vol.34, pp. 721-742, 2005.

Benedict, R.P., Carlucci, N.A., Swetz, S.D., "Flow losses in abrupt enlargements and contractions". Transactions ASME, J. of Eng. For Power, Vol. 88, pp.73-81, 1966.

Blanchard, D.J., Griffith, P., Rabinoweiz, E., "Erosion of a pipe bend by solid particle entrained in water". Journal of Engineering for Industry, Vol.106, pp. 213-217, 1984.

Bourgoyne, A.T., "Experimental study of erosion in diverter systems due to sand production". SPE/AIDC 18716. Presented at 1989 SPE/IADC Drilling Conference held in New Orleans, Louisiana, pp. 807-816, 1989.

Bullen, P.R., Cheeseman D.J., Hussain, L.A., " The determination of pipe contraction pressure loss coefficient for incompressible turbulent flow". Kingston Polytechnic, pp.111-119, December 1986.

Bullen, P.R., Cheeseman D.J., Hussain, L.A., “A study of flow in pipe contraction”. Proc. Inst Mech. Engrs., Vol. 210, pp.171-180, 1996.

Chang, K.C., Wu, W.-J., “ Sensitivity study on Monte Carlo solution procedure of two-phase turbulent flow”. Numerical Heat Transfer, Part B, Vol. 25, pp. 223-244, 1994.

Chen, X., Mclaury, B.S., Shirazi, S.A., “Application and experimental validation of a computational fluid dynamics (CFD) based erosion prediction model in elbows and plugged tees”. Computers & Fluids, Vol. 33, pp. 1251-1272, 2004.

Clark, H.M.I., Burmeister, L.C., “The influence of the squeeze film on particle impact velocities in erosion”. International Journal of Impact Engineering, Vol.12, No. 3, pp. 15-426, 1992.

Clift, R.,Grace, J.R., Weber M.E., ”Bubbles, Drops and Particles”. Academic Press, New York, 1978.

Crowe, C.T., Sharma, M.P., Stock, D.E., “ The Particle-Source-In Cell (PSI-CELL) model for gas-droplet flows”. Transactions of the ASME, Journal of Fluids Engineering, June 1997, pp. 325-332, 1977.

Durst F., Milojevic D., Schonung B., “Eulerian and Lagrangian predictions of particulate two-phase flow: a numerical study. “Appl. Mathematical Modeling, Vol.8, pp.101-115, 1985.

Edwards, J.K., McLaury, B.S., Shirazi, S.A., “Supplementing a CFD code with erosion prediction capabilities. ASME Fluids Engineering Division Summer Conference, Paper FEDSM 98-5229, 1998.

Edwards, J.K., McLaury, B.S., Shirazi, S.A., “ Evaluation of alternative pipe bend fittings in erosive service”. FEDSM2000-11245, Proceedings of the ASME Fluids Engineering Division Summer Meeting, June 11-15, 2000, Boston, MA, 2000.

Enayet, M., Gibson, M., Taylor, A., Yianneskis, M., "Laser-Doppler measurements of laminar and turbulent flow in a pipe bend". International Journal of Heat and Fluid Flow, Vol. 3, pp. 213-219, 1982.

Eyler, R.L., "Design and analysis of a pneumatic flow loop". M.S. Thesis, West Virginia, 1987.

Finnie, I., "The mechanism of erosion of ductile materials". Proceedings of the third US National Congress of Applied Mechanics, pp. 527-532, 1958.

Finnie, I., "Erosion of surfaces by solid particles". Wear, Vol. 3, pp. 87-103, 1960.

Finnie, I., "Some observations on the erosion of ductile metals". Wear, Vol. 19, pp. 81-90, 1972.

Finnie, I., Stevick, G.R., Ridgely, J.R., "The influence of impingement angle on the erosion of ductile metals by angular abrasive particles". Wear, Vol. 152, pp. 91-98, 1992.

Finnie, I., "Some reflections on the past and future of erosion". Wear, Vol. 186/187, pp. 1-10, 1995.

Fluent 6.1 Documentation, Fluent Inc., Lebanon, NH, U.S.A.

Forder, A.F., Thew, M.T., Harrison, D., "A CFD model to analyze erosion within oilfield control valves". Third CFX International Users Conference, pp. 415-427, 1996.

Forder, A., Thew, M., Harrison, D., "A numerical investigation of solid particle erosion experienced within oilfield control valves. Wear, Vol. 216, pp. 184-193, 1998.

Fossa, M., Gugliemini, G., "Dynamic void fraction measurement in horizontal ducts with sudden area contraction". International Journal of Heat and Mass Transfer, Vol. 41, pp.3807-3815, 1998.

Gerami-Tajabadi, H., "The determination of pressure loss coefficients for an incompressible turbulent flow through pipe contraction, Mphil. Thesis, Kingston Polytechnic, 1985.

Gosman, A.D., Ioannides, E., "Aspects of computer simulation of liquid-fuelled combustors." AIAA 19th Aerospace Sciences Meeting, Paper AIAA-81-0323, 1981.

Govan, A.H., Hewitt, G.F., Ngan, C.F., "Particle motion in a turbulent pipe flow". International Journal of Multiphase Flow, Vol. 15, No. 3, pp. 471-481, 1989.

Graham, D.I., "An improved eddy interaction model for numerical simulation of turbulent particle dispersion". ASME, Fluids Engineering Division, (Publication) FED, Vol. 228, pp. 161-167, 1995.

Graham, D.I., "An improved eddy interaction model for numerical simulation of turbulent particle dispersion", Journal of Fluids Engineering, Vol. 118, pp. 819-823, 1996.

Grant, G., Tabakoff, W., "Erosion prediction in turbo machinery resulting from environmental solid particles". Journal of Aircraft, Vol. 12, No. 5, pp. 471-478, 1975.

Habib, M.A., Attya, A., McEligot, D.M., "Calculation of turbulent flow and heat transfer in channels with streamwise periodic flow.". ASME Journal of Turbomachninery, Vol. 110, pp.405-411, 1989.

Habib, M.A., Badr, H.M., Ben-Mansour, R., Said, S.A.M., "Numerical calculations of erosion in an abrupt pipe contraction of different contraction ratios". International Journal for Numerical Methods in Fluids, Vol. 46, pp. 19-35, 2004.

Hanson, R., Patel, M.K., "Development of a model to predict the life of pneumatic conveyor bends subject to erosive wear". FEDSM2000-11246, Proceedings of the ASME Fluids Engineering Division Summer Meeting, June 11-15, 2000, Boston, MA., 2000.

Hashish, M., "An improved model of erosion by solid particle impact". Proceedings of the 7th International Conference on Erosion by Liquid and Solid Impact, Cambridge, UK, pp. 66-1, 66-9, 1987.

Hengshuan, C., Zhong, X., "Numerical analysis and experimental investigation of erosion in variable rectangular-section bends by solid particles". Chinese Journal of Mechanical Engineering (English Edition), Vol. 3, No. 1, pp. 111-118, 1990.

Haugen, K., Kvernvold, O., Ronold, A., Sandberg, R., "Sand erosion of wear-resistant materials: Erosion in choke valves". Wear, Vol. 186/187, pp. 179-188, 1995.

Hinze, J.O., "Turbulence". McGraw-Hill, New York, 1975.

Incropera, F.P., and DeWitt, D.P., "Fundamentals of Heat and Mass Transfer". Fourth Edition, Jon Wiley and Sons, 1996.

Jayanti, S., Hewitt, G.F., "Review of literature on dispersed two-phase flow with a view to CFD modeling". Report AEA APS – 0099 from AEA Petroleum Services, AEA Technology, Harwell Laboratory, Oxon, OX11 ORA, 1991.

Jones, W.P., and Launder, B.E., "The Calculation of low-Reynolds number phenomena with a Two-Equation Model of Turbulence". International journal of Heat and Mass Transfer, Vol. 16, pp. 1119-1130, 1973.

Kays, W.M., " Loss coefficient for abrupt changes in flow cross section with low Reynolds flow in single and multi-tube systems, Trans. ASME, J. of Fluids Eng.,Vol. 72, pp.1067-1074, 1950.

Keating A., Nesic, S., "Particle tracking and erosion prediction in three-dimensional bends". Proceedings of FEDSM2000, ASME Fluids Engineering Summer Meeting, Boston, MA, June 11-15, 2000.

Khezzar, L., Wimpactelaw, J.H., Yiannesk, M., "Round sudden-expansion flows". Proc. IMeche, Vol. 200, No. C 6, pp. 447-455, 1988.

Lapidus, L. and Pinder, G.F., "Numerical solution of particle differential equations in science and engineering". John Wiley and Sons, 1982.

Launder, B.E., and Spalding, D.B., "Lectures in Mathematical Models of turbulence". Academic Press Inc., London, 1972.

Launder, B.E., Reece, G.J. and Rodi, W., "Progress in the development of Reynolds-stress turbulence closure". Journal of Fluid Mechanics, Vol. 68, No. 3, pp. 537-566, 1975.

Lu, Q., Fontane J.R., Auberitne, G., "A Lagrangian model for solid particles in turbulent flows." Intl. J. of Multiphase Flow, Vol. 19, No.2, pp. 347-367, 1993.

Mason, J.S., Smith, B.V., "The erosion of bends by pneumatically conveyed suspensions of abrasive particles". Powder Technology, Vol. 6, pp. 323-335, 1972.

McLaury, B., "Predicting solid particle erosion resulting from turbulent fluctuations in oilfield geometries". PhD Thesis, Department of Mechanical Engineering, University of Tulsa, 1996.

Meng, H., Van Der Geld, C.W.M., "Particle trajectory computations in steady non-uniform liquid flows". ASME, Fluids Engineering Division (Publication) FED, Vol. 118, pp. 183-193, 1991.

Michaelides, E.E., "Review-The transient equation of motion for particles, bubbles, and droplets". ASME Journal of Fluids Engineering, Vol. 119, pp.233-247, 1997.

Neilson, J.H., Gilchrist, A., "Erosion by a stream of solid particles". Wear, Vol. 11, pp. 111-122, 1968.

Nokleberg, L., Sontvedt, T., "Erosion in choke valves- oil and gas industry applications". Wear, Vol. 186/187, pp. 401-412, 1995.

Nokleberg, L., Sontvedt, T., "Erosion of oil and gas industry choke valves using computational fluid dynamics and experiment", International Journal of Heat and Fluid Flow, Vol. 19, pp. 636-643, 1998.

Odar, F., Hamilton, W.S., "Forces on a sphere accelerating in a viscous fluid". Journal of Fluid Mechanics, Vol. 18, pp. 302-314, 1964.

Patankar, S.V., Spalding, D.B. "A calculation procedure for heat, mass, and momentum transfer in three dimensional parabolic flows". International Journal of Heat and Mass Transfer, Vol. 15, pp. ,1972.

Patankar, S.V., "Numerical heat transfer and fluid flow". Hemisphere Publishing Corporation, 1980.

Picart, A, Berlemont, A., Gouesbet, G., "Modeling and predicting turbulence fields and the dispersion of discrete particles transported by turbulent flows". International Journal of Multiphase Flow, Vol. 12, No. 2, pp. 237-261, 1986.

Postlethwaite, J., Nesic, S., "Erosion in distributed liquid/particle pipe flow: Effects of flow geometry and particle surface roughness". Corrosion, Vol. 49, No. 10, pp. 850-859, Oct. 1993.

Reynolds, W.C., "Fundamentals of turbulence for turbulence modeling and simulation", Lecture notes for Von Karman institute, Agard report no. 755, 1987.

Roco, M.C., Addie, G.R, "Analytical model and experimental studies on slurry flow and erosion in pump casings. Slurry Transportation", Vol. 8, pp. 263-276, 1983.

Roco, M.C., Nair, P., Addie, G.R., Dennis, J.," Erosion of concentrated slurries in turbulent flow". Journal of Pipelines, Vol. 4, No. 3, pp. 213-221, 1984.

Rubini, P., Boysan, F., Swithenbank, J., "The computation of gaseous particle laden flow around pipe bends". Second International Conference on Multi-Phase Flow, London, pp. 229-243, 1985.

Saffman, P.G., "The lift on a small sphere in a slow shear flow". Journal of Fluid Mechanics, Vol. 22, No. 2, pp. 385-400, 1965.

Salama, M.M., Venkatesh, E.S., "Evaluation of erosional velocity limitations of offshore gas wells". Offshore Technology Conference, OTC no. 4485, TX, May2-5, 1983.

Salam, M.M., "An alternative to API 14 E erosion velocity limits for sand laden fluids". Offshore Technology Conference, Houston, TX, pp. 721-731, May 4-7, 1998.

Schuh, M.J., Schuler, C.A., Humphrey, J.A.C., "Numerical calculation of particle-laden gas flows past tubes". AIChE Journal, Vol. 35, No. 3, pp. 466-480, 1989.

Shih, T., Liou, W.W., Shabbir, A., "A new κ-ε eddy viscosity model for high Reynolds number turbulent flows – model development and validation". Computers and Fluids, Vol.24, No.3, pp.227-238, 1995.

Shirazi, S.A., Shadley, J.R., Mclaury, B.S., "A procedure to predict solid particle erosion in elbows and tees". Journal of Pressure Vessel Technology, Vol.117, pp.45-52, 1995.

Shirolkar, J.S., Coimbra, C.F.M., Queiroz McQuay, M., "Fundamental aspects of modeling turbulent particle dispersion in dilute flows". Progress in Energy and Combustion Science, Vol. 22, pp.363-399, 1996.

Sommerfeld, M., Zivkovic, G., "Recent advances in the numerical simulation of pneumatic conveying through pipe systems". Computational Methods in Applied Sciences, C. Hirsch (Editor), Elsevier Science Publishers, pp. 201-212, 1992.

Tabakoff, W., Malak, M.F., Hamed, "A Laser measurements of solid-particle rebound parameters on 2024 aluminum and 6A1-4V titanium alloys". AIAA Journal, Vo. 25, No. 5, pp. 721-726, 1987.

Tu, J.Y., Lee, B.E., Fletcher, C.A.J., "Eulerian modeling of particle-wall collisions in confined gas-particle flows via a Lagrangian approach". ASME, Fluids Engineering Division (Publication) FED, Vol. 236, No. 1, pp. 751-758, 1996.

Von Karman, T. “Turbulence”, Twenty Wilbur Wright Memorial Lecture, Journal of Aeronautical Science, Vol. 41, pp. 1109, 1937.

Wallace, M.S., Peters, J.S., “CFD based erosion modeling of multi-orifice choke valve”. Proceedings of 2000 ASME Fluids Engineering Summer Meetings, Boston, MA, Paper No. FEDSM 2000-11244, 2000.

Wallace, M.S., Dempster, W.M., Scanlon, T., Peters, J., McCulloch, S., “Prediction of impact erosion in valve geometries”. Wear, Vol. 256, pp. 927-936, 2004.

Wang, J., Shirazi, S.A., “A CFD based correlation for erosion factor for long-radius elbows and bends”. Transactions of the ASME, Vol.125, pp. 26-34, March 2003.

Wilcox, D.C., “Turbulence Modeling for CFD”, DCW Industries, 2000.

Wood, R.J.K., Jones T.F., Ganeshalingam, J., Miles, N.J., “Comparison of predicted and experimental erosion estimates in slurry ducts”. Wear, Vol. 256, pp. 937-947, 2004.

Yakhot V., Orszag S.A., “ Renormalization group analysis of turbulence.I.Basic theory”, Journal of Scientific Computing, Vol. 1, no. 1, pp. 3-51, March 1986.

Zhang, Z., Cheng, Z., Aheng, Y., “Numerical simulation of erosion-corrosion in liquid-solid two phase flow”. Chinese J. of Chemcial Engineering, Vol. 8, pp. 111-118, 2000.

VITA

NAME:	MUHAMMAD EHSANUL KABIR
PLACE OF BIRTH:	Dhaka, Bangladesh.
ADDRESS:	H. No. 62, Road No. 16, Block: A,
	Banani Model Town,
	Dhaka, Bangladesh.
PHONE NO.:	880-29675117.
E-MAIL:	ehsan_kabir@yahoo.com

EDUCATIONAL QUALIFICATION:

M.S (Mechanical Engineering)

June 2005

King Fahd University of Petroleum and Minerals

Dhahran, Saudi Arabia.

B.S. (Mechanical Engineering)

October 1999

Bangladesh University of Engineering and Technology

Dhaka, Bangladesh.